Re-evaluation of analytical chemistry techniques in studying DNA structures

Jesse H. Vanloon, M.Sc

Biotechnology

A THESIS SUBMITED IN PARTIAL FULFILMENT OF

REQUIREMENTS FOR THE DEGREE OF

MASTERS OF SCIENCE

Faculty of Mathematics and Science, Brock University

St. Catharines, Ontario

January, 2021

Abstract

This work describes the use of analytical chemistry techniques to examine the structural changes that DNA adopts when subjected to a number of external/internal factors. A self-complementary sequence, $d(CG)_9$, and a non-self-complementary sequence (mixed sequence) were used to study the conformational effects displayed by each type of oligonucleotide sequence. The structural changes adopted by DNA was examined using a variety of analytical techniques, such as: nuclear magnetic resonance imaging (NMR), differential scanning calorimetry (DSC), ultra violet visible (UV-Vis) spectroscopy, circular dichroism (CD) spectroscopy, and high-performance liquid chromatography (HPLC). 1) $d(CG)_9$ and a mixed sequence in the B- and Z-DNA conformation was examined by CD and UV-Vis at a concentration of 1m*M* using a home-made cuvette called a Flexicell with a minimum pathlength of 0.129± 0.015 mm. The CD and UV-Vis spectra's produced were found to be reliable when compared to commercial cuvettes with a pathlength of 1 cm and sample concentration of 10 µ*M*. 2) $d(CG)_9$ was lyophilized and reconstituted using either water or buffer to determine if $d(CG)_9$ adopts a different structure when reconstituted using different conditions. It was determined that lyophilized $d(CG)_9$ adopts a hairpin conformation when reconstituted with water, and a B-DNA duplex when reconstituted with a buffer containing NaCl. 3) $d(CG)_9$ was thermally denatured using DSC to determine if DSC can be a viable method to study oligonucleotides. It was determined that $d(CG)_9$ undergoes a two-state unfolding pathway. 4) Nuclear Overhauser Effect spectroscopy (NOESY) and correlation spectroscopy (COSY) were used to examine the conformational differences of 2'-deoxyadenosine when incubated in water. From the distance and torsion angle constraints obtained from NOESY and COSY respectively, and from existing

crystal structures, it was found the structures that were determined by NMR spectroscopy were misleading because of spectral artifacts. 5) A mixed sequence was treated with organic modifying agents to determine the minimal condition required for DNA denaturation when different modifiers were used. It was determined that urea at a concentration of 8 *M* and at a pH of 12.5 is sufficient to denature the mixed sequence duplex.

Acknowledgements

I would like to thank my supervisor Professor Dr. Hongbin (Tony) Yan for his patience, support, guidance and for giving me this opportunity to work in his lab, I would like to thank my supervisory committee members Professor Dr. Heather Gordon and Dr. Douglas Bruce. I would like to extend my gratitude to Dr. Heather Gordon for her support, patience, and guidance both in my academic and personal life. I would like to acknowledge Dr. Jeffery Attkinson, Dr. Paul Zelisko, Dr. Costa Metallinos for all of their help and advice when I needed guidance during my time as a graduate student. I would like to thank Dr. Thad Harroun, and Razvan Simionesu for their assistance regarding the analysis of my data. I would like to acknowledge colleagues, and friends in: 1) Dr. Yan's group: Dr. Dhruval Joshi, Frank Betancourt, James Deluca-Helmkay, Michelle Groux, Hailey Ann Bennet, Alyssa McAdorey, Quanjian Li, Quynn Gilmour, Matteo Iacucci , and Raissa Sultana, 2) Dr. Atkinson's group: Dr. Candice Panagabko, Yvonne Yong, Rachel Ciccone, Kailey Meehan, Vansh Mehta, Marcelo Victor, and Yassaman Hosseini, 3) Dr. Lemaire's group: Dr. Nico Bonanno, Mark Pelaccia, Zackery Watts, and Meneesha Wijesundara, 4) Dr. Metallinos group: Dusty Cadwallader, Nan Tran, Lyzcel Talisic, and Claire Snelgrove, 5) Dr. Nickeonov's group: Josh Clark, Anton Dmitrienko, and Medet Segizbayev, 6) Dr. Pilkington's group; Mike D'Agostino, and Gabe DellMonache.

To other members of these groups that were not mentioned I appreciate all that you have done. I would like to acknowledge the ladies of the Science Stores: Irene Palumbo, and Allison Smart, and the ladies of custodial services, specifically: Heather, Elain, Elin, Margo, and Tammy. I would like to acknowledge Olivia DeBartolo and Charles Barraco for their kindness, friendship, and support. I would like to extend my gratitude to Charles Barraco, my best friend,

for his guidance, advice, help with my experimental techniques and input on my research. Lastly, I would like to acknowledge my parents for their continued love and support throughout the years.

Table of contents

List of Figures

List of Tables

List of Abbreviations

dA	2’-deoxyadenosine
dC	2’-deoxycytosine
DC	Direct current
dG	2’-deoxyguanosine
DGEOM	Distance geometry
DMSO	Dimethyl sulfoxide
DNA	Deoxynucleic acid
DOSY	Diffusion ordered spectroscopy
DSC	Differential scanning calorimetry
FID	Free induction decay
ΔG	Gibbs free energy
G	Guanine
GNP	Gold-nanoparticles
ΔH	Enthalpy
ΔH_{cal}	Calorimetric enthalpy
ΔHvH	van’t Hoff enthalpy
HPLC	High performance liquid chromatography
HT	High-tension
IDT	Integrated DNA Technologies
L-HCPL	Left-handed circular polarized light
LPL	Linearly polarized light

LSPR	Localized surface plasmon resonance
MC	Mitocymin
N twist	Northern twist
n-bonding	Non-bonding
NDDI	Nuclear dipole-dipole interactions
NMR	Nuclear magnetic resonance
NN	Nearest neighbors
NOE	Nuclear Overhauser effect
NOESY	Nuclear Overhauser Effect spectroscopy
PCR	Polymerase chain reaction
PEG	Polyethylene glycol
PEM	Photoelastic modulator
PMT	Photomultiplier tube
QCFF/ PI	Quantum Mechanical Consistent Force Field method for PI electrons
RF	Radio frequency
R-HCPL	Right-handed circular polarized light
RISC	RNA-Induced silencing complex
RMSD	Root mean squared displacement
RNA	Ribonucleic acid
ROE	Rotating Overhauser Effect
ΔS	Entropy
S twist	Southern twist

shRNA	short hairpin RNA
SPR	Surface plasmon resonance
T	Thymine
TDDFT	Time-dependent density functional theory
T_i	Time domains
T_m	Thermal melt temperature
TOCSY	Total Correlation Spectroscopy
tRNA	transfer RNAs
U	Uridine
UV-Vis	Ultraviolet-visible spectroscopy

Chapter 1: Introduction

1.1 Nucleic acids

Nucleic acids are a class of macromolecules responsible for the storage of genetic information and regulation of protein synthesis. The term nucleic acid was used by Richard Altmann (1889)[1] to describe the non-protein component of nuclein described by Fredrich Miescher in 1869 [2,3]. Later, Albert Kossel (1885-1901) isolated and characterized the four nucleobases that are used to form DNA: adenine[4], cytosine[5], thymine[6], and guanine[7]. Nucleotides constitute of three components: a pentose sugar moiety (2'-deoxyribose or ribose sugar), a phosphate group, and one of five canonical nucleobases, adenine (A), cytosine (C), guanine (G), thymine (T), and uridine (U)[8] (Figure 1.0 a). Nucleobases are divided into pyrimidines (C, T and U) and purines (A and G), which are cyclic and bicyclic heterocycles, respectively (Figure 1.1).

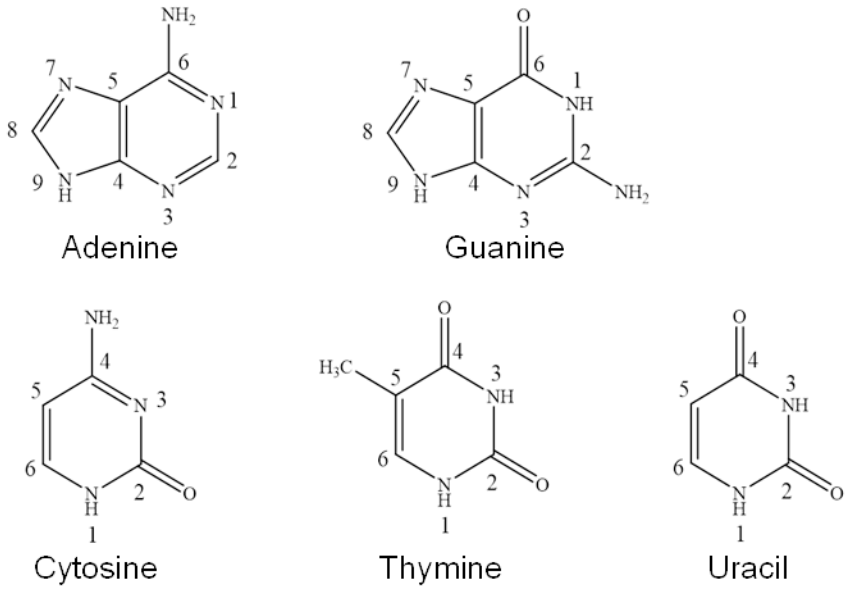

Figure 1.1. Structure of the nitrogenous bases

Nucleic acids encompass deoxynucleic acid (DNA) and ribonucleic acid (RNA)[8]. Nucleosides form DNA or RNA through the successive phosphodiester bonds between the 5'-OH and 3'-OH groups of the sugar moiety[8] (Figure 1.2). The sugar residues found in DNA and RNA are 2-deoxy-D-ribofuranose and 2-D-ribofuranose, respectively. Furthermore, the thymine nucleobase in DNA is replaced with uracil in RNA.

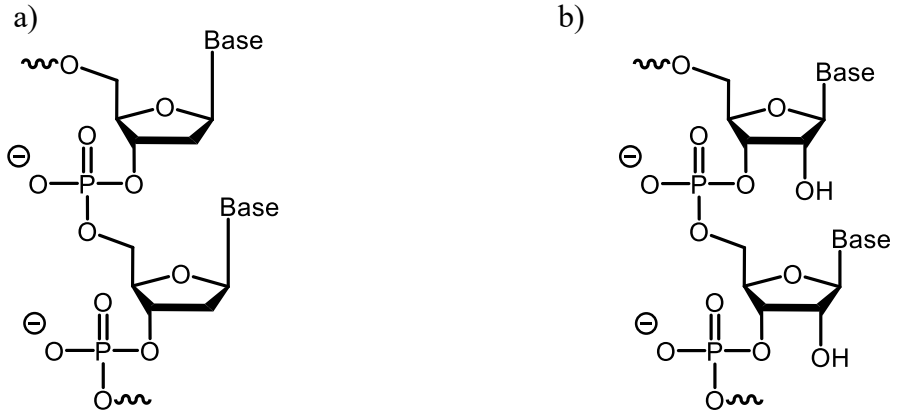

Figure 1.2. Structure of a) deoxyribonucleic acid b) ribonucleic acid. The wavy line represents that the nucleotide chain is connected to another nucleotide with either a deoxyribose or ribose sugar moiety. The word base is used to represent the nitrogenous base attached to the nucleotide chain.

1.2 Nucleic acid conformations

Nucleic acids can adopt various forms of conformers, conformers are isomers that possess an ability to interconvert by rotation of the molecule about a particular bond[9]. To quantify the conformation of a conformer an internal coordinate such as torsion angles is used.[10] A torsion angle is the angle formed between two intersecting planes where each plane consists of three atoms, as exemplified with butane in Figure 1.3.

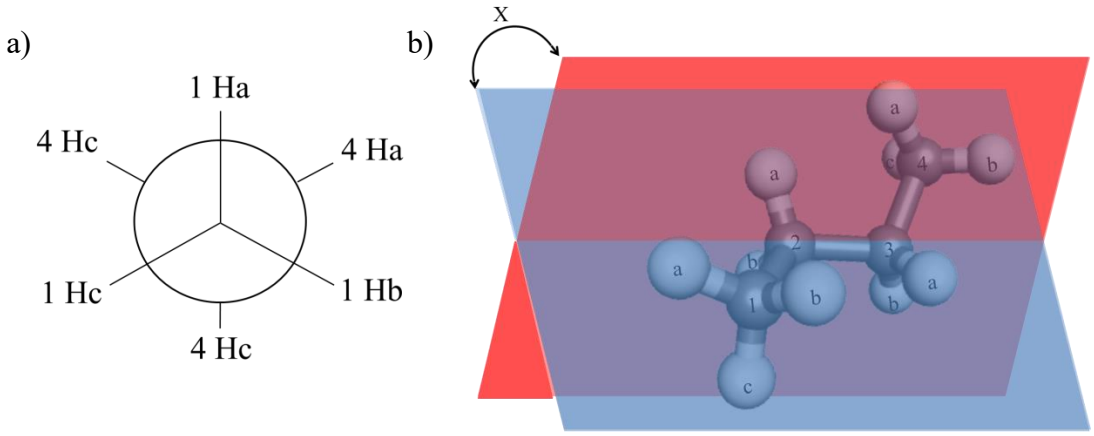

Figure 1.3. a) Newman projection of butane in the staggered conformation. b) Schematic of the dihedral angle for butane. The intersecting planes of atoms where X represents the torsion angle. The blue plane is composed of atoms 1, 2 and 3, and the red plane is composed of atoms 4, 3 and 2.

The value of a dihedral angle can be approximated using the Karplus equation, Equation [1][11,12]:

$$^{3}J_{HH} = A\cos^{2}\varphi + B\cos\varphi + C \qquad [1]$$

where $^{3}J_{HH}$ represents the J-coupling value between vicinal hydrogens, φ represents the dihedral angle, and A, B, and C are empirical values derived from parameters which relate to the substituents involved in forming the dihedral angle.

Rotation about a bond may be influenced by the hybridization of the atoms involved. For instance, in a furanose ring consisting of four carbon atoms and one oxygen atom linked in a ring, C1-C2-C3-C4-O4 the sp^3-sp^3 hybridization about the torsion angle bond at C2-C3 permits pseudorotation. Pseudorotation is a fictitious rotation used to describe the conformational change

of a molecule's configuration. This type of "rotation" is described by the displacements of atoms of a molecule which is equivalent to the rotation of a molecule. Pseudorotation is not a true rotation, as the latter would require that the motion of the atoms is perpendicular to the rotation and that there is no angular momentum about the axis of rotation.[13] This difference is demonstrated by the cartoon showing pseudoroation and true rotation of phosphorus pentafluoride (Figure 1.4).

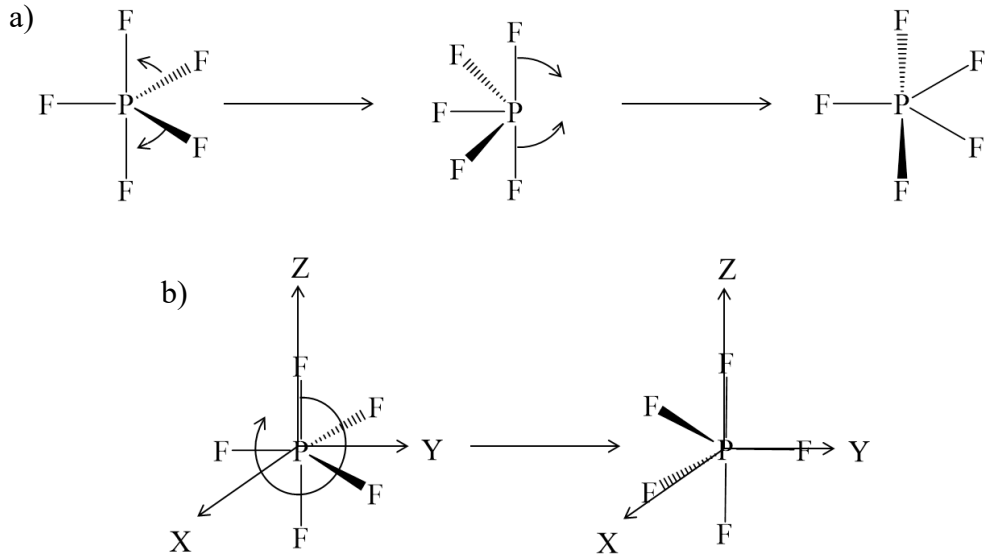

Figure 1.4. Cartoon representation depicting a) Berry pseudorotation. The curved arrows represent the displacement of two fluorine atoms around phosphorous atom b) rotation about an axis. The curved arrow represents the circular movement of phosphorus pentafluoride.

Pseudrotation allows the furanose ring in nucleic acids to display a degree of co-planarity where the C2'-C3' bond may protrude above (*endo*) or below (*exo*) the plane of the deoxyribose ring relative to C5'[14] (Figure 1.5). The equilibrium between the *endo* and *exo* conformations of the deoxyribose ring is known as sugar puckering[15]. Ring puckering occurs because of non-bonded interactions between substituents at the four carbons within the ring[16]. A

flat pentagonal ring system would set all the atoms in an eclipsed conformation with a bond angle of approximately 109.5^{o}[17]. Puckering relieves the steric conflict caused by eclipsed groups interfering with one another by allowing the bond angle to deviate[15]. Pseudrotation allows the ring system to achieve an energetically favourable environment where the substituents are as far apart as possible[15]. Qualitatively there are six conformations of the ribose ring about the C2'-C3' bond. If C2' is *endo* then the conformation adopted is described as a 2'-*endo* envelope ($^{2'}$E). Alternatively, if C2' is *exo* then the conformation adopted is described as a 2'-*exo* envelope ($E_{2'}$)[15]. Similarly, this is true if C3' is displaced in the ribose ring rather than C2'. If C2' is *endo* and C3' is *exo* then the conformation adopted is described as a northern twist (N twist). Conversely if C2' is *exo* and C3' is *endo* then the conformation adopted is described as southern twist (S twist)[18].

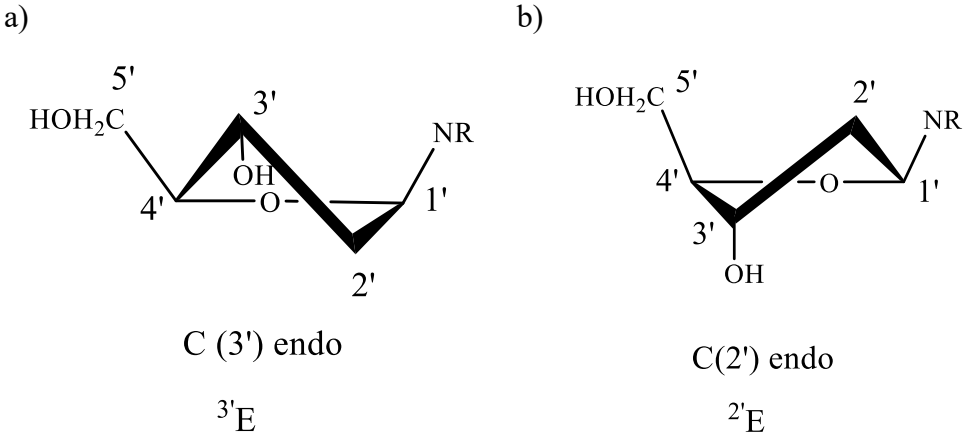

Figure 1.5. Representation of the pseudorotation of ring puckering in deoxynucleotides where NR represents the base.

To accurately describe the exact conformation about the deoxyribose ring and the continuum of the interconvertible ring puckers, internal coordinates such as torsion angles and the phase angle of pseudorotation are used[19]. In a study conducted by Altona and Sundarlingam

(1972) the conformation of the sugar ring in nucleosides and nucleotides was described using a series of torsion angles about the sugar ring[20]. These torsion angles are defined as follows: τ_0 represents the torsion angle C3'-C4'-O4-C1', τ_1 represents the torsion angle C4'-O4-C1'-C2', τ_2 represents the torsion angle O4-C1'-C2'-C3', τ_3 represents the torsion angle C1'-C2'-C3'-C4', τ_4 represents the torsion angle C2'-C3'-C4'-O4 (Figure 1.6 a)[20]. To quantitatively describe the conformation of the sugar ring, Altona and Sundarlingam used the maximum angle of torsion, τ_m, and the "phase angle" of pseudorotation, P (Figure 1.6 b). The phase angle of pseudorotation is a trigonometric expression used to indicate the type of pucker that the sugar ring adopts. The phase angle of psuedorotation can be expressed by the Equation [2][19]:

$$\tan P = \frac{(\tau_4 + \tau_1) - (\tau_3 + \tau_0)}{2 * \tau_2 \ * (sin36^o + sin72^o)} \quad [2]$$

where P represents the phase angle of pseudorotation, and $\tau_0 - \tau_4$ represents the five torsion angles that compose of the deoxyribose ring. The phase angle of pseudorotation can take any value between 0^o and 360^o, and it can be related back to the five torsion angles by Equation [3][19]:

$$\tau_i = \tau_m[P + \frac{4\pi(j-2)}{5}] \quad [3]$$

where j is equivalent to the values between 0 and 4, τ_m represents the maximum torsion angle; $\tau_m = \frac{\tau_2}{\cos P}$ [19]. From the expression, P is dependent on τ_m which, in turn, depends on the atom chosen as the first atom or origin atom (O4'). The torsion angle τ_2 is used in this expression because the pseudorotation about τ_2 possesses the largest puckering degrees of freedom because of the absence of steric hinderances (τ_3, τ_4, τ_1, τ_0) and dominating hybridization effects of the glycosidic bond (τ_0, τ_1).

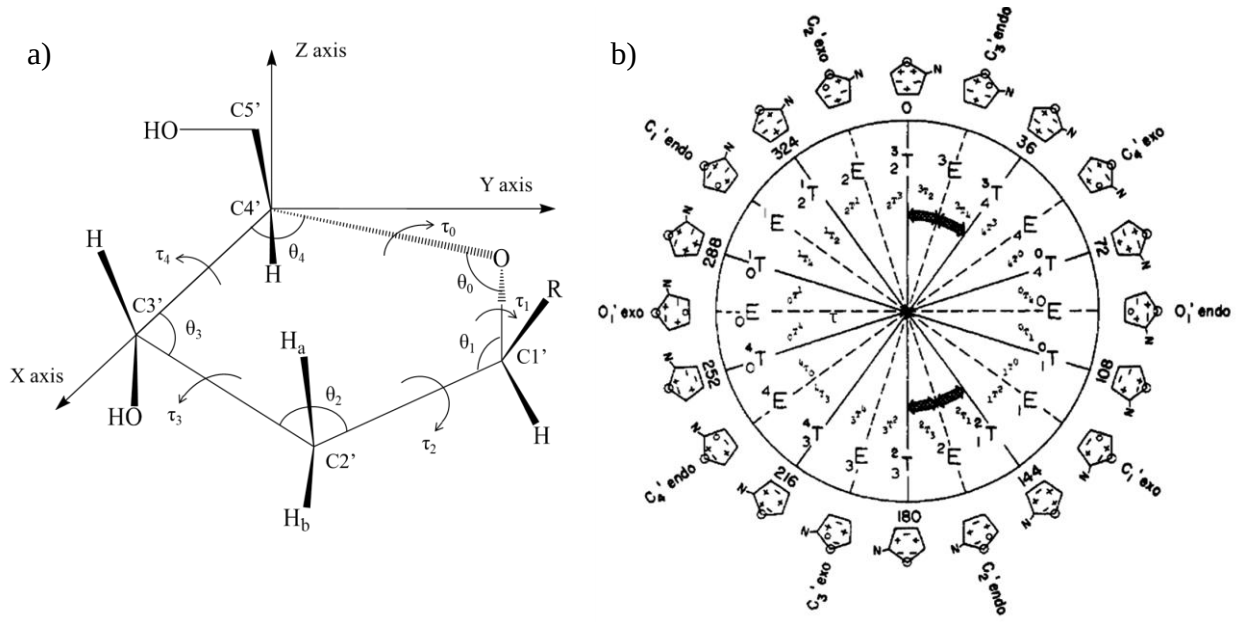

Figure 1.6. a) Representation of the deoxy ribose ring showing the ring atoms, the nitrogenous base (R), side-chain atoms, bond angles (θ_i), torsion angles (τ_j), and a coordinate system to express the Cartesian coordinates. Figure adapted from Tomimoto, M.; Go, N. Analytic Theory of Pseudorotation in Five-Membered Rings. Cyclopentane, Tetrahydrofuran, Ribose, and Deoxyribose. *Journal of Physical Chemistry.* **1995**, *99* (2), 563–577. b) Pseudorotation cycle of the ribose ring in nucleotides. The values of the phase angles (P) are given in multiples of 36°. The envelope and twist conformations alternate every 18°. The signs of endocyclic torsion angles are indicated on the ribose ring as either positive (+), negative (-), and zero (0). Figure used with permission from *Journal of the American Chemical Society*. 94, 23, 8205-8212 Copyright © 2018 American Chemical Society.

In comparison to the sugar puckering of the deoxyribose ring, the N-glycosidic bond that is formed between atoms C1' to N9 also permits pseudorotation (Figure 1.7). Pseudorotation about the N-glycosidic bond allows the nitrogenous base to protrude only outwards between 0 to 90° (*anti*) or between 120 to180° (*syn*) towards the ribose ring[21]. The dynamic transition around

the glycosidic bond is known as base flipping[22] and was first observed in DNA using X-ray crystallography by Klimasuskas and co-workers in 1994[23]. Rotation about the glycosidic bond is described as pseudorotation because of restricted rotation caused by the non-equivalent hybrid orbitals involved. In order for π bonds to form, complete sideway overlap of the p orbitals is required. As a consequence, all of the empty p orbitals must be in the same plane of the π system; this is possible when all atoms of the molecule are in the same plane[24]. In the case of N9, this nitrogen atom is sp^2 hybridized as it is part of a π bond system, thus N9 experiences limited rotation. Atom C1', on the other hand, is sp^3 hybridized and possesses free rotation. Because of the differences in hybridization the effects of N9 dominates over C1' there is a restriction in rotation about the N-glycosidic bond.

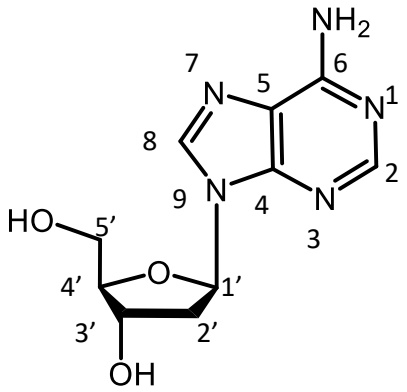

Figure 1.7. Structure of 2'-deoxyadenosine.

1.3 Secondary structures

Nucleic acids can adopt a variety of conformations depending on the nucleotide sequence, the proportion and type of base pairs, and how the base pairs are hydrogen bonded to one another[25–27]. The combination of nucleotides and variation of hydrogen bonding allow for the most favorable geometry that maximizes the efficiency of base pair stacking[28]. As a result of different base pairings and base stacking arrangements, nucleic acids can exist in different hybridized conformations, with the most well-known and biologically active being A-, B-, and Z-DNA [29–31] (Figure 1.8). Each conformation of DNA is favoured under different conditions, and differ in their handedness, helical turn, sugar pucker, and glycosidic bond dihedral angle[32,33], as summarized in Table 1.1.

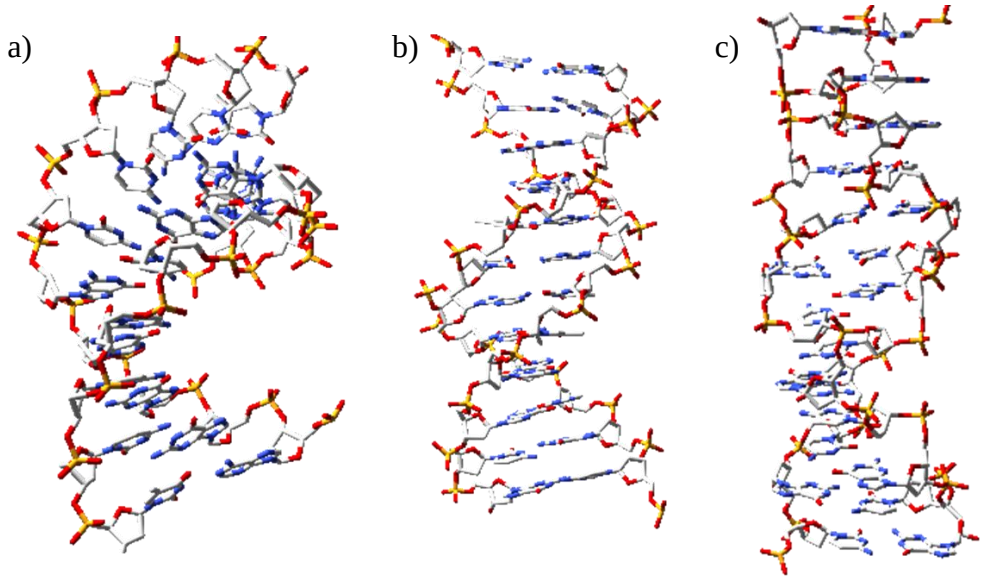

Figure 1.8. Structures of a) A-DNA, pdb ID: 440D, b) B-DNA, pdb ID: 1BNA, and c) Z-DNA, pdb ID: 4OCB. The figures were prepared using the image rendition software's Swiss PDB and POV-RAY

Table 1.1. Summary of the structure of A-, B-, and Z-DNA.

Conformation*	A-DNA	B-DNA	Z-DNA
Handedness	Right	Right	Left
Sugar pucker †	C3'-*endo*	C2'-*endo*	dG: C3'-*endo* dC, dT, dA: C2'-*endo*
Glycosidic bond † ‡	*Anti*	*Anti*	G: *Syn* dC, dT, dA: *Anti*
Base pairs per turn	11	10	12
Axial rise (nm)	0.26	0.34	0.45
Helical pitch (°)	28	34	45
Base pair tilt (°)	20	-6	7
Twist angle	33	36	-30
Diameter of helix (nm)	2.3	2.0	1.8

* The hairpin conformation was not shown because of limited information available and the variable nature of the conformation.

† Describes the conformation of the sugar pucker or glycosidic bonds for each of the four canonical nucleotides unless otherwise stated.

‡ *Anti* and *syn* refers to the orientation of the *N*-glycosidic bond between the base and deoxyribose moiety. In the *anti*-conformation, the base extends away from the deoxyribose

moiety. On the other hand, for the *syn*-conformation, the base is above the deoxyribose moiety. The *syn* and *anti*-conformations are further described in Chapter 2.

Table recreated from Ussery, D. "DNA Structure: A-, B- and Z-DNA Helix Families," 2002 and Nakamoto, K.; Masamichi, T.; and Gary D. S.; *Drug-DNA Interactions: Structures and Spectra*. John Wiley & Sons, 2008.

B-DNA is the most common double helical structure in nature and was discovered in 1953 by Watson, Crick, Wilkins, and Franklin[29,30]. B-DNA exists at neutral pH and physiological salt concentrations. B-DNA appears as a double stranded (ds) right-handed helix that is about 20 Å wide with 10-10.5 base pairs per turn[34]. B-DNA possesses a hydrophilic backbone with negatively charged phosphate groups positioned on the outside of the helix. In canonical Watson-Crick base pairing two hydrogen bonds are formed between adenine and thymine, and three hydrogen bonds are formed between cytosine and guanine[35] (Figure 1.9). In B-DNA the sugar moiety adopts a sugar pucker where the C2' atom protrudes above (*endo*) to the plane of the deoxyribose ring[32]. Additionally, all of the nucleobases are arranged in the *anti*-conformation with respect to the position of the sugar moiety[32]. B-DNA consists of alternating partitioned regions called the major and minor groove. The major and minor grooves are formed because the angles of the glycosidic bonds between complementary base pairs are not diametrically opposite to one another, causing the sugar of the nucleotide to protrude outward. The major and minor grooves run continuously along the entire length of the duplex resulting in

deep, wide and narrow depression respectively[32].

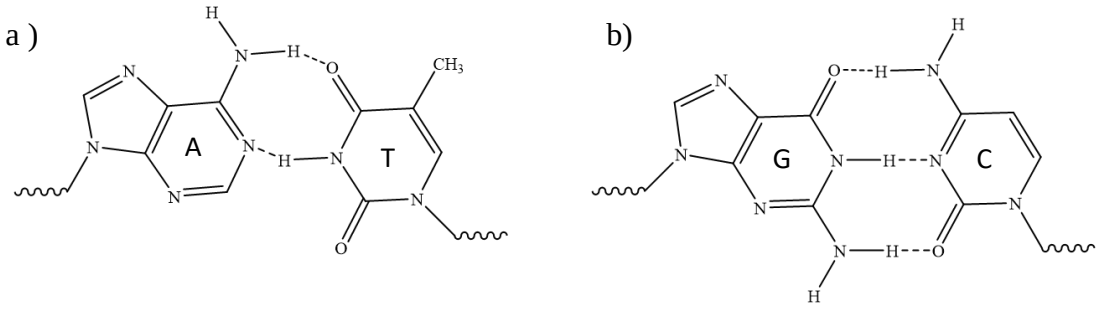

Figure 1.9. Watson-Crick base pairing. a) adenine-thymine and b) guanosine-cytosine.

The structure of A-DNA was discovered in 1953 by Franklin and Gosling[29]. A-DNA occurs when B-DNA is subjected to dehydrating conditions. Similar to B-DNA, A-DNA appears as a right handed coil, all of the nucleobases are in the *anti*-conformation, and possess Watson-Crick base pairing. Unlike B-DNA, A-DNA is 23Å wide with 11 base pairs per turn and appears broader and more compressed. The sugar moiety in A-DNA is puckered in the C3'-*endo* conformation, and the base pairs are not perpendicular to the helix-axis. The major and minor groove depressions become deep and narrow, and shallow and wide respectively[32, 34].

The structure of left-handed Z-DNA was discovered in 1970 by Wells and colleagues when studying a sequence composing of alternating deoxyriboinosinic acid and deoxyribocytidylic acid residues[31]. The structure of the Z-DNA was detected by circular dichroism spectroscopy and the B→Z transition was reported by Pohl and Jovin in 1972[36]. Later in 1979 the structure of Z-DNA was elucidated by Wang and colleagues for $d(CG)_3$ using X-ray crystallography[37]. Unlike B-DNA and A-DNA, Z-DNA is left handed and is the higher-energy form of the double helix[38]. The Z-DNA duplex is about 18Å wide with 12 base pairs per turn[34] and resembles a zigzag pattern. The sugar pucker for dC and dG is altered, where dC and dG

adopt the C2'-*endo* and C3'-*endo* conformation, respectively[32]. The major and minor grooves of Z-DNA do not differ in width. Unlike B-DNA there is limited evidence to suggest that Z-DNA does not exist as a stable conformation *in vivo*[39]. Under physiological conditions the negatively charged phosphate groups possess strong destabilizing electrostatic repulsion that favours the B-DNA conformation[40]. Z-DNA has been found to occur under high salt concentrations, cationic environments, by the use of organic/inorganic modifiers, or chemical modification such as cytosine methylation[41]. On the other hand, Z-DNA has been found to occur transiently in B-DNA in regions with alternating pyrimidines and purines such as deoxyguanosine and deoxycytidine respectively[42]. When sections of Z-DNA form in a helix that is primarily in the B-DNA conformation the region where the two conformations meet is known as the B-Z junction[19,38](Figure 1.10).

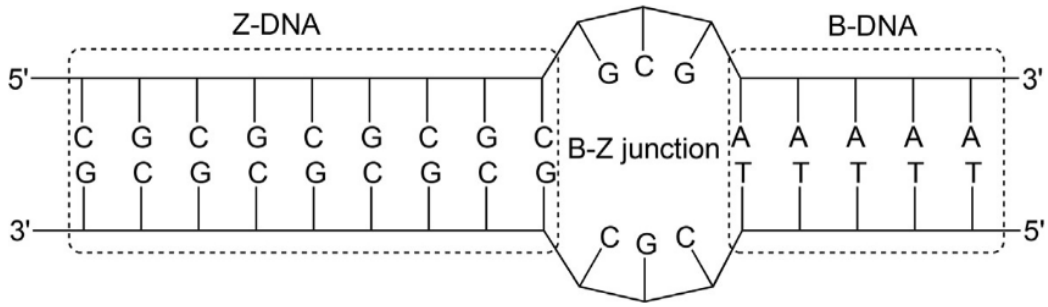

Figure 1.10. Structure representing a heptadecamer featuring segments of B- and Z-DNA and a 3-base B-Z junction. Figure was reproduced with permission from Yan, H.; Powers, R.; Gibbons, A.; Joshi, D. (2017) Z-DNA: Chemistry and Biological Relevance. In: Reedijk, J. (Ed.) Elsevier Reference Module in Chemistry, Molecular Sciences and Chemical Engineering. Waltham, MA: Elsevier.

The possibility of Z-DNA possessing biological significance was first postulated by Wells and colleagues[31]. Support for this hypothesis came from a study by Rich and colleagues

(1982) [42]. Here Rich and colleagues examined plasmid DNA with an alternating d(pCpG) insert ranging from 24-42 bp in the presence of NaCl or cobalt hexammine ($Co(NH_3)_6^{3+}$). Rich and colleagues performed sedimentation and gel electrophoresis to assess if a change in conformation of the insert from right-handedness to left-handedness had occurred[42]. It was found that under physiological conditions the formation of Z-DNA is favoured provided sufficient negative supercoiling of the plasmid DNA[39]. DNA supercoiling is caused by the over- or under-winding of a DNA strand that can release the torsional stress[43]. Negative supercoiling occurs when a DNA helix is unwound, while positive supercoiling occurs when a DNA helix is over wound[43]. Z-DNA is found to exist when a negatively supercoiled plasmid is unwound[39]. The energy required to form a negative supercoiling is instead used to stabilize the Z-DNA forming region[39]. The significance of Z-DNA being present in a negative supercoiling event suggests that Z-DNA may play a role in controlling gene expression by providing relief from torsional strain during transcription[38,44]. In a study conducted by Liu and Wang (1987), it was found that when RNA polymerase complexes to DNA, RNA polymerase unwinds the DNA molecule rather than rotating around the helix[45]. With the ends of the DNA molecule being fixed during translation, the section in front of RNA polymerase becomes overwound, while the sections of DNA behind RNA polymerase become unwound. This mechanism allows for the formation of negative supercoils and possibly the stabilization thereof by Z-DNA[39,45]. The formation of Z-DNA can regulate transcription by blocking trailing RNA polymerases from actively transcribing[46]. However, some studies showed that the influence of Z-DNA on transcription is dependent on the gene being examined[39]. Because of the inconsistency of the proposed mechanism, support for the claim that Z-DNA was a non-functional conformational phenomenon was favoured[39]. The first real evidence that suggested that Z-DNA had a biological function was provided by Rich and

colleagues where polyclonal[47] and monoclonal[48] anti-Z-DNA antibodies were shown to recognize Z-DNA. The significance of these anti-Z-DNA antibodies led to the discovery of Z-DNA-specific antibodies in human autoimmune diseases[49,50] and later Z-DNA binding proteins[51]. In a study conducted by Herbert and colleagues (1995), a Z-DNA-binding protein from chicken lung tissue was purified and was later identified as RNA adenosine deaminase (ADAR1)[51]. ADAR1 is an RNA editing enzyme that binds to double stranded regions of nuclear-encoded RNA and viral RNA formed in pre-mRNA and converts adenosine to inosine by deamination[52,53]. Inosine is a molecule that shares some resemblance to guanine with the exception that the exocyclic amine at position two is replaced with a hydrogen atom. The conversion of adenosine to inosine regulates gene transcription and supresses innate immune response to endogenous RNA. The binding of Z-DNA/Z-RNA to the Zα domain of ADAR1 has been found to facilitate multiple biological processes such as, altering stress granules, altering the selectivity of ADAR1-editing site and dsRNA substrates leading to enhanced editing of ds RNAs[52], preventing dysregulated interferon response in autoimmune disorders such as Aicardi-Goutieres syndrome, and Bilateral striatal Necrosis/Dystonia[52], and localization of $ADAR_{1p150}$ to stress granules[52,54]; a collection of proteins and RNAs in the cytosol that occurs during cellular stress. Although there is evidence of Z-DNA being present in biological systems, the biological function(s) of Z-DNA still remains mostly elusive[55].

Unlike A-, B-, and Z- DNA, the hairpin or hairpin loop consists of a single strand of RNA or DNA that is folded in on its self, forming the stem and the loop (Figure 1.11). The stem consists of self-complementary regions where nucleotides that read in opposite directions form hydrogen bonds with one another. The loop on the other hand is single stranded and consists of unpaired nucleotides that loop outwards forming the end of the hairpin. The formation of a

hairpin conformation is dependent on the stability of the stem and loop regions, which are related to the length, size of the loop, and the type of nitrogenous base in the sequence[56,57]. The hairpin conformation was known sometime around the early-mid 60s and was referred to as a helix-random coil until the late 60s where the term hairpin was used to describe the conformation[58]. During the 60s-70s some examination on the hairpin conformation was performed. Studies on the hairpin conformation at the time consisted of thermal analyses[59], folding dynamics[58], X-ray crystallography[60], electron microscopy[61], and polyacrylamide gel electrophoresis[58], and some *in silico*[62] approaches.

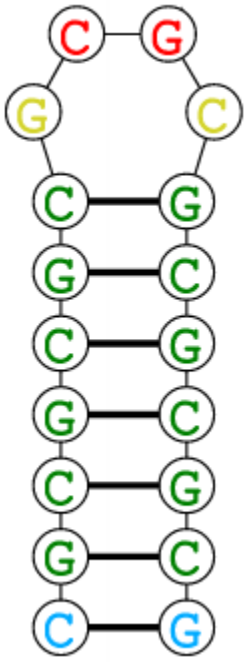

Figure 1.11. Cartoon representation of a hairpin conformation. The image was generated using the RNAstructure webserver Reuter, J.S.; and Mathews, D.H. (2010). RNAstructure: software for RNA secondary structure prediction and analysis. BMC Bioinformatics.11,129.

In biological systems hairpin conformations occur as a secondary structure of RNA strands that possesses palindromic sequences. As an example, transcription in prokaryotes is

halted either through rho-dependent or rho-independent termination[63]. The difference between rho-dependent or rho-independent termination is the use of a rho factor such as a helicase protein to terminate transcription[63,64]. In rho-independent termination or intrinsic termination, transcription is halted by a process known as attenuation, which involves the physical modification of the synthesized RNA molecule[65]. During attenuation the synthesized RNA adopts a hairpin structure that binds to a protein called nusA, which subsequently binds to RNA polymerase[66]. When the polymerase reaches the polyA region on the template strand during transcription, the hairpin-nusA complex causes RNA polymerase to temporarily stall, which allows for destabilization of the RNA-DNA duplex to be more favourable[64,66].

Hairpins are also found in transfer RNAs (tRNA), which are approximately 76-90 nucleotides in length[67]. The secondary structure of tRNA resembles a clover leaf, with three loop regions, and an L-shaped tertiary structure (Figure 1.12). tRNA is used during protein synthesis to transfer amino acids to elongating peptide chains. A tRNA molecule is composed of an amino acid attachment region or acceptor stem that forms an ester bond with amino acids, and an aminoacyl-tRNA synthetase recognition site[8].

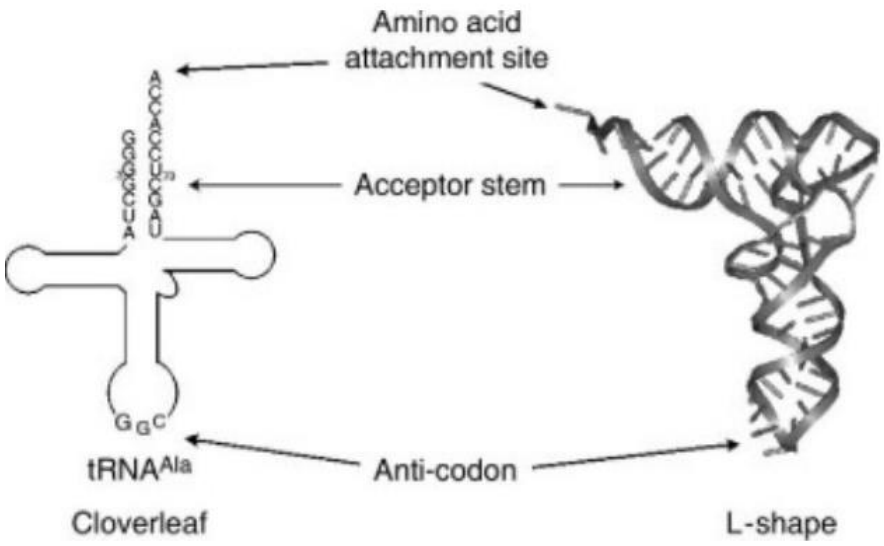

Figure 1.12. Secondary (left) and tertiary (right) structure of a hairpin conformation. Figure used with permission from Ewalt, K.L.; and Schimmel, P. "tRNA Synthetases." In *Encyclopedia of Biological Chemistry*, edited by William J. Lennarz and M. Daniel Lane, 263–66. New York: Elsevier, 2004.

Aside from transcription and translation, there have been uses for hairpins in biotechnological aspects. As an example, short hairpin RNA (shRNA) is an artificial dsRNA molecule that is used to silence targeted gene expression[68]. Expression of shRNA in cells is achieved by transfection or transformation[68]. Transfection and transformation are processes where foreign DNA/RNA is introduced into a cell's nucleus[68]. The difference between transfection and transformation is the type of cell that is used to integrate foreign oligonucleotide strands into the host cell. Transfection typically uses a viral vector to infect mammalian cells, while transformation uses a plasmid vector to infect bacterial, yeast, or plant cells[8,63]. To introduce the shRNA sequence, the shRNA sequence is incorporated into a plasmid which is delivered to a cell by a bacterial or viral vector. The gene for the shRNA is transcribed and the mRNA transcript folds in on itself forming pri-shRNA. pri-shRNA is processed by a series of

enzymes, forming pre-shRNA before being transferred out of the nucleus using a protein known as exportin[68]. Pre-shRNA differs from pri-shRNA where pre-shRNA possesses a two nucleotide overhang at the 3'end. Once in the cytoplasm pre-shRNA is further processed by enzymes to form mature shRNA[68]. Mature RNA differs from pre-shRNA where the loop region is cut off by an RNase type enzyme forming an RNA duplex with a two-nucleotide overhang at the 3' end on the passenger strand[68]. The mature shRNA is further processed where the passenger strand is degraded by Ago II forming an RNA-Induced silencing complex (RISC)[68]. Depending if the guide strand is completely complementary to the gene of interest RISC act one of two ways: 1) if the guide strand is completely complementary to the gene of interest, RISC will repeatedly bind to and degrade the mRNA of the target gene[68]; 2) if the guide strand is partially complementary to the gene of interest, RISC will bind to the gene of interest and repress translation of the mRNA[68]. In either case the RISC complex effectively hinders the expression of the gene product.

1.4 Denaturation

Denaturation is a process where the structural topology of the native state of biomolecules such as nucleic acids is altered[69]. Denaturation can be achieved using physical or chemical stimuli such as using heat, sonication, or organic modifying agents[69]. Examples of organic modifying agents include urea[70], formamide[71], dimethyl sulfoxide (DMSO)[71], and guanidinium hydrochloride[72]. Denaturation of dsDNA is an import event in many biochemical and biological processes, such as polymerase chain reaction (PCR) and sequencing.

Mechanistically most denaturing agents interact with DNA by disrupting the formation of hydrogen bonds[73]. Denaturation of dsDNA can be examined by the change in absorbance at 260 nm, called the hyperchromic effect (Figure 1.13)[74].

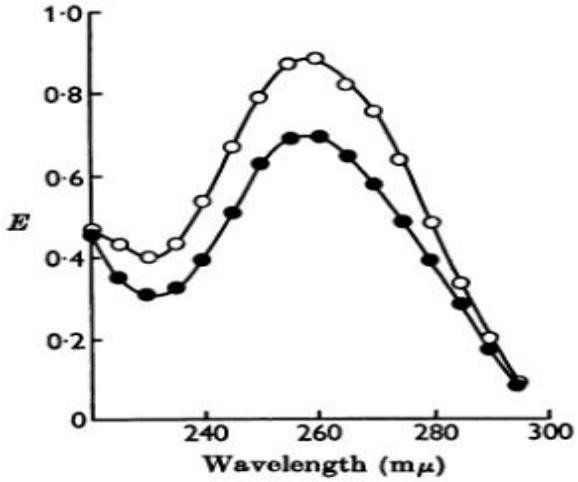

Figure 1.13. Hyperchromicity of DNA from Landschutz-ascites-tumour cells, thermally denatured in 0.167 mM NaCl. •Native DNA; ◦, thermally denatured DNA. Figure used with permission from: Keir, H.M.; B. Binnie.; and R. Smellie. "Factors Affecting the Primer for Deoxyribonucleic Acid Polymerase." *The Biochemical Journal*, 1962.

The hyprochromic effect refers to an increase in UV-Vis absorption when dsDNA is denatured into two single strands of DNA. It is presumed that the overall induced dipoles are enhanced as dsDNA denatures, leading to increases in absorbance. The degree of hyperchromicity varies on the sequence of DNA being examined. It was reported in the literature that complete denaturation can lead to 30-40% increases in absorbance at 260 nm[75–78]. The percent hyperchromicity is calculated by Equation [4][79];

$$\%\ hyperchromicity = \frac{Final\ A_{260} - Initial\ A_{260}}{Final\ \ A_{260}} \times 100 \qquad [4]$$

where $Initial\ A_{260}$ and $Final\ A_{260}$ represent the absorbance of the DNA sample before and after denaturation, respectively.

1.5 Common techniques used in the study of DNA structures

1.5.1 Ultraviolet-visible (UV-Vis) spectroscopy

Ultraviolet-visible (UV-Vis) spectroscopy is an analytical spectroscopic technique that uses light in the ultraviolet and visible range to obtain the absorbance or reflectance spectrum of a sample at a single wavelength. Absorbance refers to a measure in the quantity of light absorbed by a sample[80], while reflectance relates to the loss in energy that a surface reflects[81]. UV-Vis absorption occurs when light is absorbed by an analyte, leading to electronic transitions or surface plasmon resonance (SPR)/ localized surface plasmon resonance (LSPR) depending on the analyte. During electronic transitions molecules containing electrons from bonding or non-bonding (n-bonding) orbitals such as conjugated systems are irradiated with ultra-violet light. The transfer of energy causes the electrons to become excited from a lower energy state (ground state) to a higher energy state (excited state)[82]. SPR, on the other hand, occurs when a metal sheet is irradiated with a beam of electromagnetic radiation. When the light hits the metal surface at a specific angle, the resonance angle, some of the energy is absorbed while the majority of light is reflected at a lower wavelength[83] (Figure 1.14a). The transfer of energy causes the electrons at the interface between the metals surface and the environment to resonate and oscillate[84]. The collective oscillation of the resonating electrons is known as surface plasmon resonance[83]. In comparison to SPR, LSPR on the other hand, involves nanoparticles and possesses a localized surface plasmon. In other words, the surface plasmon is restricted to a smaller space than SPR[84] (Figure 1.14b,c). LSPR compared to SPR allows for a number of advantages depending on the application such as: reduced cost and complexity, prism and resonance angle is not required, decreased evanescent field, increased sensitivity, and detection of wavelength shift in real-time.

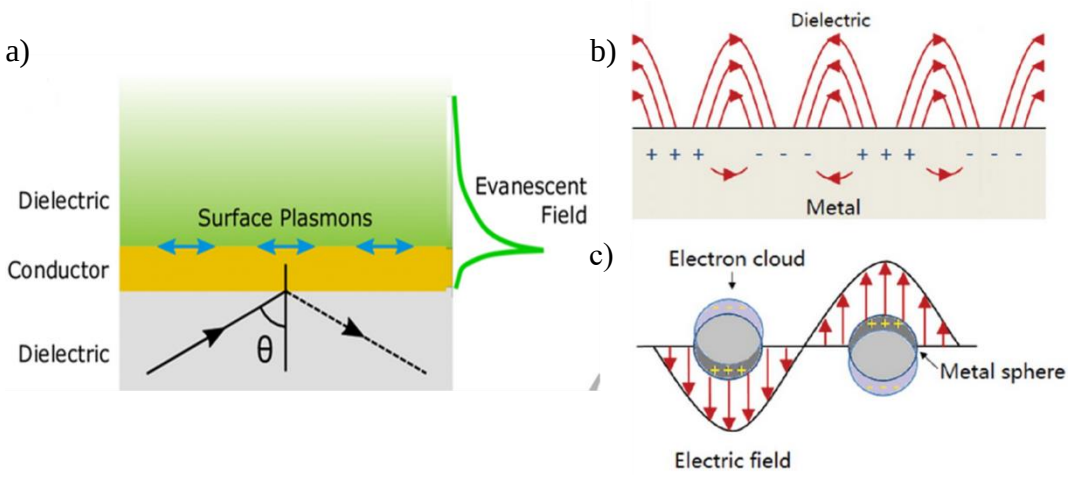

Figure 1.14. a) Diagram representing the occurrence of surface plasmon resonance between two dielectric media, and the generated evanescent field that decays as a function of distance. Figure used with permission from Howe, C.L.;Webb, K.F.: Abayzeed, A.A.; Anderson, D.A.; and Russel, N.A. "Surface Plasmon Resonance Imaging of Excitable Cells." *Journal of Physics D: Applied Physics* 52, no. 10. 2019: 104001. Cartoon representation of b) surface plasmon in a metal film and c) localized surface plasmon in nanostructures. Figures b) and c) used with permission from: Xiaowei,G. "Surface Plasmon Resonance Based Biosensor Technique: A Review." *Journal of Biophotonics* 5, no. 7. 2012: 483–501.

To quantify the amount of attenuation of light when an analyte is irritated the following expression known as the Beer-Lamberts law can be used Equation [5][85,86]:

$$A = \varepsilon c l \qquad [5]$$

where A represents the absorbance of the analyte, ε represents the molar extinction coefficient with the units ($M^{-1}cm^{-1}$), c represents the concentration of the analyte with the unit M, and l represents the pathlength of the vessel used with the unit cm[87].

1.5.2 Electronic circular dichroism (CD) spectroscopy

Electronic circular dichroism (CD) spectroscopy is a technique that is used to examine optically active chiral molecules in solution[88] or the solid state[89]. CD spectroscopy is used in a wide range of applications ranging from studying changes in conformation of biomolecules[90], investigating the mechanisms of action of proteins[91], and determining magnetic optical activity of paramagnetic systems[92]. CD spectroscopy has been employed to examine conformational changes of biomolecules when subjected to various conditions. As an example, three forms of DNA duplexes, A-, B- and Z-DNA, can be readily distinguished by CD spectroscopy (Figure 1.15).

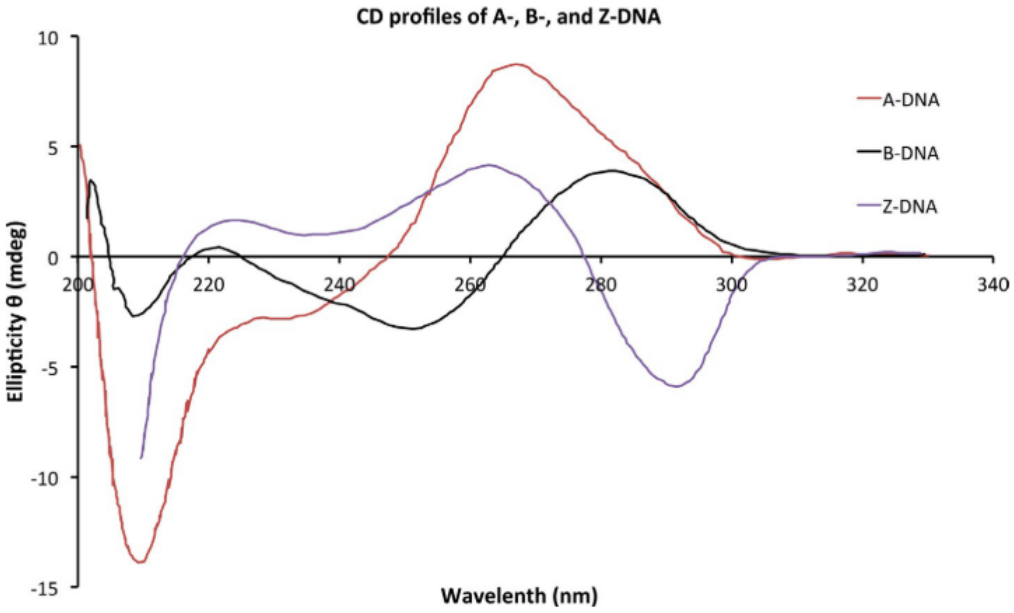

Figure 1.15. CD spectrum of A-DNA, B-DNA, and Z-DNA. Figure used with permission from Yan, H.; Powers, R.; Gibbons, A.; Joshi, D. Z-DNA: Chemistry and Biological Relevance. Reference Module in Chemistry, Molecular Sciences and Chemical Engineering. 2017, 1–14.

Although CD spectroscopy is a direct and convenient technique to assess the presence of chiral compounds, the deconvolution of the CD profile can be difficult, especially for complex systems[93]. As an example, Tomasz and colleagues (1983) used CD spectroscopy to examine the effect of mitocymin (MC) on the structures of poly(dG-dC) duplexes and *Micrococcus lysodeikticus* DNA. It was found complexation of MC to DNA led to the observation of CD profiles that were reminiscent to that of Z-DNA, however, further investigations revealed that MC does not induce B→ Z-DNA transition, instead it inhibits such a transition.

CD actively measures the difference in absorption by an analyte when irradiated with left-handed circular polarized light (L-HCPL) and right-handed circular polarized light (R-HCPL). The absorption of L-HCPL and R-HCPL can be expressed by modified Beer-Lampert equation, Equation [6][88]:

$$CD = \Delta A = (\varepsilon_L - \varepsilon_R)cl \qquad [6]$$

where ΔA represents the difference in absorbance, ε_L and ε_R represent molar coefficients for L-HCPL and R-HCPL respectively, c represents the molar concentration, and l represents the pathlength of the cuvette used[88].

Most CD spectrophotometers measure the difference in absorbance in elliptical units (θ) in degrees. The conversion of absorbance units to elliptical units is described by Equation [7][88]:

$$\theta = 32.98\,\Delta A \qquad [7]$$

where θ represents the absorbance in elliptical units, and ΔA represents the difference in absorbance in absorbance units[88].

Light is a form of electromagnetic radiation that consists of an electric field, $\vec{E}$, and a magnetic field, $\vec{B}$, that are equivalent in amplitude, oscillate perpendicular to one other, and propagate in the same direction[94,95]. CD machines usually use a xenon arc lamp as a light source[96]. The light emitted by the xenon arc lamp is un-polarized, which vibrates in all planes[97]. The un-polarized light travels through a monochromator and then a polarizer to produce linearly polarized light (LPL) [96]. Circular polarized light results when LPL travels through a filter called a photoelastic modulator (PEM). The PEM is a resonant device that resonates between 50-100 kHz and changes the polarization state of a light beam by actively shifting the electric field by $\pm 90^o$ relative to the magnetic field at a set frequency, and generates alternating current (AC) that is detected by a lock-in amplifier. R-CPL or L-CPL is produced if the electric field is shifted by $+90^o$ or -90^o respectively. [96, 98–101]. When looking down the axis of propagation the resultant polarization vector from the contributions of the electric and magnetic field vectors traces out a circle over the period of one wave frequency[98] (Figure 1.16).

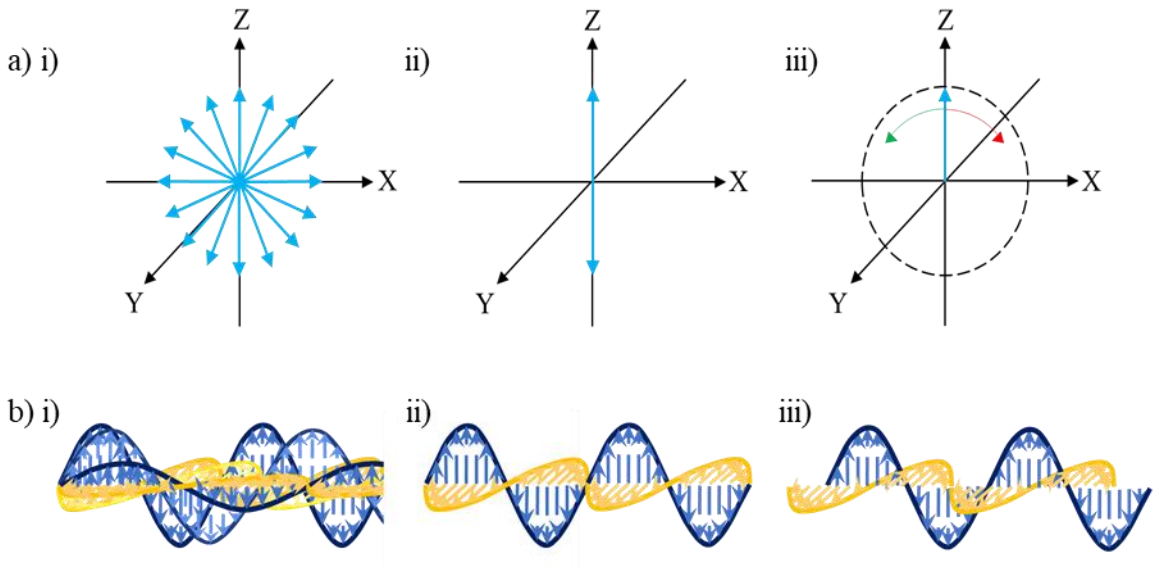

Figure 1.16. a) Cartoon representation of the magnetic vector (light blue) of i) un-polarized light, ii) linearly polarized light and iii) circularly polarized light. The red and green arrows represent right-handed and left-handed circularly polarized light, respectively. b) Cartoon representation of i) un-polarised light, ii) linearly polarized light, and iii) circularly polarized light. The dark blue and yellow sinusoids represent the magnetic and electric field, respectively. Figure a) reproduced from: Bijan, R.; and Gill, P. "Circular Dichroism Techniques: Biomolecular and Nanostructural Analyses- A Review." *Chemical Biology & Drug Design* 74, no. 2 (2009): 101–20. Figure b i) reproduced from Marvel,K.B. *Astronomy Made Simple: A Clear Guide to the Workings of the Universe*. Crown, 2010. Figure b) ii-iii) reproduced from Steiner, R.F.; and Garone,L. The Physical Chemistry of Biopolymer Solutions: Application of Physical Techniques to the Study of Proteins and Nuclei Acids. World Scientific, 1991.

To detect the difference in absorbance of circularly polarized light a photomultiplier tube (PMT) is used. A PMT consists of a photocathode and a series of dynodes called electron multipliers[102]. The arrangement of the photocathode and electron multiplier acts to convert

incident light into electrons and amplify the current produced. When the photocathode is illuminated with a single photon an electron is ejected[102]. The ejected electron is accelerated by a focusing electrode into a dynode array that releases additional electrons that increases the current[100]. During each scan the current is kept constant by an applied voltage, converting the variable current into direct current (DC). The applied voltage is also known as the dynode voltage, high-tension (HT) voltage, detector, or PMT HV depending on manufacturer of CD machine used[98]. The DC output from the PMT can be measured to monitor the light intensity or photon flux over time during the scan[102]. It is worth mentioning that, although Equation [4] is how CD spectroscopy is conventionally understood, the definition of the CD signal is actually the ratio of DC/AC output, and can be described by Equation [8][103];

$$A = log_{10}\left(\frac{2 + AC/DC}{2 - AC/DC}\right) \quad [8]$$

where A represents the absorbance, and the ratio of AC/DC current corresponds to the difference in light intensity of L-CPL (I_L) or R-CPL (I_R) and is described as follows; $\frac{AC}{DC} = \frac{2(I_L - I_R)}{I_L + I_R}$ [103].

The AC and DC current are then transformed into a signal by a computer interface where data acquisition, storage manipulation, and digital plotting are performed. Figure 1.17 shows the schematic of a CD spectrometer.

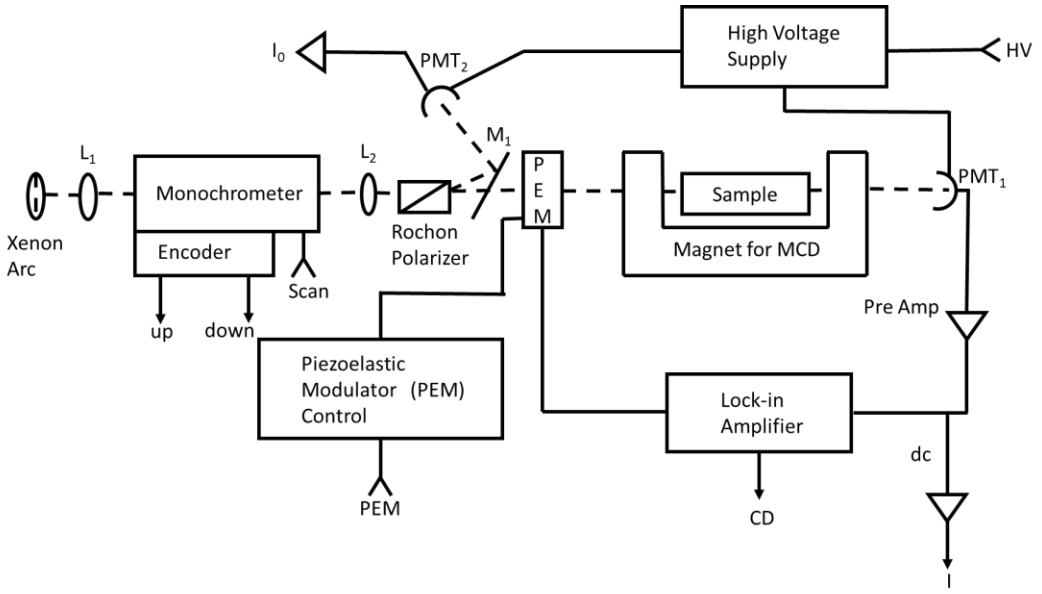

Figure 1.17. Schematic diagram of a circular dichroism spectrophotometer. Figure adapted from Mason, W.R. Spectrometer for Simultaneous Measurement of Absorption and Circular Dichroism Spectra. *Analytical Chemistry* 1982, *54* (4), 646–648.

1.5.3 Nuclear magnetic resonance (NMR) spectroscopy

Nuclear magnetic resonance (NMR) spectroscopy is a spectroscopic technique that uses energy in the form of electromagnetic radiation (60–1000 MHz) to exploit the intrinsic angular momentum or nuclear spin properties of atomic nuclei to help elucidate structures of a sample[104]. Nuclear spin is an innate property to isotopes/atoms that contain an odd number of protons and/or neutrons and cannot be changed[82]. NMR spectroscopy examines the nuclear spin of atoms through subjecting a chemical compound or bio-molecule to a magnetic field. An NMR signal is produced by the excitation of the nuclei in the sample when irradiated with a radio frequency (RF) pulse[104]. The nuclei then relax back down to the ground state; it is the relaxation of the nuclei that is detected with radio receivers to give rise to the signals on a spectrograph[104].

Depending on how the analyte is irradiated, the use of NMR spectroscopy allows for a plethora of quantitative structural information for a sample to be determined.

1.5.4 Two dimensional (2D) NMR spectroscopy

Although one-dimensional (1D) NMR spectroscopy is useful for probing the chemical environments of nuclei in molecules, the information that can be obtained may be limited, especially for more complex molecules. Two-dimensional (2D) NMR spectroscopy methods are used to give more insight on how nuclei are coupled to each other[105]. A 2D NMR spectra is characterized by a frequency co-ordinate system and can be expressed by a graph that possesses F1 (x) and F2 (y) frequency axes (Figure 1.18 a). Signals that correlate to the coupling of two nuclei are called cross peaks, while signals that correlate to a nucleus that couples to itself is referred to as a diagonal peak[104] (Figure 1.18 b).

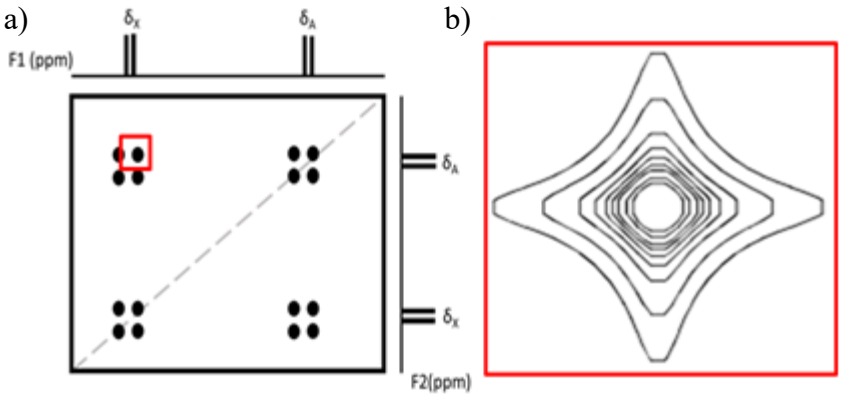

Figure 1.18. a) Cartoon representation of a 2D homonuclear correlated spectroscopy b) Illustration of a cross-peak as a contour plot. The red box in A and B highlights a cross peak. Figure adapted from Derome, A. E. *Modern NMR Techniques for Chemistry Research*. Elsevier, 2013.

2D NMR methods and by extension multipulse NMR experiments proceed through an algorithmic process. The timing, frequencies, and intensities of the RF pulses vary among the different types of NMR experiments performed[106]. 2D NMR pulses are broken up into four stages or time domains (T_i), preparation, evolution (T_1), mixing , and acquisition/detection (T_2)[107]. Preparation involves the formation of a non-equilibrium spin state using a RF pulse to promote specific atoms to a higher energy level[108,109]. Spin-active nuclei are represented by a nuclear spin magnetization field vector (M). The promotion of spin-active nuclei causes M to rotate in a direction opposed to the orientation of the applied magnetic field[104]. During the evolution phase the nuclear spins are allowed to freely precess or relax[104]. The resultant signal is recorded as the first time variable, T_1[104]. During the mixing period the magnetization is transferred from the irradiated nucleus to a second nucleus[104]. Additionally the molecule is subjected to another series of pulses where the coherence is further manipulated[104,110]. The duration of the mixing time τ_m is of a fixed value and depends on the size of the molecule of interest[111]. Acquisition occurs directly after the pulse sequence and involves recording the decay of the sinusoid signal emitted from the selected atom, as it proceeds from a high energy state back to the ground state[110]. The resulting free induction decay (FID) features an exponential decay sinusoid where the signal becomes weaker and broader[110]. The signal is then decomposed from a function of time into the frequencies by performing a Fourier transform. During acquisition it is common practice to truncate the FID in order to save time when performing the pulse sequence, and to reduce the amount of computational time required for the Fourier transform[110]. The algorithmic process is then repeated multiple times to obtain multiple traces to obtain the most accurate spectra[110] (Figure 1.19).

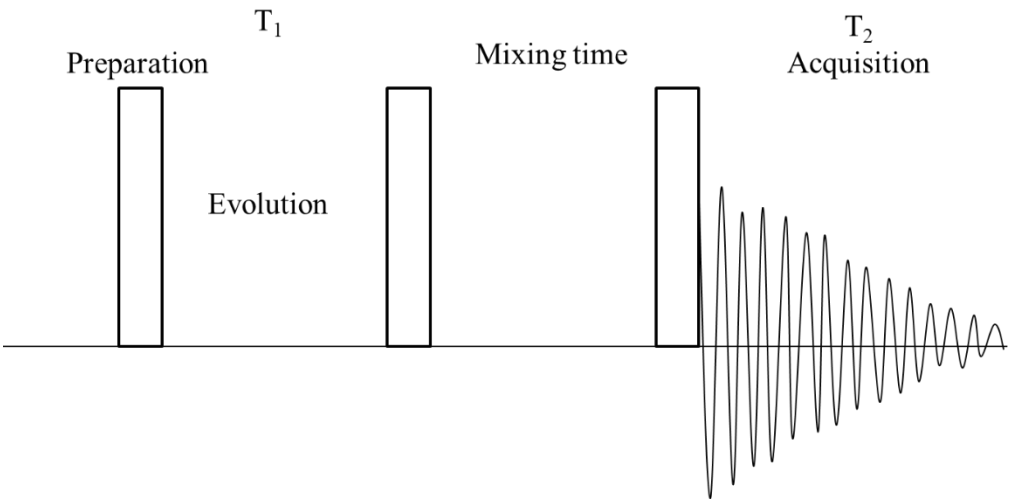

Figure 1.19. Cartoon representation of a 2D NMR pulse sequence. The rectangular bars represent individual pulses that are applied.

Some types of commonly used 2D NMR techniques include homonuclear correlation spectroscopy (COSY), nuclear Overhauser effect spectroscopy (NOESY), and diffusion ordered spectroscopy (DOSY). COSY was proposed by Jean Jeener in 1971, and first performed by Aue and colleagues in 1976[112]. COSY is a homonuclear technique used to determine the origin of signals from neighboring protons that are J-coupled to each other[113]. J-coupling or scalar coupling refers to an indirect interaction between two spin-active nuclei that are connected up to three bonds away (^{3}J), e.g. H-C-C-H, is a frequency difference measured in Hz, leading to splitting of resonance lines in NMR spectra[114]. COSY cross peaks arise as a result of magnetization transfer, which refers to the transfer of nuclear spin polarization from one spin to another that are coupled to each other[115]. Magnetization transfer occurs between similar nuclei through bonds or through space, depending on how the experiment is performed[115,116]. Using magnetization transfer, 2D spectra are created by measuring the chemical shift of the first and second nucleus before and after magnetization transfer occurs respectively[117]. There are many

different variations of COSY, COSY-90 being the most commonly used (Figure 1.20). The COSY-90 pulse sequence consists of a 90º RF pulse that tips the nuclear spin magnetization vector (M) into the XY plane[117]. M is allowed to precess in the XY plane for a given time during the evolution time period, and then irradiated with a second 90º RF pulse that tips the Y component into the Z-axis, while leaving the X component unaffected[117]. The mixing time is restricted to the duration of the second pulse. The nuclei then relax through J-coupling relaxation down to the ground state. The FID is acquired during T_2, which remains constant, and the process is repeated until the desired number of scans has been completed.

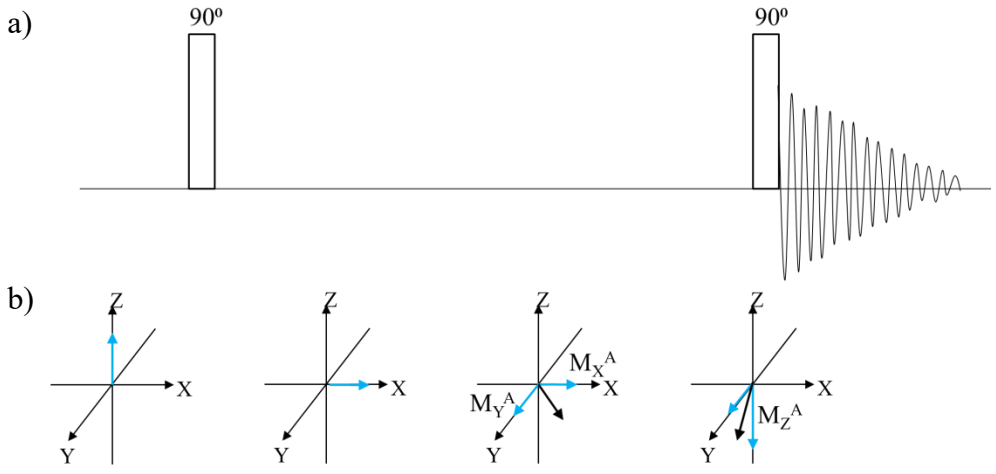

Figure 1.20. a) Cartoon representation of the COSY-90 pulse sequence, and b) cartoon representation of the change in the magnetic field vector (blue) during each stage of the COSY-90 pulse sequence, the black arrow represents an average of the magnetic field vector components. Figure a) adapted from Sanders, J. K. M. *Modern NMR Spectroscopy: A Guide for Chemists*. Oxford University Press, 1993. b) adapted from Claridge, T. *High-Resolution NMR Techniques in Organic Chemistry*. Elsevier, 1999.

NOESY in comparison to COSY is a spectroscopy technique that uses nuclear dipole-dipole interactions (NDDI) or dipolar coupling compared to J-coupling. In other words NOESY is a through-space correlation between spin-active nuclei up to 4-5 Å away, rather than a through-bond correlation like COSY[104]. The NOESY pulse sequence is similar to the COSY pulse sequence, except the NOESY pulse sequence consists of three 90º RF pulses rather than two pulses (Figure 1.21). The first 90º RF pulses tips the M of two nuclei (M_A, M_B) into the XY plane, where M_A and M_B are allowed to freely precess. A second pulse irradiates M_A and M_B tipping the Y component into the Z axis. The resultant signal is then recorded as the first time variable, t_1. M_A and M_B are allowed to precess a second time, a 90^o RF pulse is used to flip M back into the XY plane. The signal is then recorded as a function of the second time variable, t_2[110]. The time variables T_1 and T_2 are collected out of phase from each other; this is known as quadrature detection[110,118]. The nuclei then relax down to the ground state through dipole-dipole interactions and the FID is acquired. The process is repeated for the desired number of scans.

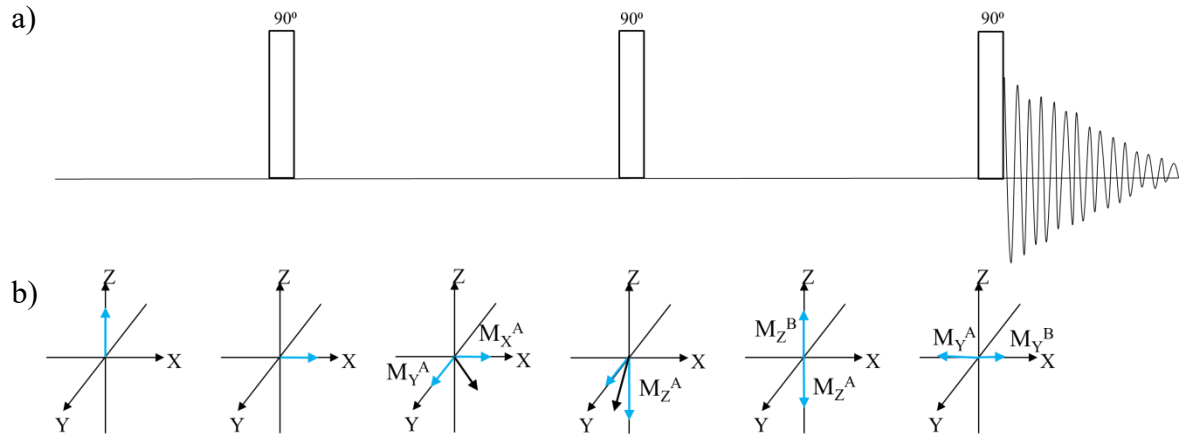

Figure 1.21. a). Cartoon representation of the NOESY pulse sequence, and b) cartoon representation of the change in the magnetic field vectors M_A and M_B (blue) during each stage of the NOESY pulse sequence. Figure a) adapted from Sanders, J. K. M. *Modern NMR Spectroscopy: A Guide for Chemists*. Oxford University Press, 1993. b) adapted from Hore, P. J. *Nuclear Magnetic Resonance*. Oxford University Press, 2015.

The distance between NDDI may affect the signal strength, as distance is a function of the intensity of a signal. The distance of a proton-proton pair is related by Equation [9][119]:

$$r_{ij} = \sqrt[6]{\frac{I_{ref}}{I_{ij}}} \quad [9]$$

where r_{ij} represents the distance between the two proton pairs, $I_{ref,}$ represents the intensity of the signal for the reference proton, and I_{ij} represents the intensity of the signal for the second proton in the proton-proton pair[119].

Using NOE and torsion angle constraints from NMR data it is possible to determine the structure and/or conformation for an analyte such as a protein or small molecule. The tools used

for structure determination and verification vary depending on the researcher and available data, however the method employed is similar. As an example, previously in this lab the conformation of 2'-deoxy-2'-fluoroguanosine was investigated[120]. H-NMR spectroscopy and NOE NMR spectroscopy was performed to obtain dihedral angles through $^{3}J_{H-H}$ coupling constants and distance constraints through NOE, respectively[120]. The distance between H5' and H5" was used as a reference and possessed a distance of 1.76 Angstrom (Å)[120]. Once the values of the dihedral angles and interatomic distances were calculated, plausible conformations were generated using distance geometry (DGEOM)[120]. DGEOM is a computer program that converts an input set of interatomic distance constraints (complete or sparse) into three-dimensional atomic coordinates for molecular conformations consistent with the input constraints. It was found that the generated conformations were in agreement with the calculated dihedral angles and NOE constraints obtained[120].

DOSY in comparison to COSY and NOESY is used to differentiate NMR signals from a mixture of compounds based on diffusion coefficients for individual resonances, which is plotted against the F2 axis. This makes DOSY a particularly useful technique when physical separation is impossible or impractical. Diffusion occurs through Brownian motion, the random motion of particles driven by thermal energy when they are suspended in a solution[117]. Brownian motion depends on many physical parameters such as the size, shape of the molecules, temperature and viscosity of solution[116,121]. To quantify the ability of a molecule to undergo translational diffusion the diffusion coefficient, D, can be used, and can be described by the Stokes-Einstein equation, Equation [10][122];

$$D = \frac{kT}{6\pi\eta r_s} \quad [10]$$

where D represents the diffusion coefficient in m^2s^{-1}, k represents the Boltzmann constant, T represents the temperature, η represents the viscosity of the liquid, and r_s represents the hydrodynamic radius of the molecule[122].

The DOSY pulse sequence is similar to a spin echo sequence, but with the addition of a magnetic field gradient pulse[123] (Figure 1.22). First a 90° RF pulse is used to tip M into the transverse plane[124]. A magnetic field gradient pulse is applied which dephases M, spatially labels molecules based on their relative position in the NMR tube and causes some molecules to diffuse[125,126]. An 180° RF pulse is applied which inverts the dispersed M[124]. After a short period M is negative of what it was during the preparation period. A second magnetic field gradient pulse is applied to refocus the signal[126]. The difference in time between the first and second magnetic field gradient pulse is called the diffusion time or delay, Δ [126].

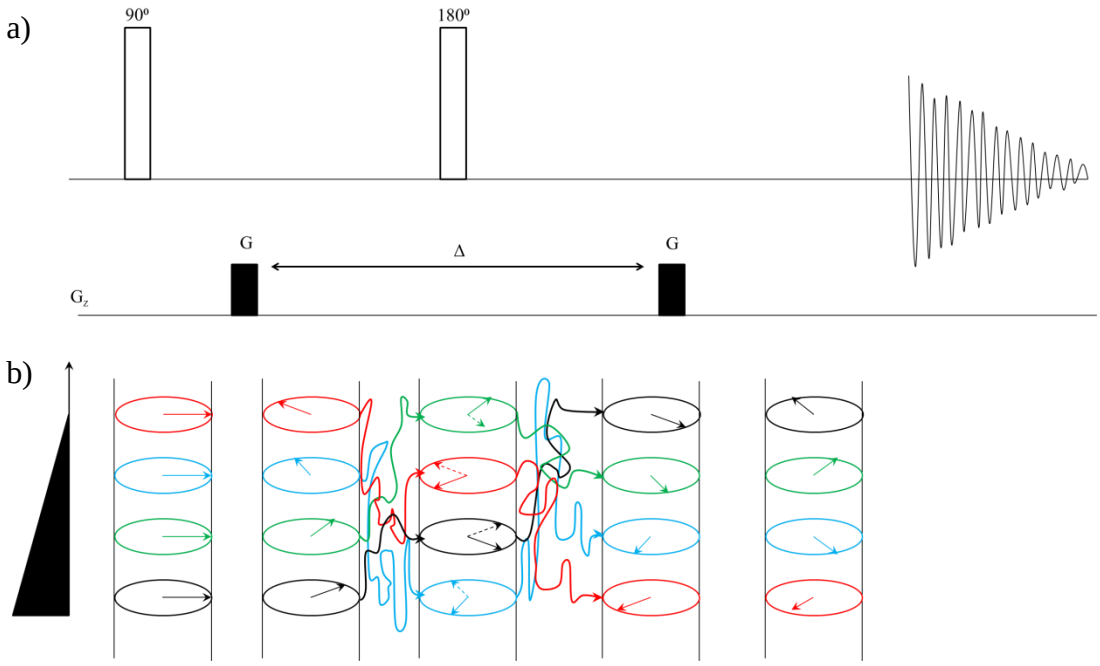

Figure 1.22. Cartoon representation of the DOSY a) pulse sequence and b) diffusion gradient. Figure a) adapted from Pregosin, P. S. *NMR in Organometallic Chemistry*. John Wiley & Sons, 2013.

Movement of molecules during Δ leads to a loss of resonance intensity. If there is no movement of the molecule during Δ, then the signal is completely recovered. On the other hand, if movement occurs during Δ, then the signal is not rephrased. The diffusion coefficient can be determined by the relationship between the initial and final intensity of the signal, and can be expressed by Equation [11][127]:

$$I = I_0 e^{-D\gamma^2 g^2 \delta^2 \left(\Delta - \frac{\delta}{3} - \frac{\tau}{2}\right)} \quad [11]$$

where I represents the observed intensity, I_0 represents the reference intensity, D represents the diffusion coefficient, γ represents the gyromagnetic ratio of the observed nucleus, g represents the gradient strength, δ represents the length of the gradient, and Δ represents the diffusion time, and τ represents the delay between gradients[127].

1.5.5 High performance liquid chromatography (HPLC)

High-pressure liquid chromatography or high-performance liquid chromatography (HPLC) is an analytical technique that is used to examine the purity of an analyte[128]. In HPLC a column is filled with an adsorbent material such as silica that makes up the stationary phase[128]. The sample is introduced to the column through the sample injector and eluted using the mobile phase, being a solvent or mixture of solvents under pressure[128]. Separation of an analyte is based on differences in the partition coefficient of the analyte between the mobile phase and the stationary phase[128]. An analyte that binds to the stationery phase with lower affinity will be eluted out more quickly[128]. Elution of the analyte can be controlled by changing the composition of the mobile phase[128]. If the composition of the mobile phase is constant throughout the procedure, then the separation is described as isocratic elution[128]. On the other hand, if the composition of the mobile phase changes during the procedure, then the separation is described as gradient elution[128]. The retention time is the amount of time that it takes an analyte to travel through the column is known as the retention time[128]. Once the analyte is eluted off the column, it is recorded by a detector[128]. Different types of detectors can be used depending on the nature of the analyte. As an example, UV-Vis detectors are commonly used if the analyte is UV-Vis active. If an analyte is not UV-Vis active then other types of detectors, such as mass spectrometry, IR, fluorescence, and optical rotation can be used[128]. After the analyte is detected

the data are processed using a computer to generate a chromatogram, a graph that shows detected signals over time[128]. To identify the analyte, known standards can be examined under the same HPLC conditions and the retention times can be compared to the peaks in the chromatogram of the mixture. If the standard and analyte in the mixture possess the same retention time, then it is likely that the standard and analyte are the same molecule. In addition to the identity of the analyte, the concentration of the analyte in the mixture can be determined by comparing the area under the peak of the analyte in the chromatogram to the area under the peak of the standard[128].

1.5.6 Differential Scanning Calorimetry

Differential scanning calorimetry (DSC) was developed in 1962-1964 by Watson and O'Neil, and Privalov and Monaselidze[129–132]. DSC is a thermoanalytical technique that measures the amount of heat required for the thermal denaturation to occur. DSC has been used to examine a wide variety of polymers and macromolecules such as polyparaphenylene terephthalamide (Kevlar)[133], DNA[134], and proteins[135]. Thermal denaturation can be performed by the use of dry bath, water bath, microwave[136], and laser[137]. However, DSC allows for the analysis of a sample's thermal melt temperature, T_m, heat capacity (C_p), and the change in enthalpy of the system[138]. T_m is the temperature at which 50% of the molecule being are examined is denatured[139]. The higher the T_m, the more thermally stable the molecule is. C_p, on the other hand, is a measurement of a material's ability to absorb heat. More specifically, C_p is a ratio of the heat flow $\left(\frac{\delta H}{\delta t}\right)$ and the heating rate $\left(\frac{\delta T}{\delta t}\right)$, and can be described by Equation [12][140]:

$$C_p = \frac{dQ}{dT} = \left(\frac{\delta H}{\delta T}\right)_P \quad [12]$$

where C_p represents the heat capacity of a sample at constant pressure measured in J/K, dQ represents the differential amount of heat required measured in J, dT represents the differential temperature, δH represents the differential amount of enthalpy measured in $\left(\frac{J}{mole}\right)$.

DSC works by directly measuring the difference in the amount of heat absorbed by the sample and reference cell. There are two types of DSC, heat-flux and power differential or power compensation[141]. In the heat-flux system, the sample and reference cells are heated with the same amount of energy, supplied by a power source[141]. The temperature of each cell is measured by a set of thermocouples. The difference in temperature correlates with the C_p of the sample compared to the reference[142]. The second type of DSC technique, power differential works by heating the sample and reference cells with a separate heat source to a specific temperature[141]. The difference in energy required to maintain the temperature is measured[141]. For each type of DSC, the output is recorded as a plot of heat flux (rate) versus temperature, known as a thermogram (Figure 1.23). The indication of an analyte being present in a mixture is displayed as a peak or multiple peaks on the thermogram, which can be used to describe the thermal transitions of the analyte examined. When heat flow is plotted against temperature, a positive peak represents an exothermic process, while a negative peak represents an endothermic process[143]. As an example, thermal denaturation or unfolding of a protein is an endothermic process, meaning the peak on the thermogram will be negative[144]. In addition to T_m, the stability of a macromolecule can be described by the difference in the Gibbs free energy of the folded and unfolded states[145]. Gibbs free energy describes the amount of energy that is available to do work. Processes are described as being spontaneous or non-spontaneous, which relates to the enthalpy,

ΔH, and entropy, ΔS . If a reaction is spontaneous than ΔG is negative, and the formation of the products is favoured. If a reaction is non-spontaneous than ΔG is positive, and the formation of the reactants is favoured. As a result energy in the form of work is required to drive the process to completion[146]. To calculate the difference in Gibbs free energy the following equation is used, Equation [13][146]:

$$\Delta G = \Delta H - T\Delta S \qquad [13]$$

where ΔG represents the change in Gibbs free energy measured in joules/mole $\left(\frac{J}{moles}\right)$ or calories/mole $\left(\frac{cal}{moles}\right)$, ΔH represents the change in enthalpy measured in $\left(\frac{J}{moles}\right)$, T represents the temperature of the system in Kelvin (K), and ΔS represents the change in entropy measured in units joules/Kelvin $\left(\frac{J}{K \bullet moles}\right)$[146].

The difference in Gibbs free energy as described by Equation [13] is the difference between enthalpy, and entropy. ΔH describes the total heat content of a system, that is, the sum of the total internal energy and the work that is required to drive the process to completion[145]. ΔH is dependent on the concentration of the sample examined, and can be determined by calculating the area under the transition peak of the thermogram[147] (Figure 1.23). For this reason, ΔH is also known as the calorimetric enthalpy, ΔH_{cal}. ΔS on the other hand, describe how energy is distributed in a system[148]. As an example, the entropy of a system increases when the amount of motion within the system increases.

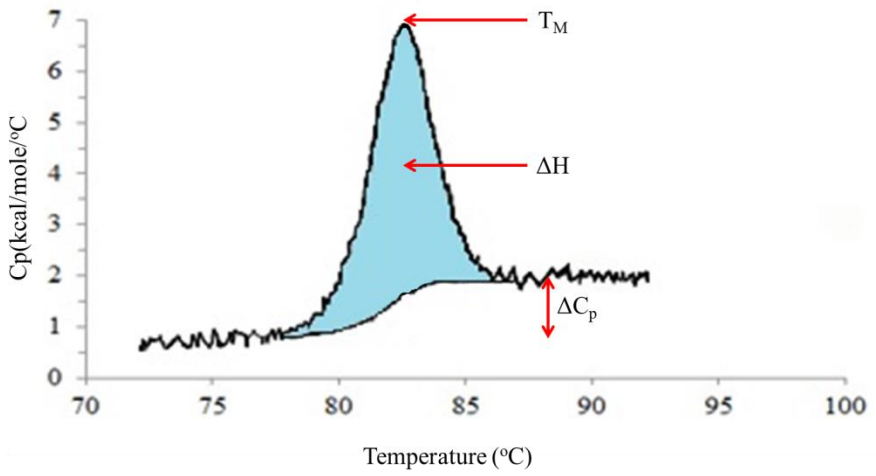

Figure 1.23. Cartoon representation of a DSC thermogram depicting the heat capacity in units kcal/mole/ºC versus the temperature in ºC the thermal melt temperature, T_m, change in enthalpy, $\mathbf{\Delta H}$, and change in heat capacity, $\boldsymbol{\Delta C_p}$.

To describe the transitions that occur during a thermal melting process, the output can be fitted to either a two-state or a non-two-state model. A two-state model is defined by a system possessing two conformational states being either native or unfolded state[149]. A non-two-state model on the other hand, is defined by a system consisting of multiple transition states[150]. In comparison to the non-two-state model, the two-state model simplifies the system making the model unsuitable to analyze DSC thermograms, as multiple conformations are required to describe the unfolding dynamics of a protein. Additionally, unlike the two-state model, the non-two-state model possesses an extra parameter called the van't Hoff enthalpy, ΔHvH, an independent estimate of the enthalpy of the transition[151]. ΔHvH is determined by the shape of the transition peak (ΔC_p^{max} at transition midpoint), where the sharper the transition the larger the value of ΔHvH [152]. ΔHvH describes the cooperativity of the system, a measurement of heat change per unfolding unit or cooperative unit[153,154]. As an example, in DNA the cooperative unit

would be the formation of hydrogen bonds between two complementary base pairs. ΔHvH can be determined by using other techniques that allow for the thermal analysis of an analyte, such as CD spectroscopy[155]. To calculate the ΔHvH the fraction of folded and unfolded macromolecule at different temperatures needs to be known, which can be determined experimentally. By determining the amount of folded and unfolded macromolecule, the equilibrium constant, K_{eq}, can be determined, which is the ratio of the concentration of unfolded versus folded macromolecule. In addition to enthalpy and entropy, the Gibbs free energy is related to the equilibrium constant by Equation [14][156];

$$\Delta G = -RTlnK_{eq} \quad [14]$$

where R represents the universal gas constant, and T represents the temperature of the system[156]. Using Equation [13] and [14], a thermodynamic relation describing the relationship between Gibbs free energy and the equilibrium constant can be derived, known as the van't Hoff equation, Equation[15][157]:

$$lnK_{eq} = \frac{\Delta H}{RT} + \frac{\Delta S}{R} \quad [15]$$

Unlike ΔH_{cal}, ΔHvH is independent of the concentration of the sample examined. However, to understand the dynamics of the system, it is common practice to examine the ratio of $\frac{\Delta H_{cal}}{\Delta HvH}$. If the ratio of $\frac{\Delta H_{cal}}{\Delta HvH}$ is equivalent to two, then this suggests that the macromolecule consists of two or more identical domains that unfold independently with T_m and ΔH,

representing a non-two-state unfolding mechanism[152]. If $\frac{\Delta H_{cal}}{\Delta \mathrm{HvH}}$ is equivalent to one, then this suggests that the macromolecule consists of a single domain, representing a two-state unfolding mechanism[152]. It is also possible for $\frac{\Delta H_{cal}}{\Delta \mathrm{HvH}}$ to be less than one, this would suggest that the macromolecule formed a dimer and the dimers would have undergone a single coupled transition[152].

Examination of DNA by DSC has been done before. As an example, Duguid and colleagues (1996) performed DSC on a 160 bp fragment of calf thymus DNA, and then examined the structural changes that occurred during the melting of B-DNA using Raman spectroscopy[134]. The T_m, ΔH_{cal}, and ΔHvH, were determined to be 75.5◦C, 50.4 kcal/mol, 6.7 kcal/mol per base pair respectively. Raman spectroscopic data show the range of the T_m to be 75-80°C, and the range of ΔHvH to be 43-61 kcal/mol which was consistent with the results obtained by DSC[134].

Chapter 2: Results and Discussion

2.1 Circular dichroism study of DNA conformations at near-biologically relevant concentrations

In the work described in this thesis, CD and UV-Vis spectra for $d(CG)_9$ and a non-self-complementary sequence (mixed sequence) was obtained at sub-m*M* concentrations by the use of home-made cuvettes with the capability of possessing an adjustable pathlength of down to ~ 0.1 mm. The significance of the work performed is relevant to nucleic acid concentrations in cellular cytoplasm and nucleus. In a study conducted by Sparague and colleagues (2006), the DNA concentrations in the nucleus of mice cells was calculated to be around 10 mg/ml[158], which would correspond to approximately 1.8 m*M* of double stranded $d(CG)_9$. Measurements of CD spectra of nucleic acids are usually performed at concentrations around 10 μ*M* at a 1 cm pathlength, a concentration much lower than nucleic acid concentrations in biological systems (~10 mg/ml)[158]. Attempts to study $d(CG)_9$ by CD spectroscopy at higher concentrations using 1 cm pathlength cuvettes led to CD artifacts, and the results were impossible to interpret (Figure 2.1).

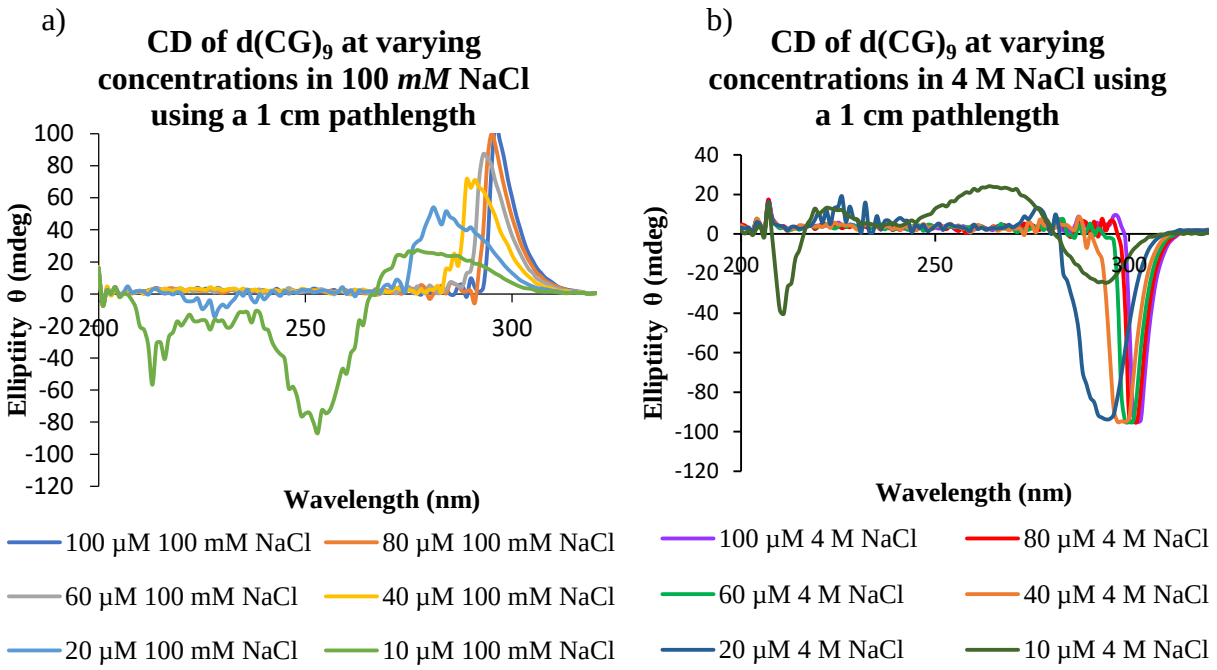

Figure 2.1. CD profiles of d(CG)$_9$ in the a) B-DNA or b) Z-DNA conformation at concentrations ranging from 100 to 10 µ*M* measured using a 1 cm cuvette.

The CD spectra of d(CG)$_9$ in the B- and Z-DNA conformation were obtained using a 1 cm pathlength cuvette with samples containing 100 m*M* or 4 *M* NaCl, respectively. The concentration of d(CG)$_9$ was decreased from 100 µ*M* to 10 µ*M* at 10 µ*M* decrements. At 100 µ*M* a sharp peak at approximately 300 nm forms in the positive or negative y-axis for B- or Z-DNA, respectively. When the concentration was decreased the peak is shifted towards short wavelength and broadens, until the point where the profiles that are characteristic of B- and Z-DNA begin to appear. At 10 µ*M* of d(CG)$_9$, CD profiles characteristic of B-DNA were recorded, with a positive peak at 270 nm, and two negative peaks at 250 nm and 215 nm. At the same d(CG)$_9$ concentration, typical Z-DNA CD patterns were seen, with a negative peak at 290 nm and a positive band at 265 nm.

These results suggested that the CD spectra measured at concentrations higher than 10 μ*M* of d(CG)$_9$ duplex in a 1 cm pathlength do not represent the conformation of the DNA specie(s) present. The peak at 300 nm is artefactual as a result of the physical limitations of the spectropolarimeter rather than an indication of a change in conformation. In the event that a highly concentrated sample is irradiated with circularly polarized light, the transmitted light is reduced and results in too few photons being able to reach the detector[125]. As a result the HT voltage increases, amplifying both the signal and noise leading to the appearance of the sharp peak at 300 nm[125]. In order to examine DNA solutions at higher concentrations such as 100 μ*M*, a cuvette with a 1 mm pathlength was used. By decreasing the pathlength of the cuvette, this would allow for more photons to reach the detector. To corroborate the CD spectra of B-DNA obtained at 100 μ*M* using a 1 mm pathlength, a CD spectrum of B-DNA at a concentration of 10 μ*M* using a 1 cm cuvette was obtained. The CD spectra were compared to each other to determine if the CD spectra are similar to one another (Figure 2.2 a). In addition to CD spectrometry, UV-Vis spectrometry was performed to determine if the sample concentration at the defined pathlength is within the dynamic range (Figure 2.2 b). For d(CG)$_9$ in the B-DNA conformation at 100 μ*M* using a pathlength of 1 cm, the UV-Vis spectrum appears cut off at approximately 5 absorbance units, suggesting that the absorbance is over the dynamic range. For the UV-Vis spectrum taken with a 1 mm pathlength, the absorbance is well within the dynamic range (Figure 2.2b).

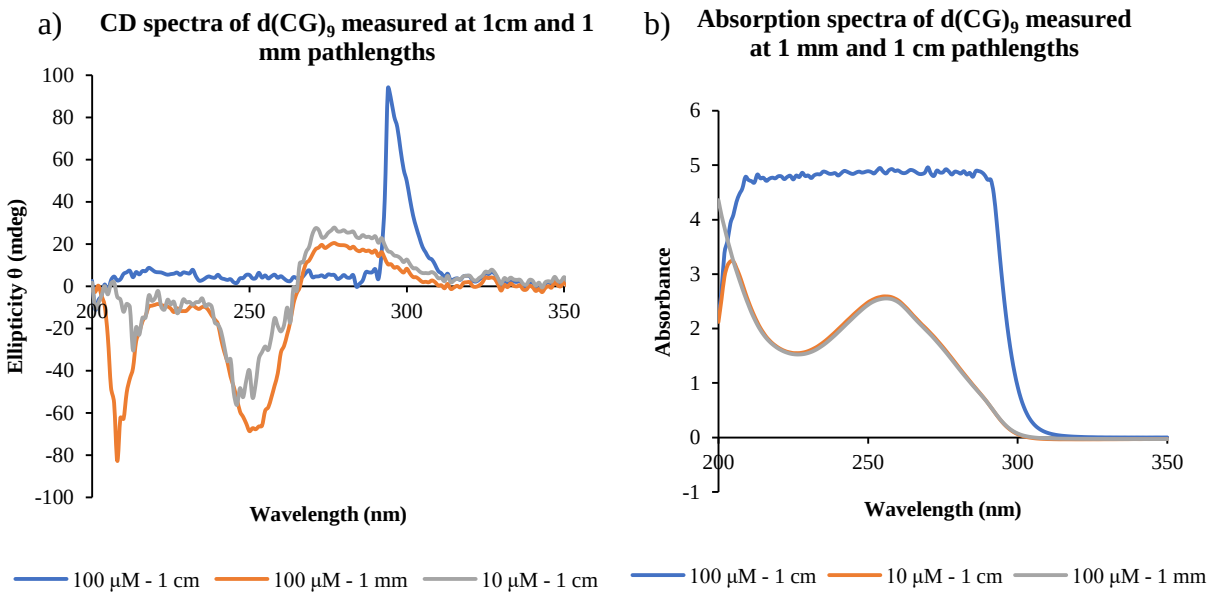

Figure 2.2. a) CD and b) UV-Vis spectra of $d(CG)_9$ in the B-DNA conformation at 10 and 100 µ*M* in 1 cm and 1 mm pathlength cuvettes.

To confirm the CD results obtained for $d(CG)_9$, CD and UV-Vis spectrometry was also performed on bovine serum albumin (BSA) using a 1 cm and 1 mm cuvette at a concentration range between 10 to 100 µ*M* (Figure 2.3).

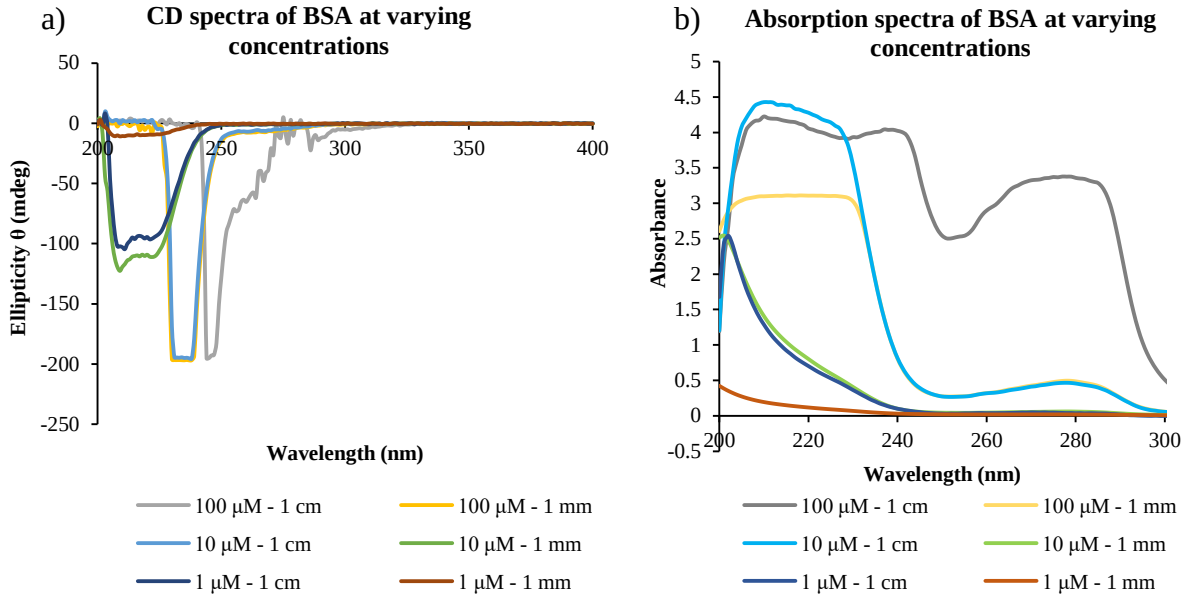

Figure 2.3. a) CD spectra and b) UV-Vis spectra of BSA from 10 µ*M* to 100 µ*M* with a 1 mm or 1 cm pathlength.

The CD and UV-Vis spectra for BSA produced similar results to that of the DNA samples, where the λ_{max} of the peak becomes blue shifted and the peak broadened, until the point where the CD profile that is characteristic of BSA begins to form.

To further confirm that the peak for $d(CG)_9$ at 300 nm in high concentration samples when using a 1 cm pathlength is an instrument artifact, camphorsulphonic acid (CSA) was used to examine the effect of sensitivity (Figure 2.4 a) and CSA concentrations on CD spectra (Figure 2.4 b). CSA was selected as a standard to test the effects of sensitivity and concentrations because CSA is a strongly optically active compound that is available in both R and S or (-) and (+) forms respectively. The sensitivity of the CD spectropolarimeter is the point where the HT voltage is enabled[159]. By increasing the HT, or decreasing the sensitivity, this would allow more photons to reach the detector and result in a better signal/noise ratio[159]. It should be noted that the amount of energy of a photon is directly proportional to the frequency. To accommodate for the

fluctuations in energy, the gain on PMT detector adjusts the amplitude of the signal depending on the DC voltage output[159]. As such, measuring a highly concentrated sample with high sensitivity would result in artifact in the CD spectra similar to what was seen for $d(CG)_9$ at 100 μ*M* using a 1 cm pathlength (Figure 2.2 a).

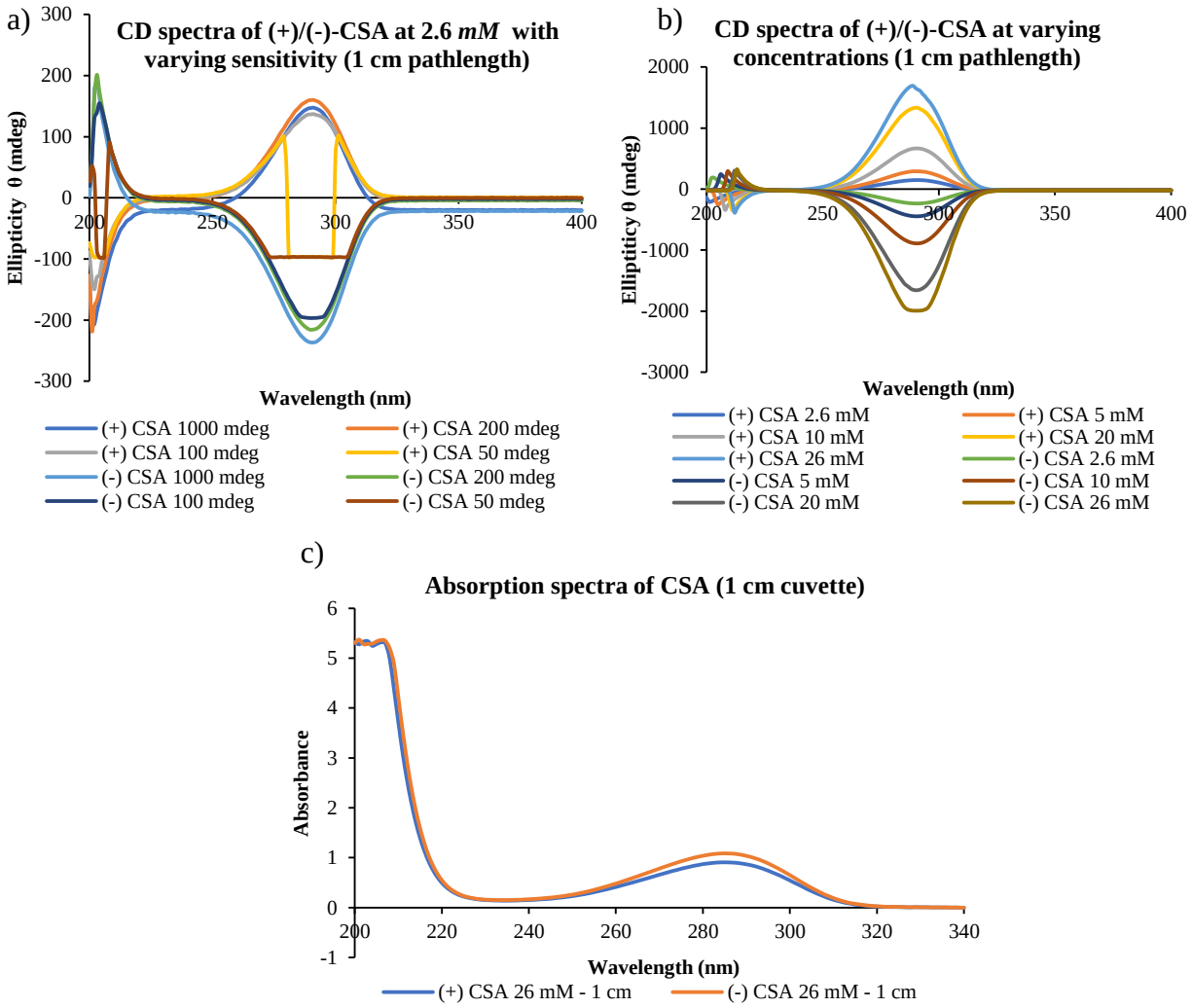

Figure 2.4. a) CD spectra of (+)/(-)-CSA where the concentration and bandwidth were kept constant (2.6 m*M*, 1 nm), and the sensitivity was decreased from a range of 50 mdeg to 1000 mdeg, b) CD spectra of (+)/(-)-CSA where the sensitivity was reduced to 1000 mdeg, the bandwidth was set to 1 nm, and a series of concentrations ranging from 2.6 to 26 m*M* were examined, and c) UV-Vis spectra of (+)/(-) –CSA at 2.6 m*M* measured using a 1 cm pathlength.

The CD spectrum for 2.6 m*M* (+)-CSA at a sensitivity of 50 mdeg shows two distinct sharp peaks at 300 and 280 nm, while the CD spectrum for 2.6 m*M* (-)-CSA at a sensitivity of 50 mdeg shows a plateau between 300 and 280 nm. Additionally the CD spectrum for 2.6 m*M* (+)/(-)-CSA at a sensitivity of 100 mdeg possesses flattened peaks at 290 nm. CSA absorbs maximally at 290 nm and possesses a $\varepsilon_L - \varepsilon_R$ of 2.36 cm^{-1} $mmol^{-1}$ [160] (reported by Chen and Yang as 2.36 cm^2 $mmol^{-1}$). Based on Equations [6] and [7], this difference in absorbance of L-CPL and R-CPL would give rise to a maximum ellipticity of 200 mdeg. As such, the detector would be at the maximum voltage at 50 mdeg sensitivity, and the spectra would be off scale. When increasing the concentration of (+)/(-)-CSA to 26 m*M* the UV-Vis spectrum shows an absorbance that is slightly below 2 absorbance units, which is in the dynamic range. When the sensitivity of the CD spectropolarimeter was reduced to 1000 mdeg and the CSA concentration was increased from 2.6 to 26 m*M*, the CD spectra were similar in appearance, but the absorption spectrum of the 26 m*M* sample was flattened.

In addition to adjusting the sensitivity and pathlength, the spectral bandwidth can also be manipulated (Figure 2.5 a/b). Thus, increasing the bandwidth would allow for more light to irradiate the sample, at the expense of decreasing the resolution of the spectral bands[159]. Decreasing the bandwidth, on the other hand, improves the resolution of the spectral bands, while decreasing the signal to noise ratio[159,161]. For CSA samples at 2.6 m*M* and 10 m*M* concentrations, however, altering the bandwidth did not give a noticeable difference in the CD spectra.

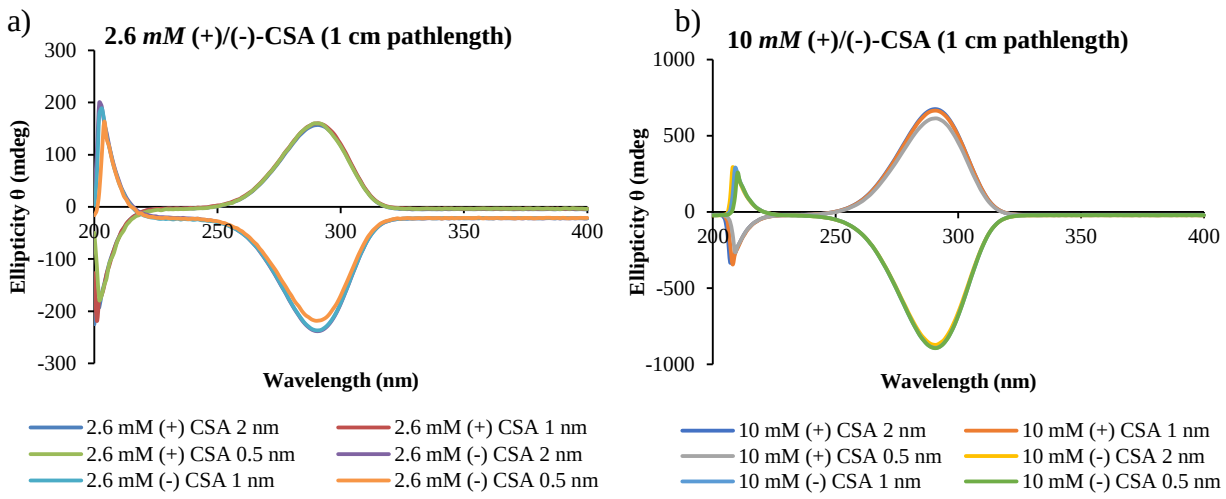

Figure 2.5. a) 2.6 mM and b) 10 mM CD spectra of (+)/(-)-CSA where the bandwidth was varied from 0.5 to 2 nm at different sample concentrations.

2.1.1 Home-made variable pathlength cuvette

Although cuvettes with a short pathlength do exist and are commercially available, the amount of material required is usually quite large, thus making measurement extremely costly. As an example, the Starna cylindrical cell requires 2.6 mL of material. For a 1 m*M* sample of $d(CG)_9$ this would cost approximately $1300 CAD (based on the pricing provided by IDT DNA). For this reason a home-built device called a FlexiCell was used for CD measurement of samples at high μ*M* to low m*M* concentrations. The advantage of the FlexiCell is that a sample volume as little as 10 μL is sufficient to obtain a CD profile at a pathlength of 0.1 mm. To determine the minimum pathlength of the FlexiCell, the FlexiCell had to be calibrated. Thymidine was used to calibrate the FlexiCell, because thymidine is readily available, and the molar extinction coefficient ε is known for the λ_{max} at 267 nm (9650 cm^{-1}/M)[162] and 235 nm (2250 cm^{-1}/M)[162]. Thus, thymidine solutions in water at 0.5, 1, 5 and 20 m*M* were examined using the FlexiCell at

various pathlengths (Figure 2.6 a/b). To describe the relationship between absorbance and the minimum pathlength allowed by the FlexiCell, a modified Beer Lampert law can be used;

$$A = (l_{min} + t\alpha)c\varepsilon \quad [16]$$

where A represents the absorbance, l_{min} represents the minimum pathlength of the FlexiCell, t represents the number of ticks, and α represents the minimum distance per tick;

$$\alpha = \frac{1\ turn}{50\ ticks} \cdot \frac{0.05\ cm}{1\ turn} = \frac{0.001\ cm}{tick} \quad [17]$$

using the relationship, $\frac{A}{C\varepsilon} = l_{min} + t\alpha$ a linear plot was constructed where the average value of $\frac{A}{C\varepsilon}$ for each concentration at 267 nm and 235 nm as a function of the number of ticks per turn was plotted (Figure 2.6 c). The data were fitted to a linear equation using least squares regression, where the $l_{min}$was found to be the y-intercept in the linear plot, and the error of the pathlength was found using the standard error of the linear regression. In this manner, the minimum pathlength of the FlexiCell was found to be 0.129 ± 0.015 mm when the barrel assemblage is completely closed.

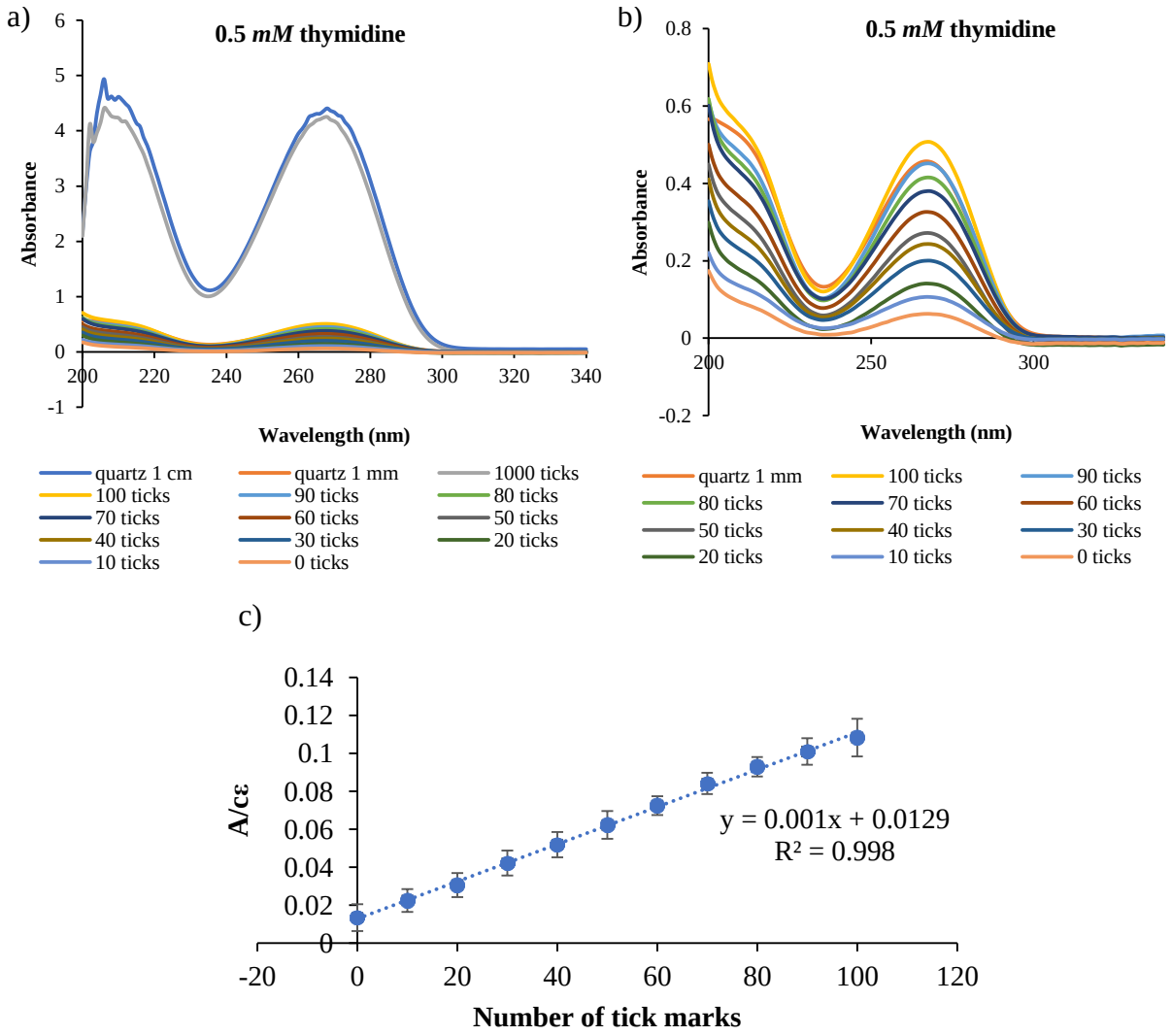

Figure 2.6. a) UV-Vis spectra for 0.5 m*M* thymidine obtained using a 1 cm quartz cuvette and the FlexiCell set to 1000 tick marks. b) UV-Vis spectra of 0.5 m*M* thymidine obtained using a 1 mm quartz cuvette, and the FlexiCell ranging from 100-0 tick marks. c) Plot of $\frac{\mathbf{A}}{\mathbf{C\varepsilon}}$ versus number of tick marks. UV-Vis data for 1 m*M*, 5 m*M*, and 20 m*M* were obtained, but are not shown.

Using the FlexiCell, the CD spectra for a mixed sequence DNA duplex (5'-CTTTAAGAAGGAGATATACCA-3') and $d(CG)_9$ duplex at a concentration between 1 m*M* and 5m*M* were obtained (Figure 2.7). At 5 m*M*, the CD profile of the mixed sequence resembles that of $d(CG)_9$ at 100 μ*M* using a 1 cm pathlength, with a sharp peak at approximately 300 nm.

Similarly, the UV-Vis spectrum of this sample is cut off at an absorbance of 6 absorbance units. The peak at 300 nm becomes blue shifted as the concentration decreases. At 2 m*M* and 1.7 m*M* the CD profile shows some resemblance of a B-DNA spectrum, where the peak at 270 nm becomes broader, with the emergence of a peak at 240 nm. However, between 240 and 270 nm the CD profile is flattened, likely because of saturation of absorption. At 1.5 and 1 m*M* the CD profile becomes reminiscent of that obtained at 10 μ*M* using a 1 cm pathlength. When $d(CG)_9$ in the B- and Z-DNA conformation was examined, the CD profiles were similar to the mixed sequence samples. These results suggest that 5 m*M* and 2 m*M* concentrations are over the dynamic range, while at 1 m*M* the CD profile was within the dynamic range.

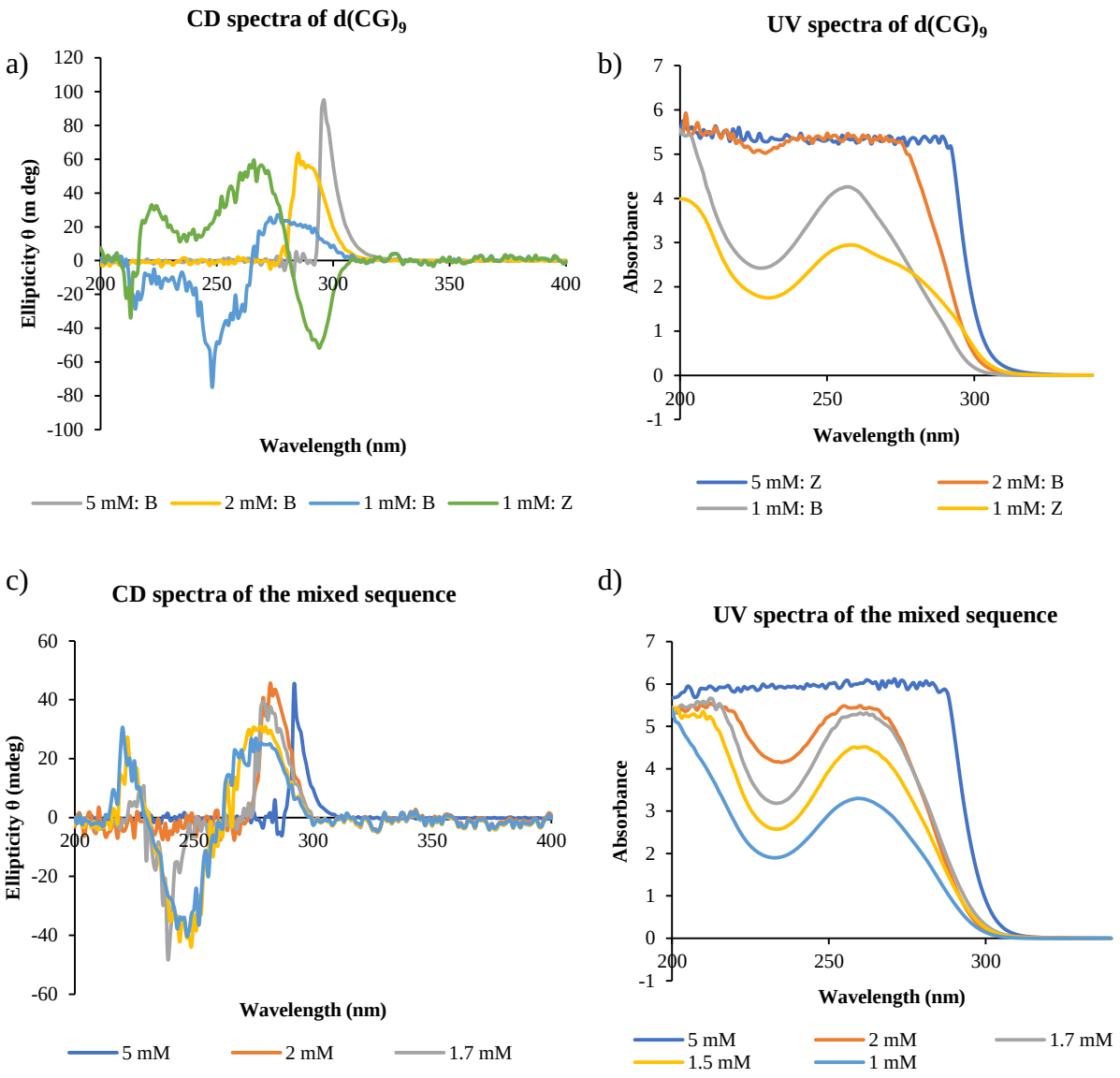

Figure 2.7. CD and UV-Vis spectra of $d(CG)_9$ and the mixed sequence measured using the FlexiCell at 0 tick marks a) CD spectra of $d(CG)_9$, b) UV-Vis spectra of $d(CG)_9$, c) CD spectra of the mixed sequence, and d) UV-Vis spectra of the mixed sequence.

2.1.2 Future works:

While the use of FlexiCell allowed for the CD measurement of DNA samples up to *ca*. 1 m*M*, an ability to study the conformation of DNA by CD spectroscopy at higher concentrations would be desirable, as it will be relevant for DNA in the nucleus. Toward this goal, a more powerful light source could be required to obtain a CD spectrum. A request to access beamlines at the Soleil synchrotron in Essonne, France has been granted for the purpose of examining DNA duplexes at a concentration of 10 m*M* by synchrotron radiation circular dichroism (SRCD) spectroscopy. Experiments using the Solei synchrotron will be carried out in due course.

2.2 Folding kinetics of $d(CG)_9$

In this thesis, the effects of reconstitution conditions on the conformation of a self-complementary oligonucleotide $d(CG)_9$ were investigated. $d(CG)_9$ was selected as an oligonucleotide of interest because it is capable of forming duplexes and hairpins. Using diffusion ordered spectroscopy (DOSY) and HPLC, it was concluded that the secondary structure adopted by $d(CG)_9$ was dictated by the condition under which the sample was reconstituted, especially the salt concentration.

2.2.1 Reconstitution

Stability of the secondary structure of an oligonucleotide is dependent on the composition of the nucleobase sequence, base-stacking, and base-pairing interactions[163]. It is expected that ssDNA would interact strongly with the surrounding water molecules because of the combination of the polar and charged groups that make up ssDNA[163]. However, by changing the solvent used in reconstitution this would affect one or more of these interactions. In this study, commercial, lyophilized $d(CG)_9$ was reconstituted in either water or Tris-HCl buffer (10 m*M*, pH

7.5) containing 100 m*M* NaCl, and the conformations were analyzed by DOSY NMR spectroscopy and anion exchange (AEX) HPLC under native conditions (Figure 2.8).

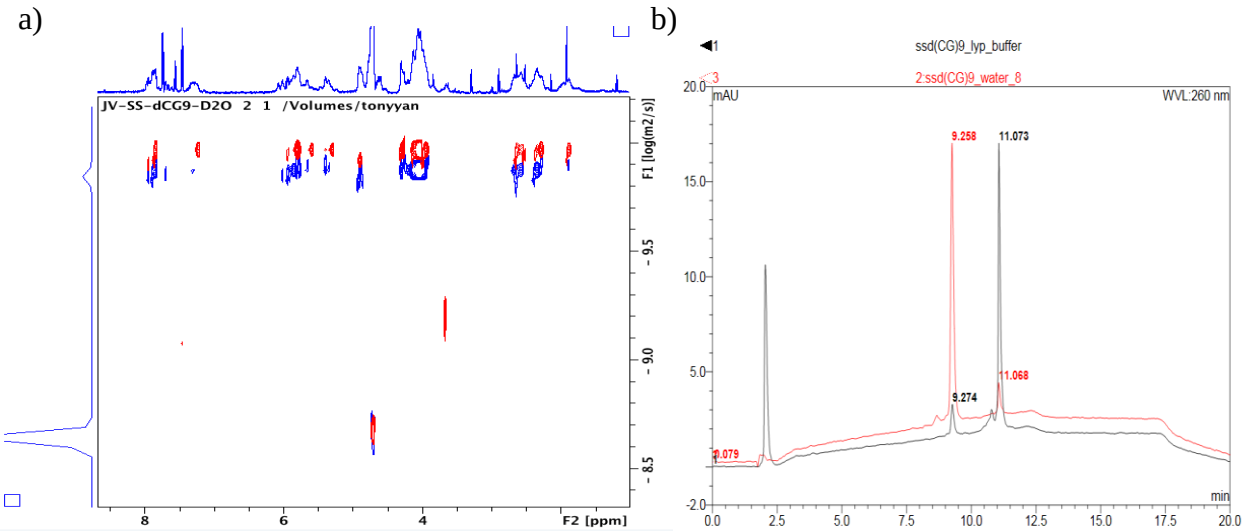

Figure 2.8. a) DOSY NMR spectra of $d(CG)_9$ reconstituted in either D_2O (blue) or Tris-HCl buffer (10 m*M*, pH 7.5) containing 100 m*M* NaCl (red). The DOSY spectra were compared to each other by overlaying the signal from HOD residue at 4.71 ppm. b) AEX HPLC chromatogram of $d(CG)_9$ reconstituted in either water (red) or Tris-HCl buffer (10 m*M*, pH 7.5) containing 100 m*M* NaCl (black).

Examination of the DOSY NMR spectra and HPLC profiles suggests the formation of two different conformations when $d(CG)_9$ was reconstituted in either water or Tris-HCl buffer (10 m*M*, pH 7.5) containing 100 m*M* NaCl. To confirm the secondary structures adopted by $d(CG)_9$, two 18 base pair DNA sequences that can form either a hairpin conformation (hairpin sequence, 5'-d(CCCAATTTTTTTTTGGG)-3'), or B-DNA duplex (B-DNA sequence, mer 1: 5'-d(CTTTAAGAAGGAGATATA)-3' and mer 2: 5-d(TATATCTCCTTCTTAAAG)-3') were

analyzed by AEX HPLC and compared to the chromatograms obtained for the two different $d(CG)_9$ conformations (Figure 2.9).

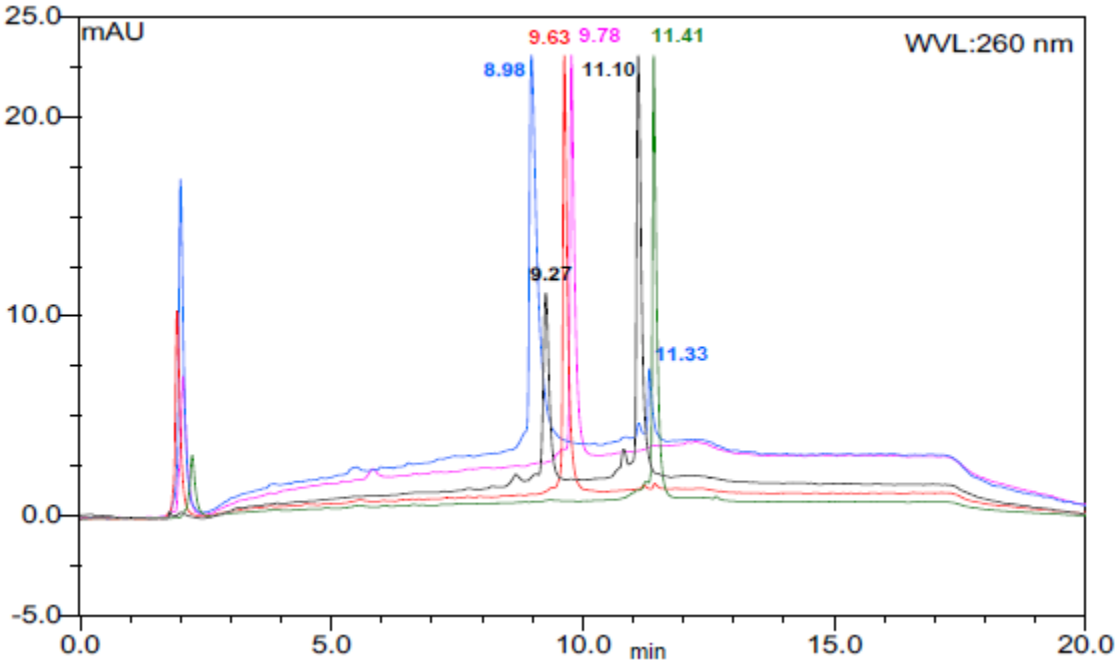

Figure 2.9. AEX HPLC chromatogram comparing the retention times for hairpin (pink, 9.78 min), B-DNA duplex (green, 11.41 min), ssDNA mer1 (blue, 8.98 min), ssDNA mer2 (red, 9.63 min), and $d(CG)_9$ in the hairpin conformation (black, 9.27 min) and B-DNA duplex conformation (black, 11.10 min). The DNAPac200 column was eluted under non-denaturing conditions. The column was eluted with a linear gradient of 10-55% 1*M* NaCl over 10 minutes, 10% 250 *mM* Tris-HCl buffer (pH 8.5).

As can be seen in the chromatograms in Figure 2.9, the retention time of the hairpin conformation of $d(CG)_9$ reconstituted in 100 m*M* NaCl buffer (9.27 min) is very close to that of $d(CG)_9$ reconstituted in water (9.26 min, data not shown), and that of the 18 base pair DNA sequences that forms a hairpin (9.78 min). The retention time of $d(CG)_9$ in the duplex

conformation (11.10 min) is close to that of the 18 base pair DNA sequence that forms a B-DNA duplex (11.41min).

To determine if the hairpin and duplex conformations of $d(CG)_9$ are dynamic, the $d(CG)_9$ samples reconstituted in water or Tris-HCl buffer containing NaCl were diluted with Tris-HCl buffer containing NaCl, or water respectively, and the portions of the hairpin and double strand structures were determined by AEX HPLC.

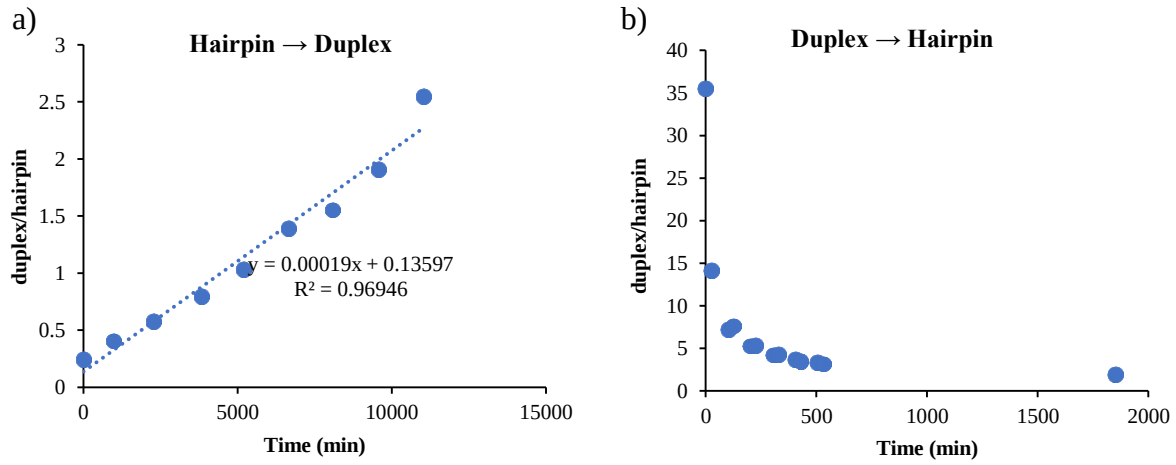

Figure 2.10. Plot of the ratio of $\frac{\textbf{duplex}}{\textbf{hairpin}}$, as determined by the HPLC peak areas, over time. a) From a stock solution of $d(CG)_9$ (100 μ*M*) in autoclaved miliQ water, 10 μL was withdrawn and diluted with 100 m*M* NaCl and 20 m*M* Tris-HCl buffer to a final volume of 100 μL (10 μ*M*). b) From a stock solution of $d(CG)_9$ (100 μ*M*) in100 m*M* NaCl and 20 m*M* Tris-HCl buffer, 10 μL was withdrawn and diluted with autoclaved miliQ water to a final volume of 100 μL (10 μ*M*).

As shown in Figure 2.10, the hairpin and duplex conformation of $d(CG)_9$ is dynamic upon changes in salt concentrations in the sample. When the hairpin conformation was exposed to 100 μ*M* NaCl buffer, the hairpin transitioned to a duplex conformation. Similarly, when the solution containing duplex was diluted with water the duplex transitioned to a hairpin

conformation. The transition from the hairpin to duplex conformation can be explained by zero order rate law kinetics, with a rate constant of 0.012 μ*M*/hr. However, the rate law for the transition from the duplex to the hairpin conformation could not be determined because the transition from the duplex to the hairpin conformation occurs very quickly, and is dependent on the concentration of NaCl in solution being either in the sample or the running buffer.

The relationship between hairpin and duplex conformations, and the effects of salt on these structures have previously been examined experimentally[164] and *in silico*[165,166]. As an example, in a study conducted by Marky and colleagues (1983), the structural transition of a self-complementary DNA sequence, d(CGCCAATTCGCG), in the presence of NaCl with concentrations ranging from 0.001- 0.1 *M* was examined using differential scanning calorimetry (DSC), temperature dependent UV-Vis spectroscopy, and temperature dependent CD spectroscopy[164]. The results suggested that CD spectroscopy was unable to resolve the differences in conformation. UV-Vis spectroscopy, on the other hand, showed that when the DNA sequence was treated with 0.1 *M* or 0.0001 *M* NaCl a monophasic or biphasic transition resulted, respectively[164]. Based on previous NMR melting studies of d(CGCCAATTCGCG) in 0.1 - 0.01 *M* NaCl it was determined that the monophasic transition was the result of the conversion of duplex to single strand, while the biphasic transition was caused by two sequential transitions, *i.e.*, melting of the duplex followed by melting of a hairpin structure[164]. The melting temperatures of the duplex and hairpin were found to be 30ºC and ~70ºC, respectively[164].

2.3 Differential scanning calorimetry of d(CG)$_9$

Previously in this lab DSC was used to examine base flipping of 2'-deoxyguanosine (unpublished). Upon analysis of the results, it was suggested that DSC may not be appropriate to examine DNA base flipping as the energy barrier for *anti* to *syn* transitions may be too small to

detect as evidenced by the absence of a signal in thermal profiles obtained (data not shown). In this thesis, DSC was attempted to examine structural differences of the oligonucleotide $d(CG)_9$. Although DSC has been used to study oligonucleotide structures in the literature, here we intend to develop a basic understanding of the technique with the future possibility of examining oligonucleotides that have been chemically modified.

2.3.1 Thermal analysis

DSC was performed on $d(CG)_9$ (100 μ*M*) three times in 20 m*M* Tris-HCl buffer containing 100 m*M* NaCl, and the results were analyzed using Origin. Origin analyzes the dataset by fitting the calorimetric data obtained to a non-linear least square regression (Figure 2.11). The thermal melt temperaturea (T_m) and calorimetric enthalpy (ΔH_{cal}) are allowed to vary in order to obtain the best fit. To evaluate the fit of the curve to the data, Origin performs a λ^2 statistical test. To determine ΔHvH, Origin derives ΔHvH from the obtained calorimetric data using the following expression:

$$C_p = C_{pN}\left[\frac{K_{eq}\Delta C_{pA}}{1+K_{eq}} + \frac{K_{eq}\,\Delta\text{HvH}\,\Delta H_{cal}}{(1+K_{eq})^2 RT^2}\right] + \cdots \qquad [18]$$

where C_{pN} represents the heat capacity of the N^{th} peak, and ΔC_{pA} represents the change in heat capacity of peak A.

Analysis of the calorimetric data for $d(CG)_9$ duplex found that the average T_m is 97.2 ± 0.6 ºC, the average of the C_p is 2.7 kcal/mol·ºC, and the average of the ratio $\frac{\Delta H_{cal}}{\Delta\text{HvH}}$ is 1. The reduced λ^2 for each trial found that the P-value is less than 0.00001 which is less than α (0.01), which means that the relationship described by the curve represents a good fit to the data.

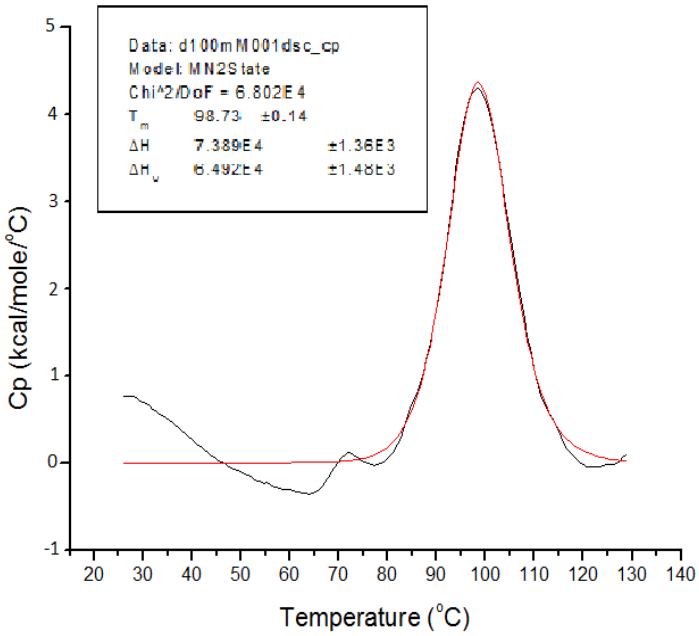

Figure 2.11. DSC thermogram for one of three trials of $d(CG)_9$ (100 μ*M*) in 20 m*M* Tris-HCl buffer containing 100 m*M* NaCl. The traces in black and red represent the experimental data and the non-linear fit of the experimental data performed by Origin, respectively.

Examination of the DSC thermogram of $d(CG)_9$ (Figure 2.11) found that the ratio of $\frac{\Delta H_{cal}}{\Delta H_{vH}}$ supports a two-state unfolding mechanism, which suggests that the primary conformation is in the B-DNA duplex conformation based on the folding kinetics discussed earlier. Additionally, the average T_m obtained by DSC of 97.02 ± 0.57 ºC does not agree with the T_m of 76.4 ºC provided by the supplier (Integrated DNA Technologies, IDT), likely because of how the T_m is calculated. Unfortunately, IDT did not provide the method used to calculate the T_m of the oligonucleotides they produced. However, the T_m of oligonucleotides provided by suppliers is determined empirically, based on the conditions assumed under which annealing occurs such as: the pH of the system, cation concentration, and concentration of the primer sequence. As an example, the oligonucleotide properties calculator by Kibbe (2007) predicts the T_m of an

oligonucleotide duplex using three different methods[167]. The first method is known as the nearest neighbors (NN) model and is used to calculate the T_m of oligonucleotides between 8 and 40 base pairs[167]. The NN model calculates the T_m based on the thermodynamic relationship between entropy, enthalpy, free energy and temperature[167]. From Equation [14] the relationship between the free energy and concentration of reactants and products at equilibrium can be rewritten to generate the following expression[167];

$$\Delta G = RT_m ln\left(\frac{[DNA \bullet primer]}{[DNA][primer]}\right) \quad [19]$$

where R represents the universal gas constant, $[DNA \bullet primer]$ represents the concentration of the DNA-primer complex, $[DNA]$ represents the concentration of DNA, and $[primer]$ represents the concentration of the primer. Rearranging for T and inserting appropriate correction factors yield the following expression:

$$T_m = \frac{\Delta H - 3.4\frac{kcal}{K\ mole}}{\Delta S + Rln\left(\frac{1}{[primer]}\right)} + 16.6\ log_{10}[Na^+] \quad [20]$$

where the $-3.4\frac{kcal}{K\ mole}$ and $16.6\ log_{10}[Na^+]$ terms represent correction factors for the free energy change and concentration of salt in the system. NN model requires experimental thermodynamic parameters ΔH and ΔS to calculate the T_m of an oligonucleotide.

The second and third methods are very similar where both methods are modified versions of the Marmur Doty formula[167,168]:

$$T_m = 2(A + T) + 4(C + G) - 7 \quad [21]$$

where T_m represents the melt temperature of the oligonucleotide duplex, A, T, C and G represent the number of 2'-deoxyadenosine, thymidine, 2'-deoxycytosine and 2'-deoxyguanosine in the sequence, respectively. The -7 term is a correction factor.

The equations used for the basic melting temperature and salt adjusted melting temperatures are displayed below:

Basic melting temperature formula[167]

$$T_m = 64.9 + \frac{41(G + C - 16.4)}{(A + T + G + C)} \quad [22]$$

Salt adjusted melting temperature[167]

$$T_m = 2(A + T) + 4(G + C) - 16.6\, log_{10}(0.050) + 16.6 log_{10}[Na^+] \quad [23]$$

The $16.6 log_{10}[Na^+]$ term is a correction factor that accounts for the concentration of salt in the system.

Oligonucleotide property calculators use modified versions of the Marmur Doty formula to determine the T_m that best represents the actual measured value. The oligonucleotide calculator by Kibbe (2007) accounts for different conformations, base stacking energy, oligonucleotide length, and the contribution from the amount of cationic charge[167].

Using the three methods to calculate the T_m of the $d(CG)_9$ duplex gave values of 68.5 ºC, 74.3 ºC, and 75.0 ºC respectively, which was closer to the T_m reported by IDT (76.4ºC). The theoretical methods provide a useful approximation of the actual T_m of a $d(CG)_9$ duplex; however, the oligonucleotide properties calculator might not account for a mixture of

conformations in a solution. For this reason, experimental methods should be performed to verify the T_m of the sequence of interest. In a study conducted by Owczarzy and colleagues (2003), the effect of sodium ion concentration on double stranded DNA was examined[169]. Owczarzy and colleagues compared the T_m of oligonucleotides that were predicted using empirical equations to the T_m of oligonucleotides that were determined experimentally by DSC or UV-Vis[169]. Owczarzy and colleagues examined 48 dsDNA and compared the T_m that was obtained experimentally to the T_m that was predicted. It was found that the average error of the T_m of the oligonucleotides when comparing the two methods was 1.6ºC [169].

2.4 Conformational study of 2'-deoxyadenosine treated under different conditions

Previous NMR experiments in this lab revealed that incubation of 2'-deoxyadenosine (dA) and thymidine (T) in water or concentrated ammonium hydroxide led to different distance constraints as evidenced by Nuclear Overhauser Effect spectroscopy (NOESY) signal intensities. The current project will determine the proportion of C3'-*endo* ($^{2'}E_{3'}$) and C2'-*endo* ($^{3'}E_{2'}$) conformations of dA in water at either 25ºC or 7ºC, based on the nuclear Overhauser effect (NOE) distance and torsion angle constraints, both obtained from NMR experiments. The obtained physical parameters are then compared to those of existing crystal structures to validate the results obtained by NMR spectroscopy, and to determine if the conformation is similar to or different from those reported in the literature.

2.4.1 Torsion angles

The torsion angles were solved by using an online calculator based on a generalized Karplus equation derived by Haasnoot and colleagues (1980)[170]. The online calculator works by determining the dihedral angle of a Newman projection when provided with four residues, two of which that correspond to either the front or the back of the Newman projection, and the $^3J_{H,H}$

value obtained by NMR spectroscopy. The calculator produces four plausible torsion angles, it is then up to the researcher to interpret which values are acceptable according to the system that is analysed (Table 2.0). Analysis of the $^{3}J_{H,H}$ value and the torsion angles for dA in D_2O at 25ºC and 7ºC produced similar results suggesting that the conformations are the same.

Table 2.1. Torsion angles of proton pairs derived from $J^3_{H,H}$ coupling constants for 2'-deoxyadenosine at 25ºC and 7ºC.

Atoms	Multiplicity	pairings	25ºC $J^3_{H,H}$ (Hz)	25ºC Torsion angle	7ºC $J^3_{H,H}$ (Hz)	7ºC Torsion angle
1'	dd	1'-2'a	7.5	137	7.3	135
		1'-2'b	6.4	31	6.7	30
3'	ddd	3'-2'a	6.1	48	6.0	48
		3'-4'	3.1	120	3.0	119
		3'-2'b	3.1	120	3.0	119
4'	ddd	4'-3'	3.2	121	3.3	121
		5'a-4'	4.2	34, 110	3.5	38, 106
		4'-5'b	3.1	60, 115	3.2	59, 116
5'a *	dd	5'a-5'b	12.8		12.8	
		5'a-4'	3.4	58, 117	3.2	59, 116
5'b *	dd	5'b-5'a	12.6		12.8	
		5'b-4'	4.3	33, 111	4.0	35, 109
2'a	ddd	2'a-2'b	14		13.9	
		2'a-1	7.7	139	6.9	134
		2'a-3'	6.2	47	6.9	42
2'b	ddd	2'b-2'a	14.1		14.1	
		2'b-1'	6.3	40	6.3	40
		2'b-3'	3.3	111	3.2	110

d: doublet of doublets; dd: doublet of doublets; ddd: doublet of doublet of doublets

* Two torsion angles are possible because it is impossible to determine which peak is responsible for H-5'a or H-5'b on the HNMR spectra.

2.4.2 Distances obtained by NOE

To determine the distance between proton pairs, Equation [9] was used. The reference distance was selected as the distance between atoms H-2'a and H-2'b from the structure solved by Sato and colleagues (1964)[171]. Analysis of the interproton distances for dA in D_2O at 25ºC and 7ºC produced similar results suggesting that the conformations are similar.

Table 2.2. Interproton distances solved based on NOE between proton pairs for 2'-deoxyadenosine at 25 C^{o} and 7 C^{o} reported in Å.

	D_2O, 25^{o}C Distance between protons	D_2O, 7^{o}C Distance between protons
2'a-2'b*	1.58	1.58
2'a-5'a	2.95	3.19
2'a-5'b	3.00	3.14
4'-2'b	3.13	3.27
2'a-3'	2.19	2.17
2'b-3'	2.77	2.70
3'-5'b	2.71	2.52
3'5'a	2.55	2.57
1'2'b	2.14	2.15
2'a-8	2.56	2.71
4'-1'	2.86	3.07
1'-8'	2.61	2.71
8'-3'	3.23	3.20

2.4.3 Comparison of NMR data against crystal structures

In order to verify the physical parameters obtained by NMR experiments, structures solved for adenosine and 2'-deoxyadenosine in the literature were compared. These structures were pre-processed by addition of hydrogen atoms or removal of auxiliary molecules. The

structures were overlaid and a pairwise comparison between two structures using a root mean squared displacement (RMSD) calculation was performed (Table 2.2). An RMSD calculation is a measure of difference between a set of values[172]. An RMSD of zero would indicate that the structures are the exact same. By comparing structures to each other this allowed for a direct examination of conformational flexibility and diversity of the structures.

Table 2.3. Comparison of RMSD values of reported structures of adenosine and 2'-deoxyadenosine.

[a]	Sato, et al. (1964) [b,e]	Goto, et al. (2004) [c,d,e]	Klooster, et al. (1991) [c,f]	Caminit, et al. (1999) [c,g]	Smith, et al. (2004) [c,d,g]	X.P.Fu et al. (2007) [c,e]	Lai, et al. (1972) [c,e]
Sato, et al. (1964) [b,e]		1.55	0.25	0.75	1.3	0.5	0.22
Goto, et al. (2004) [c,d,e]	1.45		1.47	1.56	1.22	1.54	1.33
Klooster, et al. (1991) [c,f]	0.25	1.47		0.07	1.46	0.10	0.01
Caminit, et al. (1999) [c,g]	0.75	1.56	0.07		0.97	0.05	0.06
Smith, et al. (2004) [c,d,g]	1.3	1.22	1.46	0.97		1.37	1.37
X.P.Fu, et al. (2007) [c,e]	0.5	1.54	0.10	0.05	1.37		0.07
Lai, et al. (1972) [c,e]	0.22	1.33	0.01	0.06	1.37	0.07	

a All of the atoms were used to compute the RMSD with the exception of the H-2' (2'-deoxyadenosine) and the 2'-OH (adenosine)

b: 2'-deoxyadenosine; *c*: adenosine; *d*: crystalized with picrate derivative; *e*: X-ray crystallography; *f*: neutron diffraction; *g*: X-ray powder diffraction

2.4.4 Comparisons of crystal and NMR data

In order to determine if the crystal and NMR data share a similar conformation, both the torsion angles and interproton distances from the crystal structures were measured using mercury 2.0. and compared to those obtained by the NMR experiments (Figure 2.12).

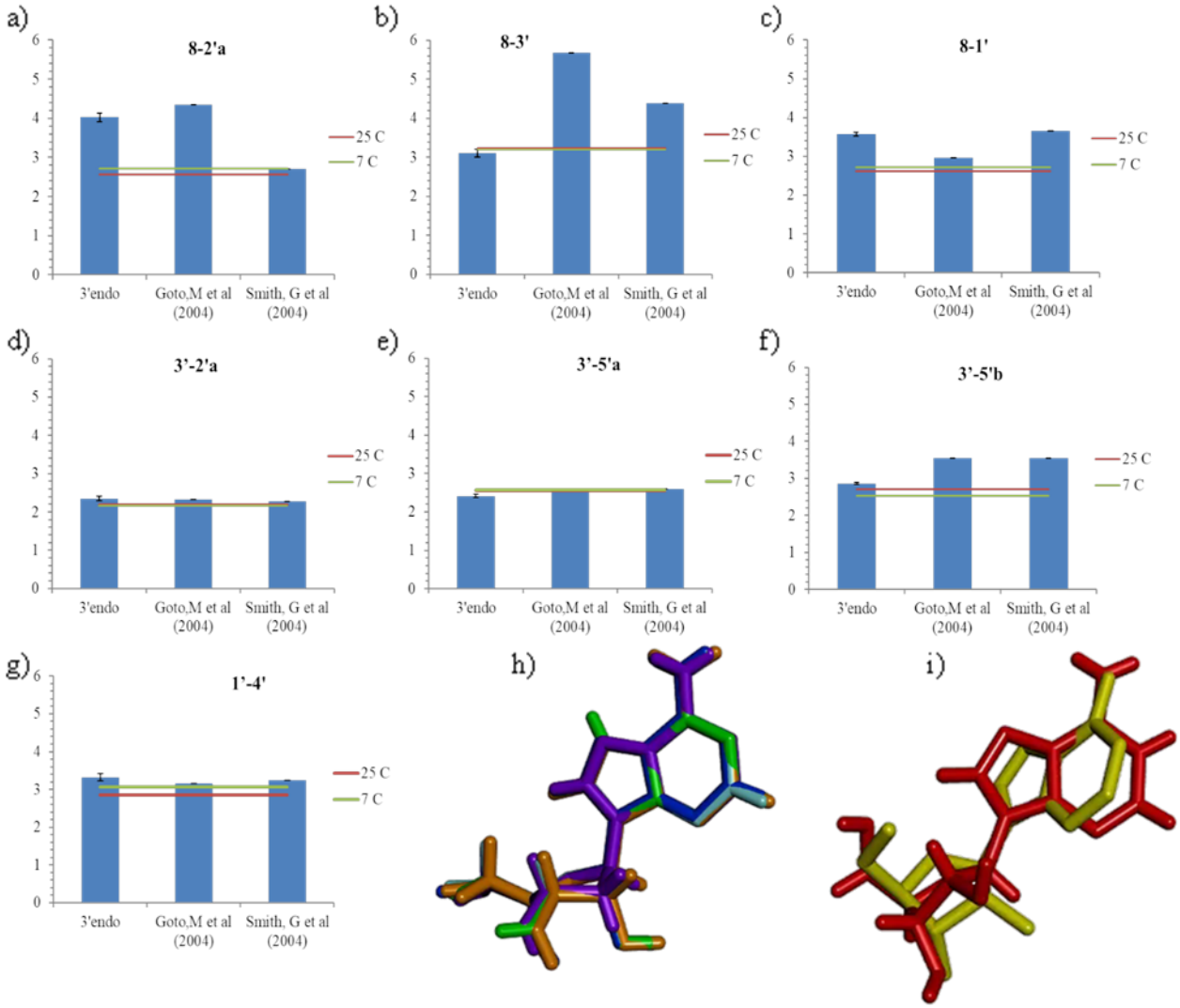

Figure 2.12. a)-g) Histogram comparing the interproton distances between coupled atoms for the average of the C3'-*endo* conformations found in the literature (Figure 2.12: h), the structure solved by Goto et al, 2004[173], and the structure solved by Smith et al, 2004[174] against the the NOE distances for 2'-deoxyadenosine in D_2O at 25ºC and 7ºC. h) Overlaid conformations of 2'-

deoxyadenosine in the C3'-*endo* conformation found in the literature, obtained by; Sato, 1964[171] (purple), Caminite et al., 1999[175] (green), Fu et al., 2007[176](dark blue), Klooster et al., 1991[177](orange), and Lai et al., 1972[178] (cyan). i) Overlaid conformations of adenosine obtained by Goto et al., 2004[173] (yellow), and Smith et al., 2004[174] (red).

The conformation of the sugar pucker for all of the structures retrieved from the literature are in the C3'-*endo* conformation with the exception of the structures reported by Goto and colleagues[173], and Smith and colleagues[174], where the sugar ring is in the C2'-*endo* conformation. The nitrogenous base, on the other hand, is in the *syn* conformation for each structure, with the exception of the structure reported by Goto and colleagues which is almost parallel to the furanose ring[173]. The difference in the structures is attributed to the fact that the structure reported by Goto and colleagues was solved from adenosine co-crystalized with a picrate derivative[173].

Comparing the interproton distances for the proton pairs between 8-2'a, 8-3', and 8-1' obtained from crystal structures against those obtained by NMR for dA at 25ºC and 7ºC, only the interproton distance for 8-2'a was in agreement with the structure reported by Smith and colleagues[174]. The histogram plots for the interproton distances that correspond to the furanose ring showed little variations between structures, with the exception of the 3'-5'b proton pair, where the interproton distances reported by Goto and colleagues[173] and Smith and colleagues[174] were similar, and the interproton distances between the average of the C3'-*endo* conformations of dA at 25ºC and 7ºC were similar. The lack of agreement in the interproton distances when comparing the crystal structures to NMR data of dA at 25ºC and 7ºC suggests that the conformation of the nitrogenous base relative to the furanose ring is different compared to the structures found in the literature.

Closer examination of the 2D NOESY spectra indicated a COSY-type artifact as evidenced by the deterioration of the 2'a-2'b signal. To confirm the presence of a COSY-type artifact, a 1D NOE was performed by irradiating H-2'a. Upon irradiation of the H-2'a hydrogen atom, a COSY-type artifact was found with the H-1' (Figure 2.13, highlighted in the oval).

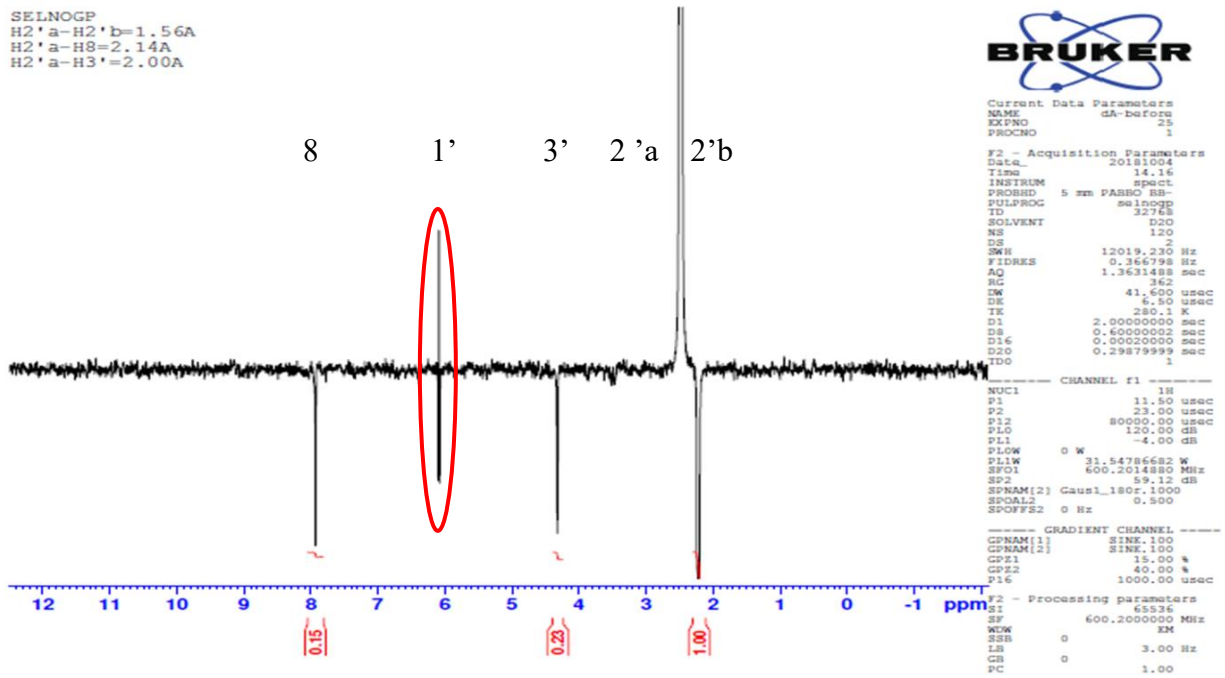

Figure 2.13. 1D NOE where H-2'b was irradiated. The signal in highlighted by the red oval represents the NOE signal that possesses the COSY-type artifact.

In a study conducted by Levitt and Warshel (1977), the energetics of sugar puckering of the furanose ring in ribose and deoxyribose was examined[179]. Levitt and Warshel implemented constraints on the system during energy minimization of the furanose ring of ribose/deoxyribose in order to find the lowest energy path between stable conformations. Energy minimization or geometry optimization is a process that evaluates the energy of any conformation, determines the nearest energy minima, and then changes the geometry of the conformation to reduce the energy

of the conformation[180]. The potential energy is calculated by a force field concept. A force field is a set of functions and constraints that are used to define the potential energy of the molecule[181]. As an example, a generalized force field equation called Chemistry at Harvard Macromolecular Mechanics (CHARMM) is described by the following[182]:

$$E_{pot} = \sum_{Bonds} U_{Bonds} + \sum_{Angles} U_{Angles} + \sum_{Dihedrals} U_{Dihedrals} + \sum_{Improper} U_{Improper} + \sum_{Electrostatic} U_{Electrostatic} + \sum_{Lennard-Jones} U_{Lennard\ Jones} \quad [24]$$

Where E_{pot} represents the total potential energy of the system, the first and second terms describe the bonded interactions between two and three atoms, that is, the bond stretching energy, U_{Bonds}, and the bond angle bending energy, U_{Angles} respectively[182]. The third and fourth terms describe the torsional angle energies between four atoms, that is, the dihedral angles energy, $U_{Dihedrals}$, and the improper angle energy $U_{Improper}$[182]. The fifth and sixth terms describe the interactions between non-bonded atom pairs, that is, the electrostatic interactions, $U_{Electrostatic}$, and the Lennard-Jones potential $U_{Lennard\ Jones}$[182]. Optimizing the conformation of the structure by removing any unwanted steric hindrances or torsion angles present in the structure would lead to a reduction in the potential energy of the system[182].

Levitt and Warshel used the Quantum Mechanical Consistent Force Field method for PI electrons (QCFF/ PI) program to perform an energy minimization of the system[179]. During energy minimization, the furanose ring was forced to move along the pseudorotation pathway by a constant energy, and the dihedral angles ψ' (O3'-C3'-C4'-C5'), τ_3 (C2'-C3'-C4'-O1') (Figure 2.14 a) and the angle of pseudorotation, W, were constrained. To simplify the computation, NH_2 was used to represent the nitrogenous base, as at the time this was less computationally

demanding. By implementing constraints on the system, Levitt and Warshel constructed an energy potential plot that describes the relative potential energy for the conformations of the furanose ring along the path of pseudorotation (Figure 2.14 b). It was found that the C3'-*endo* and C2'-*endo* conformations possessed the lowest potential energies, and the potential energy difference between the conformations was 0.6 kcal/mol or 1.4 kcal/mol if τ_3 or W was constrained, respectively. In comparison to the potential energy difference between the conformation with the highest potential energy O1'-*exo*, and C3'/C2'-*endo*, the difference was ~ 5 kcal/mol or ~ 2 kcal/mol if τ_3 or W was constrained, respectively. When structures solved by X-ray crystallography were compared to the conformations on the energy potential plot, it was found that the structures solved by X-ray crystallography tended to possess a conformation that was similar to the lower energy conformations.

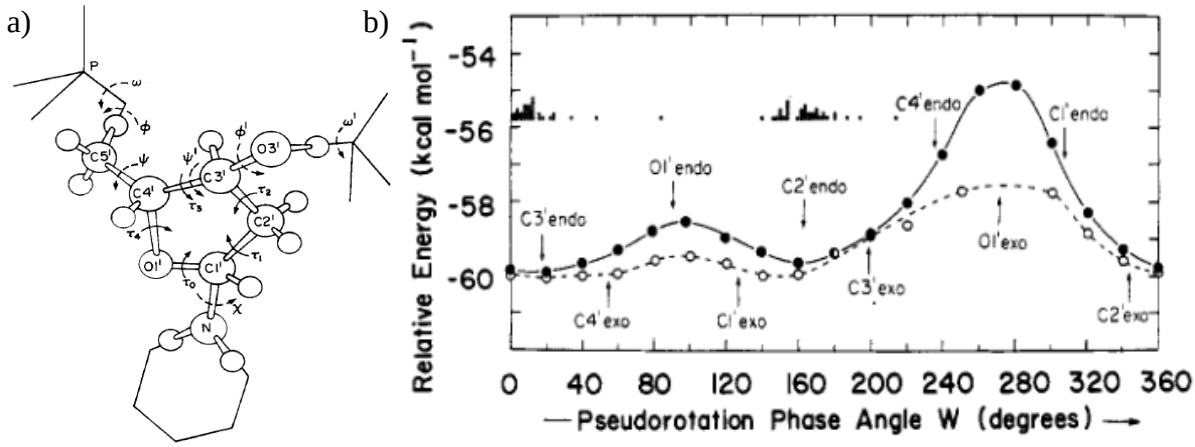

Figure 2.14. a) Ring torsion angles of the furanose ring b) Ring torsion angles as the angle of pseudorotation W is constrained to values between 0 and 360°. The solid line shows the energy variation when all five torsion angles are constrained to the path of pseudorotation. The dashed line shows the energy variation when only τ_3 is constrained to the path of pseudorotation. The dot histograms mark the angles of pseudorotation observed in furanose structures solved by X-

ray crystallography. Figure a) and b) used with permission from: Levitt, M.; Warshel, A. Extreme Conformational Flexibility of the Furanose Ring in DNA and RNA. *Journal of American Chemical Society* 1978, *100* (9), 2607–2613.

In a similar study Floppe and colleagues examined the energetics of nucleotide flipping about the glycosyl torsion angle χ, by performing energy minimization on dA, dG, dC, and dT using GAUSSIAN98[183]. It was found that the energy barrier between the *anti* and *syn* conformation was ~3-8 kcal/mol, however the potential energy of the conformation was also dependent on the type of nitrogenous base examined. As an example, the potential energy of the *syn* conformation of pyrimidines is higher than purines[183].

Collectively, the work conducted by Levitt and Warshel, and Floppe and colleagues found that the potential energy barriers between C3'-*endo* and C2'-*endo*, and *anti*- and *syn*-rotation are relatively low, suggesting that these conformational fluctuations occur quite readily in solution, and may therefore be difficult to observe different conformations using NOESY.

A factor that confounds the structural analysis encountered in this thesis was related to the potential challenges in properly interpreting NMR data, especially NOE. In a review by Suyama and colleagues, the authors examined the techniques used in reports of numerous structural revisions of 504 terrestrial and marine natural products between 2005-2010[184]. It was found that NMR techniques were responsible for ~50% of the misassigned structures, of which ~22% of the misassignment was the result of misinterpretation of NOE, suggesting that the majority of errors are configurational rather than constitutional in nature[184]. Configurational errors are those that relate to the spatial arrangement of an atom (or a substituent) in a molecule that cannot be determined through the rotation of a single bond[185], while constitutional errors are

related to a molecule's connectivity[82]. Upon further examination of the misassigned structures, it was found that the abundance of configurational errors was linked to an inappropriate interpretation of the NOE data and spectroscopic comparison[184]. With these observations in mind, the literature highlights the importance of careful evaluation to ensure that the molecular models are consistent with the NOE constraints. It has to be borne in mind that there are many factors that can perturb the intensity of an NOE.

Some factors that attribute to misleading NOE signals include COSY-artifacts, spin diffusion, 2D vs 1D NOE, and conformational flexibility. COSY cross-peaks have the same phase as the diagonal, while NOESY cross-peaks are opposite in phase. As such, COSY cross-peaks may coincide with the NOESY cross-peaks and cause a loss of intensity of the NOESY signal, resulting in a COSY-artifact. COSY-artifacts are caused by residual scalar coupling from the last 90º pulse that is used in both COSY and NOESY[186,187]. The 90º pulse causes coherence transfer between J-coupled spins[32], leading to the reduction in the intensity of the NOESY cross-peak. Because of COSY-artifacts, interpretation of results becomes difficult[188], and calculating the distance between spin active nuclei may be inaccurate because of the differences in signal between the reference peak and the peak of interest. Furthermore, spin diffusion or relay effect, are chain reaction type NOEs that occur when an NOE induces relaxation with unintended nearby neighbouring nuclei, may also lead to Total Correlation Spectroscopy (TOCSY)-artifacts[189,190] (Figure 2.15).

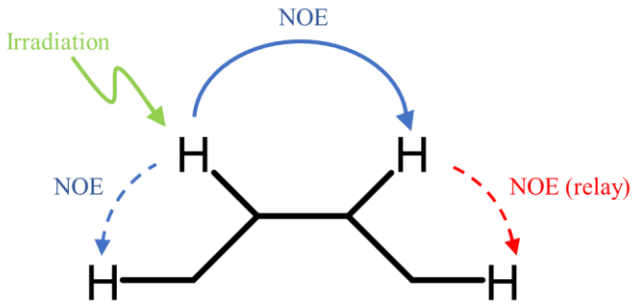

Figure 2.15. Cartoon representation of spin diffusion. The green arrow represents the proton that is irradiated. The solid blue arrow and dashed arrows represent the protons that are induced by the proton irradiated. The red dashed arrow represents the unintended proton that is induced by the proton irradiated.

TOCSY spectroscopy is a 2D NMR technique that creates correlations where magnetization is transferred between protons that are directly coupled to each other or between distant protons up to five or six bonds away, as long as there are couplings between every intervening proton[191]. As a result, the presence of TOCSY-artifacts can lead to false correlations in NOE.

2D NOESY and 1D NOESY differ in that the detected signal in 1D NOESY is a function of only one time variable, which results in a spectrum with only one frequency axis. In 2D NMR spectroscopy the detected signal is a function of several time variables[97,192]. 1D in comparison to 2D offers better sensitivity[190] and can reveal very small NOEs that may otherwise be missed in 2D. However, 2D is usually preferred over 1D because of convenience, where 2D unlike 1D reduces the amount of overlap in the data and allows for easier interpretation but at the cost of limiting selective irradiation. Because of the limit in protons that are selectively irradiated, 2D datasets are found to produce less reliable distances as a result of insufficient mixing times[193]. To mitigate some of the discrepancies with 2D NOESY, Butts and colleagues examined the

interproton distances of strychnine (Figure 2.16) determined by 1D and 2D NOE and Rotating Overhauser Effect (ROE) in various solvents, and assessed the accuracy and precision against crystal structures and conformations generated by computation using time-dependent density functional theory (TDDFT)[194].

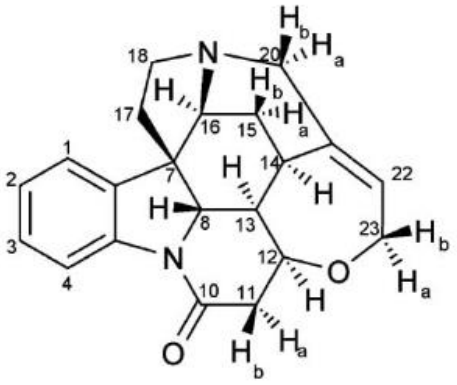

Figure 2.16. Molecular structure of strychnine

Butts and colleagues examined strychnine because of its rigid structure, relatively high solvation energy, and isotropic tumbling nature[194]. To examine the solvent effects on NOE signals, NMR experiments were carried out in $CDCl_3$, C_6D_6, and DMSO-d_6 with a 500 MHz NMR spectrometer[194]. Butts and colleagues collected 128 scans for samples in $CDCl_3$ with a relaxation time of 600 ms, 1024 scans for samples in C_6D_6 with a relaxation time of 200 ms, and 1024 scans for samples in DMSO-d_6 with a relaxation time of 600 ms[194]. To calculate the interproton distances from the NOE signals, Butts and colleagues used the intensity of the vicinal protons H15a and H15b of strychnine and the distance measured between the vicinal proton pair from the TDDFT calculations to calibrate the NOEs, being 1.76 Å[194]. To assess the interproton distances solved by NMR spectroscopy, TDDFT, and X-ray crystallography, NOE data for strychnine solvated with $CDCl_3$ and C_6D_6 and averaged interproton distances obtained for each spectra were used, which gave 55 unique interproton distances[194]. The solved interproton

distances extracted from 1D and 2D NOE experiments were then plotted against the computed TDDFT interproton distances. For the 1D NOE it was found that the precession had an average absolute error of 0.09 Å and a standard deviation of 0.11 Å for distances up to 4.5 Å[194]. In comparison to the X-ray crystal structure the error of interproton distance was found to be 1.4–4.3% (std 1.2%–4.3%)[194]. The 2D NOE method, on the other hand, was found to be less accurate than the 1D NOE, with few long range (>3.5 Å) interactions obtained, and the precession had an average absolute error of 0.10-0.23 Å[194]. The inaccuracies derived from 2D NOE are due to the nature of 2D NOE, where errors are introduced as a result to truncation of t_1 and the overlap from adjacent strong correlations such as J-coupled nuclei[194]. Butts and colleagues then examined the effect of solvent on NOEs. It was found that solvents do affect 1D NOE signals[194]. In this respect, it was found that measurement made in DMSO-d_6, C_6D_6 and $CDCl_3$ led to an average error of 0.2 ± 0.14 Å, 0.1 ± 0.11 Å, and 0.1 ± 0.10 Å, respectively[194]. Thus, measurements in DMSO-d_6 gave the highest average error and standard deviation, likely because of the higher viscosity of DMSO[194]. As a result, the NOE build-up rate is quicker in DMSO-d_6, resulting in a shorter mixing time of 200 ms[194]. Upon correcting for the mixing time, measurements in DMSO-d_6 gave an average error of 0.13 ± 0.10 Å[194].

Conformational flexibility describes a molecule's ability to form various stable conformers. Because of the flexibility that is displayed by some molecules, interpretation of NOEs becomes difficult, as the NOE may be representative of an average of the various conformations instead of a static structure[195]. Although the examination of flexible molecules may be difficult, solving the structure for flexible molecules is possible, but may require the use of computer-assisted structure elucidation (CASE). CASE is a technique that uses software to generate possible molecular structures that are consistent with a supplied set of spectroscopic

data. CASE was first used in 1968 by four individual research groups, and has become increasingly utilized for the purpose of structural elucidation[196–200]. In a study conducted by Butts and colleagues, the accuracy in determining interproton distances using NOE data obtained from flexible molecules was examined[195]. Butts and colleagues performed TDDFT calculations on 4-propylaniline to generate an ensemble of low energy conformations that are located at a local minima on an energy potential landscape and fitted the conformational data to the NOE data[195]. This was done to treat the population as an ensemble of low energy conformations rather than an average of all conformations[195]. In this manner, the structure of four low energy conformations was determined, that is, 4-propylaniline where the propyl chain was in the *anti* (1a and 1b) and *gauche* (2a and 2b) conformation (Figure 2.17) [195]. The difference between 1a and 1b is that they have opposite pyramidalisation of the amino group, while 2a and 2b defer in their rotation around the C5-C6 bond, that is, by 120^{o}. To assess the distances, the average distance between the protons H3 and H5 from the simulated conformations was used[195]. The distances between H3-H6, H3-H7, and H5-H7 were then compared to simulated conformations and the distances found through NOE (Table 2.3) [195].

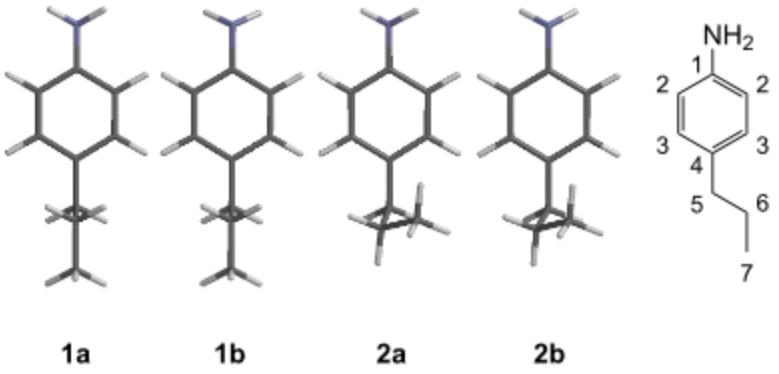

Figure 2.17. Four low energy conformations of 4-propylaniline that were obtained by B3LYP/6-31G. Conformations 1a and 1b are in the *anti*-conformation, while conformations 2a and 2b are in the *gauche* conformation. Figure used with permission from Jones, C. R.; Butts, C. P.; Harvey, J. N. Accuracy in Determining Interproton Distances Using Nuclear Overhauser Effect Data from a Flexible Molecule. *Beilstein Journal of Organic Chemistry* 2011, *7*, 145–150.

Table 2.4. Distances for proton pairs that gave rise to NOE signals. The distances were solved and compared to values calculated by B3LYP/6-31G[195].

Interproton pairs	r_{NOE} (Å)	r_{calc} (Å)	% error (Å)
H3-H5	2.77	2.77	-
H3-H6	3.21	3.34	3.83
H3-H7	4.16	4.05	2.54
H5-H7	3.13	3.08	1.67

Through these comparisons, Butts and colleagues demonstrated that NOESY is a very accurate technique when used with a computational approach, the mean percentage error of the NOE distances obtained by 2D NOESY vs computation was 2.68%.

2.5 Re-examination of the denaturation of DNA secondary structures

Previous work in this lab examined the structural fluctuation of a self-complementary oligonucleotide sequence $d(CG)_6$ using high performance liquid chromatography (HPLC)[201-202]. This self-complementary oligonucleotide sequence was used in the HPLC studies due to its ability to form secondary structures such as hairpins. Thus, reverse-phase and non-denaturing anion exchange HPLC were found to be unreliable and often lead to the misinterpretation of the results, as multiple species are observed in the chromatogram under these HPLC conditions. Elution of the anion exchange column under denaturing conditions, on the other hand, allowed for reproducible resolution of a variety of sequences. The use of denaturing conditions in anion exchange HPLC has led to an interest in establishing conditions required for efficient DNA denaturation. Despite the fact that DNA denaturation is commonly practiced in chemistry, biochemistry and molecular biology, detailed study on the minimal conditions required for this process remains elusive. This project aimed to study a variety of organic modifiers and compare their relative strength to one another using a non-self-complementary mixed sequence of dsDNA. Toward this end, the denaturation process was monitored by UV-Vis spectroscopy, and the structural changes were studied by HPLC.

2.5.1 UV-Vis spectroscopy

Urea was first chosen for the denaturation experiments, as it has been well documented and shown to effectively denature DNA. In order to normalize absorbances in the presence of urea, an internal standard was required. Toward this goal, citrate-modified gold-nanoparticles (GNP) (Cytodiagnostics) were used, as GNPs are not known to bind DNA. Analysis of the UV-Vis data, however, suggested that citrate modified GNPs may not be a good candidate as an

internal standard, as evidenced by the shift of absorbance at 535 nm of GNPs to 690 nm in the presence of DNA (5'-d(CTTTAAGAAGGAGATATACCA)-3') (Figure 2.18).

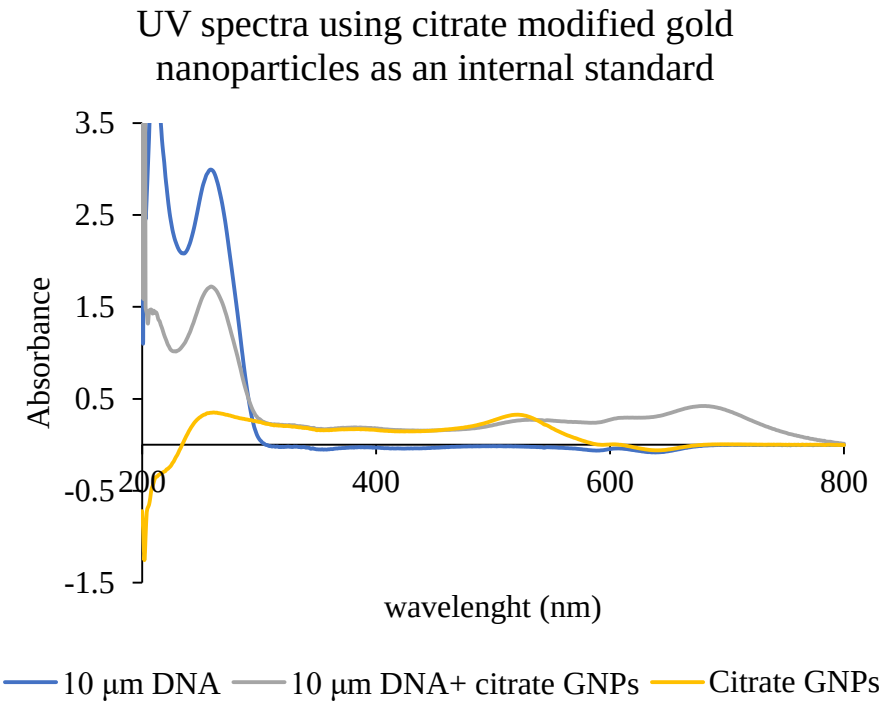

Figure 2.18. UV-Vis spectra of citrate modified gold nanoparticles and ds DNA

Subsequently, polyethylene glycol (PEG) modified gold nanoparticles were evaluated as an internal standard in the denaturation experiments.

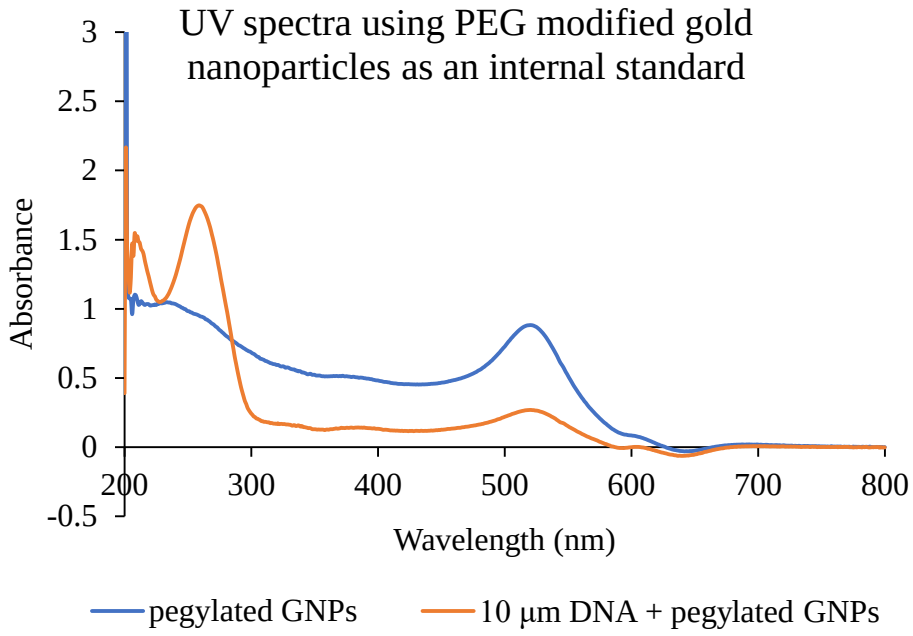

Figure 2.19. UV-Vis spectra of PEG modified gold nanoparticles and ds DNA

Analysis of the UV-Vis spectra (Figure 2.19) using PEG modified GNPs as an internal standard suggested that the PEG modified GNPs do not bind to DNA, however, the PEG modified GNPs appeared to bind to the plastic or glassware as evidenced by left-over residue of the GNPs on the plastic or glassware used, and by the decrease in the absorbance in the UV-Vis spectrum (data not shown). For this reason, an external standard (dsDNA, (5'-d(CTTTAAGAAGGAGATATACCA)-3')) was sought. When a sample is treated by an organic modifier in a solid form, the sample becomes diluted by an unknown amount. As a result, the absorbance of the treated sample is lower than that of the un-treated sample. To determine the dilution factor of the treated sample, an external standard approach is used. By diluting an identical sample of DNA with buffer rather than organic modifier while keeping the volume the same the dilution factor can be determined by calculating the ratio of the absorbance at 260 nm before and after the sample was diluted with buffer. Using the dilution factor, the spectrum of the

sample treated with organic modifier can be adjusted, and a meaningful result can be determined using the spectrum before treatment and the processed spectrum after treatment.

In the literature urea at a concentration between 6-8 *M* is used in denaturing polyacrylamide gel electrophoresis[203,204]. In this thesis the concentration of urea was kept constant (8 *M*), while the pH was varied from 8, 10, and 12.5. HPLC was performed under denaturing conditions to verify if denaturation occurred.

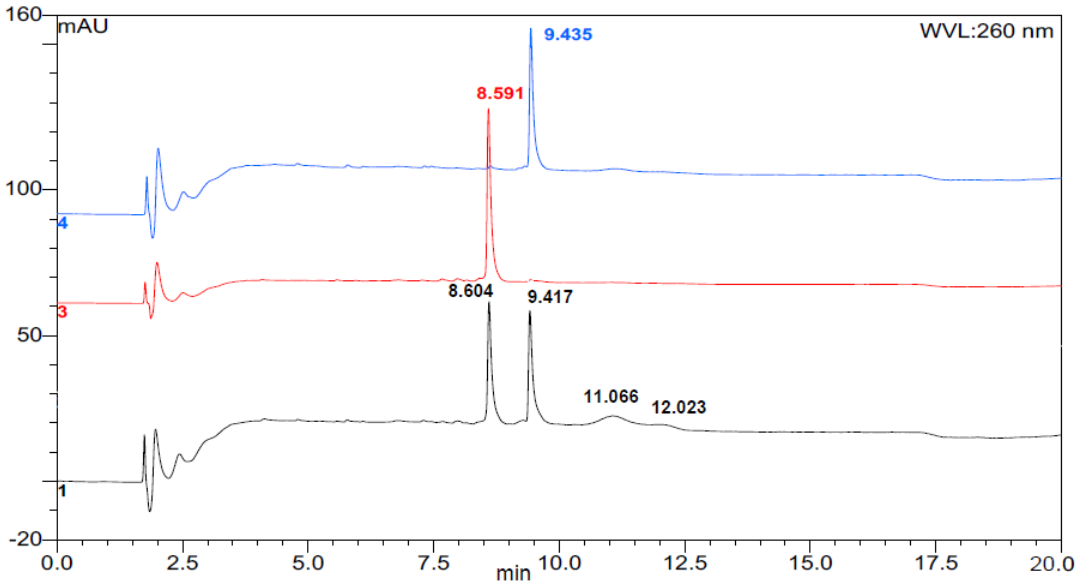

Figure 2.20. AEX HPLC chromatogram of dsDNA (mixed sequence, black) and the ssDNA oligonucleotides used, mer 1 (5'-d(CTTTAAGAAGGAGATATACCA)-3', blue), and mer 2 (5'-d(TGGTATATCTCCTTCTTAAAG)-3', red). The column was eluted under denaturing conditions. The column was eluted with a linear gradient of 10-70% 1*M* NaCl over 20 minutes, 30% 8 *M* urea buffer (pH 12.5).

Analysis of the HPLC chromatogram (Figure 2.20) suggests that 8 *M* urea at a pH of 12.5 denatures the majority of dsDNA present, with the exception of two small broad peaks with a retention time of 11.06 min, and 12.02 min respectively. Denaturation of dsDNA formed two

ssDNA strands, mer 1 (5'-d(CTTTAAGAAGGAGATATACCA)-3') with a retention time of 8.59 min and mer 2 (5'-d(TGGTATATCTCCTTCTTAAAG)-3') with a retention time of 9.44 min.

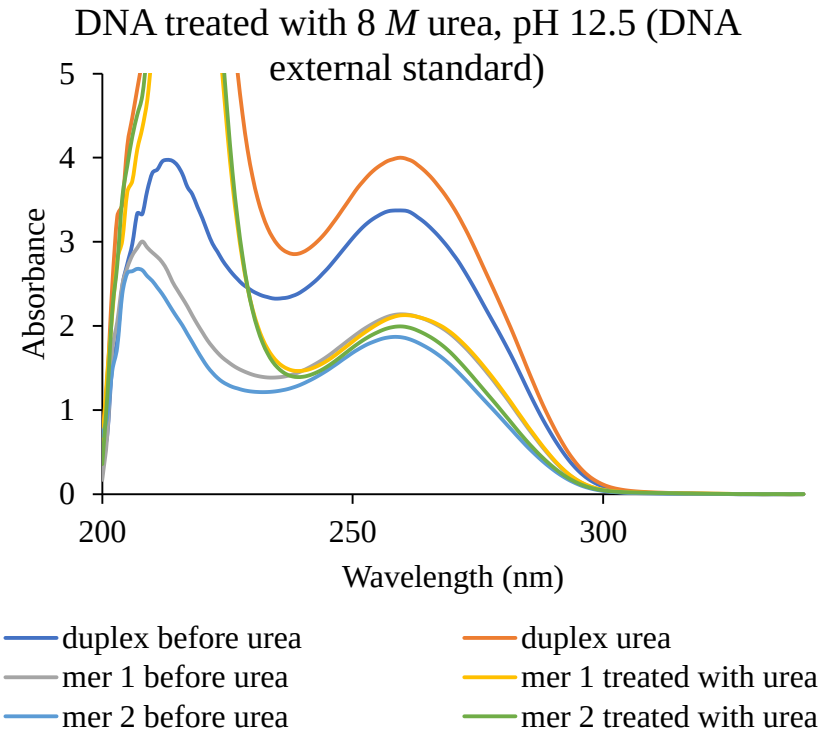

Figure 2.21. dsDNA and ssDNA treated with 8 *M* urea at a pH of 12.5 after adjusting for the dilution factor

Analysis of the UV-Vis spectra of dsDNA treated with urea using the external standard approach determined that the average percent hyperchromicity for three trials was $16.2 \pm 6.3\%$. This inconsistency in the percent hyperchromicity might be due to the interaction of urea with ssDNA. To study the effects of urea on the absorbance of ssDNA, mer 1 and mer 2 were also treated with 8 *M* urea and examined using the external standard method. When mer 1 and mer 2 were treated with 8 *M* urea, the percent difference of the absorbance at 260 nm was $19.2 \pm$

14.2% and $8.05 \pm 0.91\%$ respectively. The difference in absorbance of the untreated and treated ssDNA strands suggests that addition of urea might lead to shift of tautomeric equilibrium of nucleobases. Tautomers are structural isomers that can interconvert in a rapid equilibrium[205]. Structural isomers are molecules that possess the same molecular formula but with differing connectivity[206]. Nucleic acids possess solvent-exchangeable hydrogen atoms that allow for tautomerism of the carbonyl and amino functional groups, resulting in a keto ↔ enol and amino ↔ imino tautomerization (Figure 2.22).

Although it is unknown in the literature whether the presence of urea leads to shift of tautomeric equilibrium of nucleobases and causes a change in absorbance because of the $\pi \rightarrow \pi^*$ transition[207]because of increased conjugation displayed by the enol and amino forms. The effect of urea on the tautomeric equilibrium of nucleobases and oligonucleotides will be investigated in future work.

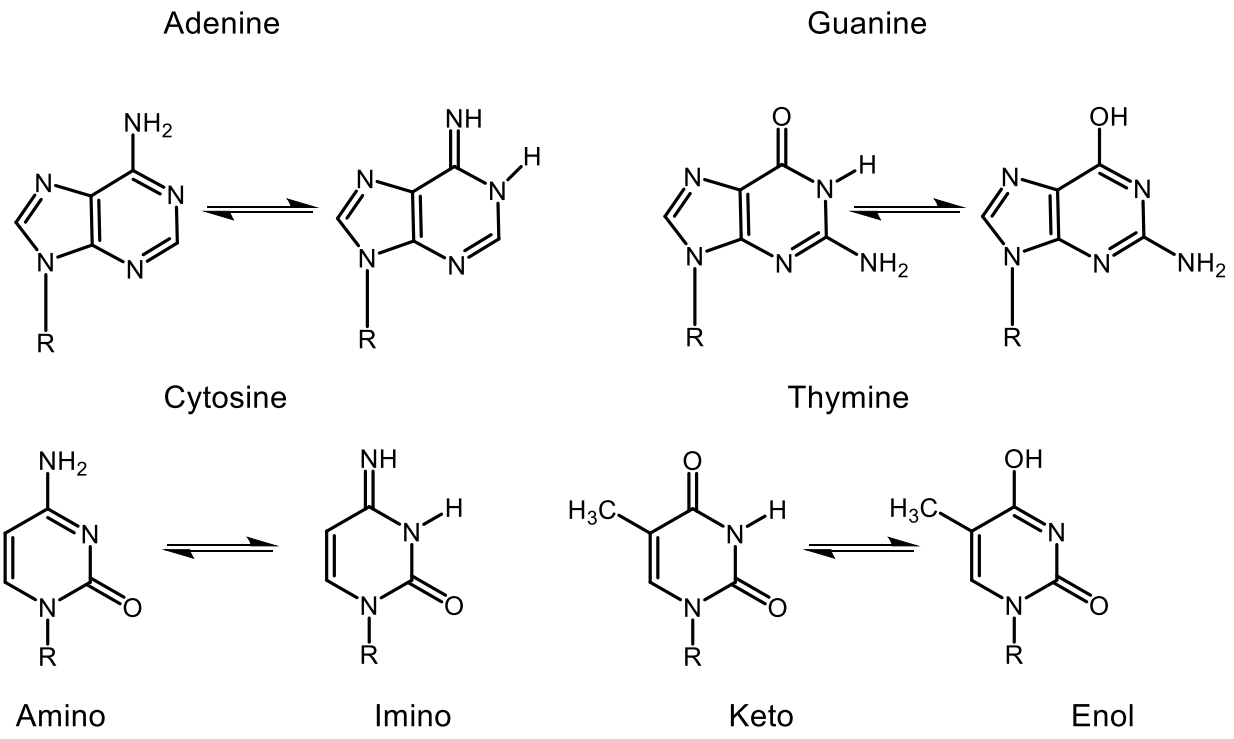

Figure 2.22. Examples of possible amino ↔ imino and keto ↔ enol tautomers of nucleobases.

It is well-documented in the literature that denaturation of DNA leads to hyperchromicity, but the degree of hyperchromicity is not well established. A study conducted by Wang and colleagues examined the denaturation of the *easA* gene in *Escherichia coli* under various physical and chemical treatments[208]. To quantify the degree of denaturation, Wang and colleagues used the following relation[208]:

$$Denaturation(\%) = \left(\frac{Final\ A_{260} - Blank\ A_{260}}{Initial\ A_{260}} - 1\right) \times 200 \quad [25]$$

Where $Initial\ A_{260}$and $Final\ A_{260}$ represent the absorbance of DNA at 260 nm before and after treatment with a denaturant respectively. $Blank\ A_{260}$ represents the absorbance at 260 nm of the buffer or reagents used to denature DNA.

At 100% denaturation and by assuming that the initial absorbance at 260 nm is equivalent to 1, and that the absorbance of the blank is equivalent to 0, the final absorbance at 260 nm would have to be 1.5 times higher than the initial absorbance. From Equation [4], this suggests that degree of hyperchromicity for a completely denatured strand of dsDNA is equivalent to 33.3%. However, Equation [25] does not account for tautomeric effects, which may falsely indicate a higher degree of hyperchromicity. As an example, Herskovits examined the effect of urea (10 *M*) on the denaturation of salmon DNA,[209] and reported a 46-48% change in hypochromicity/hyperchromicity, which would translate to 170-184 % change in % denaturation according to Equation [25].

Currently there does not seem to be a method that separates tautomeric and hyperchromic effects. The total absorbance of the system can be explained by a modified Beer Lampert equation:

$$\Sigma Absorbance = \Sigma \varepsilon_{ds\ DNA} l[ds\ DNA] + \Sigma \varepsilon_{ss\ DNA}\, l[ss\ DNA\ ] + \Sigma \varepsilon_{tautomerized\ ss\ DNA} l[tautomerized\ ss\ DNA] \quad [26]$$

where, the total absorbance is dependent on the absorbance of the amount of dsDNA, ssDNA, and ssDNA that has undergone tautomerization. This approach will be investigated in future work.

2.5.2 Future work

Much work will be carried out in order to complete a thorough investigation into the minimal conditions required for denaturation using the organic modifying agents such as urea, formamide, ethanol, methanol, dimethyl sulfoxide (DMSO), polyethylene glycol (PEG), and guanidinium hydrochloride, and at varying pHs. Currently the external standard method that was

developed is able to quantify denaturation of DNA through the hyperchromic effect. However, only one condition (8 *M* urea, pH 12.5) was examined, and consistency between trials remains poor. As previously mentioned the recent analysis of the dsDNA treated with urea (8 *M*, pH 12.5) has led us to believe that the sample is possibly partially denatured as evidenced by HPLC, and tautomerization may have occurred as evidenced by UV-Vis spectroscopy. Tautomerization is significant because it can lead to changes in absorbance at 260 nm. As a result it may be necessary to obtain the absorbance spectrum of completely denatured dsDNA as a positive control. It is proposed that thermal denaturation coupled with UV-Vis spectroscopy can be used to obtain a spectrum of ssDNA sample. Regarding tautomerization of the ssDNA strands, this may be a result of human error as a result of the low volumes used. It is suggested that the internal standard approach be revisited. Citrate, and PEG gold modified nanoparticles have been shown to be inappropriate internal standards because the gold modified nanoparticles either bind to DNA or the plasticware used. It is suggested that gold oxide nanoparticles may prove to be a better internal standard. Gold oxide nanoparticles are not known to bind to DNA, and the oxygen counter ion should not bind to the plasticware. After the completion of this project it is suggested that other DNA secondary structures are examined i.e. Z-DNA, and G-Quadruplex. As well as examining the use of native HPLC to verify denaturation of dsDNA treated with organic modifiers.

2.6 Conclusion

In conclusion it was found that the analytical techniques used to examine structures of DNA have been proven to be reliable techniques. Analysis of circular dichroism and ultra violet visible spectroscopy of B- and Z-DNA at 1m*M* using a pathlength of ~ 0.1 mm produced reliable spectra and allow for future conformational studies of nucleic acids at biologically relevant conditions.

Rehydration of $d(CG)_9$ using either water or NaCl buffer led to the formation of either a hairpin or duplex conformation, as evidenced by HPLC. When the hairpin conformation was subjected to NaCl buffer, the hairpin conformation would unfold and form a duplex conformation. It was found that the transition from hairpin to duplex occurs through zero order rate law kinetics, and the rate constant was determined to be 0.012 μ*M*/hour. When the duplex conformation was subjected to NaCl, the duplex conformation would unfold and form a hairpin conformation. However the transition from duplex to hairpin occurs rapidly, as a result we were unable to determine the rate law for the transition.

Differential scanning calorimetry performed on $d(CG)_9$ suggests that $d(CG)_9$ undergoes a non-two-state unfolding mechanism. It was found that the average of the ΔH_{cal} was 100.2 ± 2.1 kcal/mol, the average of ΔH_{VH} was 53.1 ± 1.6 kcal/mol, the average T_m was 97.0 ± 0.6 ºC, and the average C_p was 2.8 kcal. However, examination of oligonucleotides by DSC leaves much to be desired. For instance, the DSC machine used requires 150 μL of sample at a concentration of 100 μ*M*. With this in mind, reproducibility is quite challenging as the DSC machine is largely affected by slight void volumes in the sample and/or reference cells, where the thermogram produced results in data that are uncharacteristic of the material of interest being examined.

Analysis of the conformation of 2'-deoxy adenosine in water using distance and torsion constraints obtained by NOESY and COSY spectroscopy proved to be unreliable because of the presence of COSY-like artifacts in the NOESY spectra.

8 *M* urea at a pH of 12.5 proved to effectively denature the mixed sequence. However, it was impossible to determine the amount of DNA that was denatured because of hyperchromic and tautomeric effects. Future work is required to find a method that can isolate hyperchormic and tautomeric effects that are responsible for the change in absorbance in the UV-Vis spectra.

Chapter 3: Materials and methods

3.1 NMR spectroscopy

^{1}H- NMR, NOSY NMR, and DOSY NMR spectra experiments were preformed using a 600 MHz using a Bruker AV600 spectrometer, equipped with a BBO-Z gradient ATMA probe head. Tetramethylsilane was used as an internal standard. *J* values and chemical shifts are given in ppm and Hz, respectively. Deuterium oxide (99.0 atom % D) obtained from C/D/N Inc was used in the preparation of NMR samples.

2-D NOESY experiments used a gradient selection pulse sequence; the mixing time was set to 600 milliseconds corresponding to small molecules, with the line broadening set to 0.3 Hz. For each experiment 256 increments were acquired zero filled to 1024. Diagonal peaks were negatively phased to give positive NOEs in the processed spectrum and chemical exchanges would be negative.

2-D DOSY experiments were run using a pseudo 2-D sequence using a stimulated echo and LED using bipolar gradient pulses for diffusion. For each experiment the evolution time was set to 100 milliseconds, the diffusion gradient was set to 2000 microseconds, and the gradient ramp was set to 32 steps. Processing was done using a Fourier transform and base line correction only in the proton dimension. Diffusion coefficient was calculated using linear regression of the diffusion formula, Equation [27]:

$$I(q) = I_0 e^{-Dq2\Delta'} \qquad [27]$$

where I represents the observed intensity, I_0 represents the reference intensity, D represents the diffusion coefficient which is given in units (log m^2/s), Δ' is composed of two terms; $\Delta - \delta/3$

where Δ represents the diffusion time and δ represents the duration of the applied gradient, q is the product of $\gamma g \delta$ where γ represents the gyromagnetic ratio, and g represents the amplitude of the applied gradient,

Interpretation of spectra obtained was performed using the program TopSpin 4.1.1

3.2 Circular dichroism spectroscopy

CD experiments were carried out using a Jasco J-600 Spectropolarimeter. Samples were read at a speed of 50 nm/min at 1 nm resolution for 20 or 60 scans with a bandwidth of 1 nm, slit width of 1000 μm, and sensitivity ranging from 50 mdeg-1000 mdeg.

3.3 Ultraviolet visible spectroscopy

UV-Vis spectrophotometric measurements were recorded using an Agilent Technologies Cary 4000 spectrophotometer.

3.4 Cuvettes

Samples were examined using two quartz cuvettes that are commercially available with either a 10 mm pathlength (Cary 50 microcell 150 μL) or a 1 mm pathlength (Hellma). A homemade cuvette called a FlexiCell was also used and is discussed later in this chapter.

3.5 HPLC

Chromatographic studies of DNA samples were performed using a Dionex ICS-300 Chromatography system, fitted with a ThermoScientific DNAPac^{TM} 200 anion exchange column (4x250 mm). Samples were detected at wavelengths of 260, 250, 275, and 225 nm. Samples were injected manually and the column was eluted at a flow rate of 0.7 mL/min. The HPLC system was controlled with a Chromeleon program.

Elution program under non-denaturing conditions:

Linear gradient, 10-55% 1*M* NaCl over 10 minutes, 10% 250 *mM* Tris HCl buffer (pH 8.5), the remaining component being water.

Elution program under denaturing conditions:

Linear gradient, 10-70% 1*M* NaCl over 20 minutes, 30% 8 *M* urea buffer (pH 12.5), the remaining component being water.

3.6 Differential scanning calorimetry

Differential scanning calorimetry (DSC) experiments were performed using a vp-cap DSC microCalorimeter. A thermal histogram for the DSC machine was established by running 7 scans of miliQ water, followed by 7 scans of the buffer, and 1 scan of the sample. The starting temperature was set to 20°C, the final temperature was set to 130°C, the pressure was set to 40 psi, the scan rate was set to 240°C/hr, and the pre-scan thermostat was set to 15 minutes. Prior to starting a run, the sample was degassed for 45 minutes. Samples at a concentration of 100 µ*M*, and was loaded into the sample cell using 250 µL of solution; any excess solution was withdrawn out of the sample cell. After the sample was run, interpretation and normalization of the thermoprofiles were performed using the Origin software. The Origin software performs an internal normalization where the raw data from the DSC output, which is in units of mcal/min, is normalized using the scan rate, and the data are corrected to cal/°C. The data are normalized again using the concentration of the sample and a set volume of 140 µL, and the data is corrected to kcal/mole/°C. Further data manipulation such as baseline correction can be performed. Here a progressive base line was used to correct for any variables relating to the heating process.

The DSC machine was cleaned by first withdrawing the denatured sample followed by rinsing the reference and sample cell with autoclaved miliQ water. A 25% contrad solution was

injected into the sample and reference cell, was heated from 25°C to 130°C, was allowed to cool to room temperature, and was rinsed out multiple times using miliQ water.

3.7 3D Molecular Visualization Software

3.7.1 Swiss PDBViewer

Swiss PDBViewer is a molecular graphics program that allows for the rendition and analysis of protein structures acquired through experimentation, such as X-ray crystallography, proton nuclear magnetic resonance (proton NMR specrroscopy), and electron microscopy. The models for the structures that are produced by Swiss PDBViewer may be used to generate comparisons of various types of proteins. Here Swiss PDBViewer was used to calculate RMSD values of overlaid structures.

3.7.2 Persistence of Vision Ray Tracer

Persistence of Vision Ray Tracer (POV-RAY) is a program that is used to generate images with a high degree of realism. Here, POV-RAY was used to increase the resolution of images produced by Swiss PDBViewer.

3.7.3 Discovery Studio

Discovery Studio 2017 is a program that was used to overlay crystal structures, manipulate, and measure dihedral angles.

3.7.4 Mercury

Mercury is a program that was used to measure the distance between selected atoms.

3.8 Reagents & Oligonucleotides

All chemical reagents were purchased from Sigma-Aldrich, TCI America, Fluka, Alpha Aesar, ACP, Thermo Fisher, and Rasayan Inc, without further purification prior to use. Gold nanoparticles were purchased from Cytodiagnostics. All oligonucleotides were purchased from Integrated DNA Technologies (IDT). HPLC eluents were filtered through 0.4 μm membrane filters.

3.9 Annealing

Annealing was performed using a Mastercycler Nexus gradient thermal cycler. First the samples were heated to 95°C over 10 min and then slowly cooled down to 25°C over a period of 50 min. Samples were stored at 4 °C until use.

3.10 Lyophilization

Lyophilization of samples was carried out using a Savant Speed-Vac system at room temperature.

3.11 Buffer preparation

Buffer 1: 150 mL, 100 *mM* NaCl, 20 *mM* TRIS-HCl

A buffer (Buffer 1) was prepared by withdrawing 15 mL of 1 *M* NaCl, and 30 mL of 100 *mM* tris-HCl, and 105 mL of autoclaved miliQ water to yield a solution of 100 *mM* NaCl, and 20 *mM* tris-HCl (pH of 7.5).

Buffer 2: 4 *M* NaCl, 20 *mM* TRIS-HCl

A buffer (Buffer 2) was prepared by dissolving NaCl (35 g), and 30 mL of 100 *mM* tris-HCl and 120 mL of autoclaved miliQ water to yield a solution of 4 *M* NaCl, and 20 *mM* tris-HCl (pH of 7.5).

1 *M* NaCl solution

A 1 *M* NaCl solution was prepared by dissolving NaCl (5.8 g) in autoclaved miliQ water to a final to a volume of 100 mL

100 *mM* TRIS-HCl solution

A 100 *mM* Tris-HCl solution was prepared by dissolving TRIS (1.2 g) in 80 mL of autoclaved miliQ water, the pH was adjusted to 7.5 and the solution was diluted to a final volume of 100 mL using autoclaved miliQ water.

Buffer 3: Phosphate buffered saline pH 7.4

A buffer (Buffer 3) was prepared by dissolving two tablets of phosphate buffered saline consisting of 0.02 *M* phosphate buffer, 0.0054 *M* potassium chloride and 0.244 *M* sodium chloride ph 7.4 in 200 mL of autoclaved miliQ water.

Buffers 4-7:1L, 8 M urea pH (8- 12.5)

A buffer (Buffer 4-7) was prepared by dissolving urea (480.5 g) in 1 L of autoclaved miliQ water, the stock solution was aliquoted into three 250 mL portions, and the aliquots were basified with $NaOH_{(aq)}$ to a pH of either 8, 10, or 12.5.

3.12 Preparation of $d(CG)_9$ samples for differential scanning calorimetry

From a stock solution of $d(CG)_9$ (1 m*M*) 275 µL was withdrawn, aliquoted into six equal portions, and lyophilized. Samples 1-3 were reconstituted using Buffer 1 to a volume of 250 µL (100 µ*M*), while samples 4-6 were reconstituted using Buffer 2 to a volume of 250 µL (100 µ*M*). All of the samples were annealed, and examined using DSC.

3.13 Circular dichroism study of DNA conformations at biologically relevant concentrations

To examine the effect of sensitivity, the CD spectropolarimeter was set to 200 mdeg and a series of (+)/(-)- camphorsulphonic acid (CSA) concentrations ranging from 26 *mM* (10 X), 20.8 *mM* (8 X), 10.4 *mM* (4 X), 5.2 *mM* (2 X), and 2.6 *mM* (1 X) was examined using a 1 cm quartz cuvette. Additionally, (+)/(-)-CSA at a concentration of 1 X was examined using varying sensitivities; 50 mdeg, 200 mdeg, 190 mdeg with a 1cm quartz cuvette. To investigate the effects of sensitivity and bandwidth, CSA at 1X, with a sensitivity of 200 mdeg and (+)/(-)-CSA at 4X, with a sensitivity of 1000 mdeg was examined with a bandwidth of; 2 nm, 1 nm, or 0.5 nm. Additionally 10 um of B-DNA $d(CG)_9$ at a sensitivity of 1000 mdeg, maximum band width and a 1 cm pathlength was examined. To investigate the effect of multiple scans, $d(CG)_9$ was examined using 20 and 60 scans at a 1 cm pathlength.

3.13.1 Design of the Flexicell

The Flexicell is composed of two cylindrical Teflon chambers/barrels with two single crystal calcium fluoride (CaF_2) windows. CaF_2 windows were selected because the transmission of CaF_2 is 130 nm-1mm, which is within the dynamic range used. Samples are loaded through two pinholes using a Hamilton syringe, and the pathlength can be adjusted by tightening the barrel assemblies through a graded threading system. The outer barrel assemblage is scaled with 50 tick marks along the circumference (Figure 3.1 a-g).

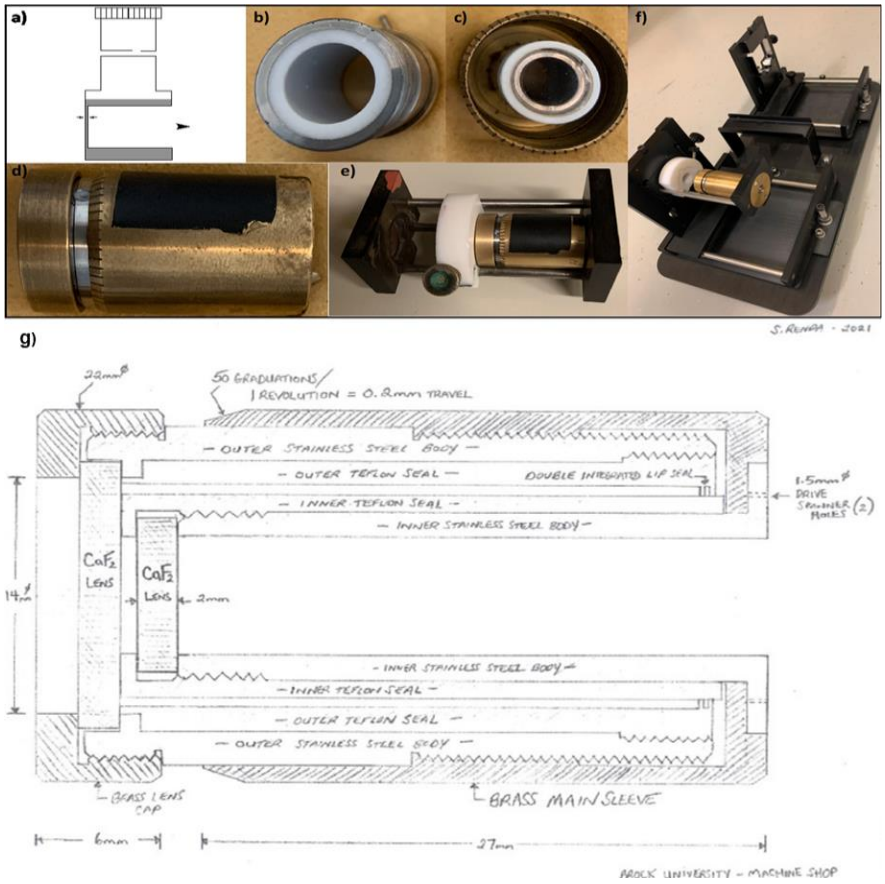

Figure.1. Sample cells with small and adjustable pathlengths. a). Commercially available Starna cylindrical cells; b and c) the two barrels of the adjustable cell; d) the assembled cell, e) the assembled cell on an adaptor, and f). Home-built adaptors for UV-Vis measurement g) schematic of the Flexicell, drawn by Steve Renda, Brock University Technical Services. Used with permission from: Vanloon, J.; Harroun, T.; and Yan. H. "Circular dichroism spectroscopy of DNA duplexes at near-biological concentrations." *Bioorganic & Medicinal Chemistry Letters*. 2021, (43),1-5.

3.13.2 Preparation of d(CG)$_9$ samples for CD experiments

From a stock solution of d(CG)9 (1 *mM*), 1200 µL was withdrawn and aliquoted into a 1000 µL and a 200 µL portion. The two ssDNA solutions were lyophilized, reconstituted with 100 µL of buffer 1 or buffer 2, annealed (5 *mM* ds B-DNA , and 1 *mM* ds Z-DNA respectively), and examined by CD and UV-Vis spectroscopy using the FlexiCell at 0 tick marks. Using the 5 *mM* d(CG)$_9$ ds B-DNA sample, a 2 *mM*, 1.7 *mM*. 1.5 *mM*, and 1 *mM* ds B-DNA sample was prepared by withdrawing; 20 µL, 17 µL, 15 µL, and 10 µL respectively, each sample was diluted to a final volume of 50 µL using buffer 1, and examined by CD and UV-Vis spectroscopy using the Flexicell at 0 tick marks. Samples were made fresh from a 5 *mM* stock solution in order to avoid effects that were caused by evaporation.

To save material after the 1 *mM* d(CG)$_9$ ds B-DNA and the 1 *mM* d(CG)$_9$ ds Z-DNA sample were examined, a set of dilutions was prepared ranging from 100 μM to 10 μM of either ds B or Z-DNA (Table 1). From the 1 *mM* solutions 20 µL was aliquoted, diluted with 180 µL of either buffer 1 or buffer 2 (100 μM ds B or Z-DNA) respectively, and examined by CD spectroscopy using a 1 cm quartz cuvette.

3.13.3 Preparation of mixed-sequence DNA samples for CD experiments

From two stock solution of two non-self-complementary DNA strands (mixed sequence) (5’CTTTAAGAAGGAGATATACCA 3’ and 5’ TGGTATATCTCCTTCTTAAAG 3’ (792 μM), 126 µL was withdrawn from each stock solution, combined, lyophilized, reconstituted with 100 µL of buffer 1, annealed (1 *mM* ds mixed sequence), and examined using CD and UV-Vis spectroscopy using the FlexiCell at 0 tick marks.

To save material after the 1 *mM* mix sequence sample was examined; a set of dilutions was prepared ranging from 100 μM to 10 μM (Table 3.1). From the 1 *mM* solutions 20 µL was aliquoted, diluted with 180 µL of buffer 1 (100 μM B- DNA), and examined by CD spectroscopy using a 1 cm quartz cuvette.

Table 3.1. $d(CG)_9$ and mix sequence set of dilutions preparation

Concentration (μM) *	Aliquoted from previous dilution (µL) †	Buffer added ††
100 μM ¶		
90	180	20
80	178	22
70	175	25
60	171	29
50	166	33
40	160	40
30	150	50
20	133	67
10	100	100

* Each sample was examined by CD spectroscopy using a 1 cm quartz cuvette

† Each sample was prepared from the previous dilution ie 90 μM was prepared by aliquoting 180 µL of the 100 μM sample and the aliquot was diluted with 10 µL of either Buffer 1 or buffer 2

†† Refers to the addition of either buffer 1 or Buffer 2 respectively.

¶ 100 μM was prepared by withdrawing 20 µL from the previous 1 mM ds B or Z-DNA sample and was diluted with 180 µL of either buffer 1 or buffer 2 (100 μM) respectively in order to save material.

3.13.4 Preparation of thymidine samples as standards

A stock solution of thymidine was prepared by dissolving thymidine powder (32 mg, $1.33*10^{-4}$ mol) using 6.63 mL of autoclaved miliQ water (20 *mM*). From the 20 *mM* stock solution a 5 *mM*, 1*mM*, and 0.5 *mM* solution was created. From the 20 *mM* stock solution, 1.63 mL was withdrawn and diluted to a volume of 6.5 mL using autoclaved miliQ water (5 *mM*). From the 5 *mM* solution 1.50 mL was withdrawn and diluted to a volume of 7.5 mL using autoclaved miliQ water (1 *mM*). From the 1 *mM* solution 2.5 mL was withdrawn and diluted to a volume of 5 mL using autoclaved miliQ water (0.5 *mM*). All of the samples were examined by UV-Vis and CD spectroscopy using a 1 cm, 1mm quartz cuvette, and the FlexiCell.

3.13.5 Preparation of bovine serum albumin samples

A stock solution of bovine serum albumin (BSA) was prepared by dissolving 66.4 mg with 1 mL of autoclaved miliQ water (100 μM). From the 100 μM sample a 10 μM, 1 μM, and 0.1μM was created. From the 100 μM sample 55.5 µL was withdrawn and diluted to 555 μM (10 μM). From the 10 μM sample 55 µL was withdrawn and diluted to 550 µL (1 μM). From the 1 μM sample 50 µL was withdrawn and diluted to 500 µL (0.1 μM). All of the samples were examined by UV-Vis and CD spectroscopy using a 1 cm and 1mm quartz cuvette.

3.13.6 Preparation of camphor samples

A solution of camphor sulfonic acid ((+)-CSA , (-)-CSA) was prepared by dissolving camphor powder (30 mg, $1.3*10^{-4}$ moles) with 5 mL of autoclaved miliQ water (26 *mM*, 100 X). From the 100 X stock solution a series of 10 X, 8 X, 4 X, 2X and 1X stock solutions were created. From the 100 X stock solution, 500 µL was withdrawn and diluted to a volume of 5 mL

using autoclaved miliQ water (26 *mM*, 10 X). From the 10 X solution 1.6 mL was withdrawn and diluted to a volume of 2 mL using autoclaved miliQ water (20.8 *mM*, 8 X). From the 8 X solution, 1 mL was withdrawn and diluted to a volume of 2 mL using autoclaved miliQ water (10.4 *mM*, 4 X) From the 4 X solution, 1 mL was withdrawn and diluted to a volume of 2 mL using autoclaved miliQ water (5.2 *mM*, 2 X). From the 2 X solution, 1 mL was withdrawn and diluted to a volume of 2 mL using autoclaved miliQ water (2.6 *mM*, 1 X). All of the samples were examined using a 1 cm and 1 mm quartz cuvette.

3.14 Kinetics of $d(CG)_9$ hairpin and duplex conformations

3.14.1 DOSY preparation of samples

From a stock solution of $d(CG)_9$ (1 *mM*) 60 µL was withdrawn, diluted with 270 µL of autoclaved miliQ water (200 µ*M*), aliquoted into two 150 µL portions (sample 1 and sample 2), and lyophilized. Sample 1 was then reconstituted with 150 µL of d_2O, while sample 2 was reconstituted with 150 µL of 100 *mM* NaCl, and 20 *mM* Tris-HCl pH 7.5 in d_2O. Samples 1 and 2 were then examined using DOSY and non-denaturing HPLC conditions.

3.14.2 Preparation of hairpin/duplex kinetic samples

From sample 1, 5 µL was withdrawn and diluted with autoclaved miliQ water to a final volume of 100 µL (10 µ*M*, sample 3). From sample 2, 5 µL was withdrawn and diluted with Buffer 1 to a final volume of 100 µL (10 µ*M*, sample 4). From sample 1, 5 µL was withdrawn and diluted with Buffer 1 to a final volume of 100 µL (10 µ*M*, sample 5). From sample 2, 5 µL was withdrawn and diluted with autoclaved miliQ water to a final volume of 100 µL (10 µ*M*, sample 6). Samples 3-6 were analyzed by non-denaturing HPLC conditions.

3.15 Denaturation of DNA

The work here discusses the methods used to normalize the spectral data obtained by UV-Vis spectroscopy for single stranded (ss) DNA and double stranded (ds) DNA when treated with an organic modifier such as urea ($CH_4N_2O(s)$) for the purpose of examining denaturation. Beer Lamperts law can be used to quantify the amount of UV-Vis activity that is displayed by a molecule. To determine the amount of denaturation (ds-DNA → ss-DNA), an internal and an external standard was used to determine the dilution factor of the DNA treated with urea. By taking the ratio of the absorbance at the λ_{max} of the internal or external standard before and after treatment the dilution factor can be determined. Gold nanoparticles 20 nm in diameter was selected as an internal standard because gold nanoparticles displays UV-Vis active properties (λ_{max}, 253 nm) because of LSPR, gold is chemically inert, and does not bind to DNA. Untreated dsDNA or ssDNA (5'-CTTTAAGAAGGAGATATACCA- 3'), and the complementary strand (5'- TGGTATATCTCCTTCTTAAAG- 3') was selected as the external standard of interest because the strand is non-self-complementary, and dsDNA and ssDNA can be used as positive controls to examine the effects of dilution. In addition to DNA, Thymidine (λ_{max}, 267 nm) was also examined using the external standard method in order to study any secondary effects that were caused by the urea treatment. The use of an internal/external standard is necessary to examine denaturation because dsDNA and ssDNA possess a similar lambda maximum (λ_{max}) at 260 nm, but the ε is approximately 25% greater. Thus, the use of a denaturing agent would simultaneously dilute the sample, and increase ε through the hyperchromic effect leading to a UV-Vis spectrum that may lead to specious correlations. By accommodating for the dilution factor using the internal/external standard approach, the spectrum of the post-treated DNA can be related to the spectrum of the pre-treated dsDNA by a ratio of the absorbances of the

internal/external standard at the λ_{max} taken pre-dilution and post-dilution. The dilution factor can be described by Equation [28]:

$$X = \frac{A_{standard\ pre-dilution}}{A_{standard\ post-dilution}} \quad [28]$$

where X represents the dilution factor, $A_{standard\ pre-dilution}$ represents the absorbance of the internal/external standard before the sample was diluted with urea, $A_{standard\ post-dilution}$ represents the absorbance of the internal/external standard before the sample was diluted with urea. The dilution factor can be used to convert the absorbance spectrum of the sample post-treatment to the reference frame of the sample where the absorbance was taken pre-treatment. Using the expression in Equation [4] the following equation can be used to convert the spectrum of the post-treated dsDNA sample to the reference frame of the spectrum of the un-treated sample, Equation [29]:

$$A' = X * A_{post-treatment} \quad [29]$$

where A' represents the adjusted absorbance that accounts for the dilution factor, X represents the dilution factor, and $A_{post-treatment}$ represents the absorbance of the sample treated with urea.

3.15.1 Preparation of organic modifiers

From Buffers 4-7, three 200 µL aliquots were withdrawn from each buffer with the exception of Buffer 7 where seven 200 µL aliquots were withdrawn. Each of the aliquots was dried using nitrogen gas for 24 hrs.

3.15.2 Preparation of B-DNA and gold nanoparticle internal standard

From a stock solution of two non-self-complementary DNA strands 5'-CTTTAAGAAGGAGATATACCA- 3' (792 μM) and 5'- TGGTATATCTCCTTCTTAAAG- 3' (792 μM), 13 µL was withdrawn from each and diluted to 1 mL (10 μM) with autoclaved miliQ water (samples 1 & 2). From each of the aliquots, 400 µL was withdrawn, combined together (sample 3). From samples 1, 2, 200 µL was withdrawn from sample. Each of the aliquoted samples were lyophilized, reconstituted with 200 µL of buffer 1 spiked with 6 µL of gold nanoparticles, were annealed, and analyzed using UV-Vis spectroscopy. The samples were used to reconstitute one of the urea aliquots from buffer 7; the urea treated samples were re-examined using UV-Vis spectroscopy.

3.15.3 Preparation of B-DNA and B-DNA external standard

From a stock solution of two non-self-complementary DNA strands 5'-CTTTAAGAAGGAGATATACCA- 3' (792 μM) and 5'- TGGTATATCTCCTTCTTAAAG- 3' (792 μM), 45.5 µL was withdrawn from each and diluted to 3.6 mL (10 μM) with autoclaved miliQ water (samples 1 & 2). From each of the aliquots, 1.2 mL was withdrawn, combined together (sample 3). From samples 1, 2, each sample was aliquoted into six 200 µL portions, while sample 3 was aliquoted into six 400 µL portions. Each of the aliquoted samples were lyophilized, and reconstituted with 200 µL of Buffer 1. The six aliquoted portions from sample 3 were annealed, and all of the aliquots were analyzed using UV-Vis spectroscopy.

From the partitioned samples 1-3, three of the six aliquots were used to reconstitute one of the urea aliquot buffers 4-7. Using a multichannel pipettor, 200 µL from the urea treated DNA samples were pipetted against 200 µL of the DNA external standards simultaneously. The remaining urea treated DNA was pipetted against buffer simultaneously, and was added to the

previously pipetted 200 µL of the urea treated DNA and DNA external standard respectively. The urea treated DNA samples and the diluted external DNA standard were analyzed using UV-Vis spectroscopy and non-denaturing HPLC conditions and denaturing HPLC conditions.

3.15.4 Preparation of thymidine and thymidine external standard

A stock solution of thymidine was prepared by dissolving thymidine powder (10 mg, $2.5*10^{-6}$ mol) using 5 mL of autoclaved miliQ water (0.5 *mM*). From a stock solution of 0.5 *mM* thymidine 400 µL was withdrawn and aliquoted into two 200 µL portions, and examined using UV-Vis spectroscopy. From the two aliquots, one sample was used to reconstitute one of the urea aliquots from buffer 7. Using a multichannel pipettor, 200 µL from the urea thymidine samples were pipetted against 200 µL of the thymidine external standard simultaneously. The remaining urea treated thymidine was pipetted against water simultaneously, and was added to the previously pipetted 200 µL of the urea treated thymidine and thymidine external standard respectively. The urea treated thymidine samples and the diluted thymidine external standard were analyzed using UV-Vis spectroscopy.

Chapter 4: References

(1) Altmann R (1889) Ueber Nucleinsäuren. Arch. f. Anatomie u. Phys-Iol:524–536.

(2) Miescher F (1871c) Ueber Die Chemische Zusammensetzung Der Eit-Erzellen. Medicinisch-Chemische Untersuchungen 4:441–460.

(3) Dahm, R. Discovering DNA: Friedrich Miescher and the Early Years of Nucleic Acid Research. *Human Genetics*. **2008**, *122* (6), 565–581.

(4) Kossel, A. Ueber Eine Neue Base Aus Dem Thierkörper. *Berichte der deutschen chemischen Gesellschaft*. **1885**, *18* (1), 79–81.

(5) Kossel, A.; Neumann, A. Darstellung Und Spaltungsprodukte Der Nucleïnsäure (Adenylsäure). *Berichte der deutschen chemischen Gesellschaft*. **1894**, *27* (2), 2215–2222.

(6) Kossel, A.; Neumann, A. Ueber Das Thymin, Ein Spaltungsproduct Der Nucleïnsäure. *Berichte der deutschen chemischen Gesellschaft*. **1893**, *26* (3), 2753–2756.

(7) Kossel, A. Über Das Agmatin. **1910**, *66* (3), 257–261.

(8) Brooker, R. J.; Bidochka, M. J.; Graham, L. E.; Hunter, F. F.; Widmaier, E. P.; Stiling, P. D.; Hasenkampf, C.; Riggs, C. D. *Biology*; McGraw-Hill Education, 2013.

(9) R. Katritzky, A.; A Ramsden, C.; Joule, J.; Zhdankin, V. 2.3 - Structure of Five-Membered Rings with One Heteroatom; 2010; pp 87–138.

(10) Schrauber, H.; Eisenhaber, F.; Argos, P. Rotamers: To Be or Not to Be? An Analysis of Amino Acid Side-Chain Conformations in Globular Proteins. *Journal of Molecular Biology*. **1993**, *230* (2), 592–612.

(11) Karplus, M. Contact Electron-Spin Coupling of Nuclear Magnetic Moments. *Journal of Chemical Physics.* **1959**, *30* (1), 11–15.

(12) Karplus, Martin. Vicinal Proton Coupling in Nuclear Magnetic Resonance. *Journal of American Chemical Society*. **1963**, *85* (18), 2870–2871.

(13) McGlashan, M. L. *Chemical Thermodynamics: Volume 1*; Royal Society of Chemistry, 2007.

(14) Banfalvi, G. *Apoptotic Chromatin Changes*; Springer Science & Business Media, 2009.

(15) Saenger, W. *Principles of Nucleic Acid Structure*; Springer Science & Business Media, 2013.

(16) Neidle, C. R. C. B. S. U. S.; Neidle, S. *Nucleic Acid Structure and Recognition*; Oxford University Press, 2002.

(17) Jacobsen, N. E. *NMR Data Interpretation Explained: Understanding 1D and 2D NMR Spectra of Organic Compounds and Natural Products*; John Wiley & Sons, 2016.

(18) Neidle, S. *Topics in Nucleic Acid Structure*; Springer, 1981.

(19) Neidle, S. *Principles of Nucleic Acid Structure*; Elsevier, 2010.

(20) Altona, C.; Sundaralingam, M. Conformational Analysis of the Sugar Ring in Nucleosides and Nucleotides. New Description Using the Concept of Pseudorotation. *Journal of the American Chemical Society*. **1972**, *94* (23), 8205–8212.

(21) Neidle, S. The Determination of Quadruplex Structures; 2012; pp 175–191.

(22) Roberts, R. J.; Cheng, X. Base Flipping. *Annual Review of Biochemistry*. **1998**, *67* (1), 181–198.

(23) Klimasauskas, S.; Kumar, S.; Roberts, R. J.; Cheng, X. Hhal Methyltransferase Flips Its Target Base out of the DNA Helix. *Cell*. **1994**, *76* (2), 357–369.

(24) Koolman, J.; Roehm, K. H. *Color Atlas of Biochemistry*; Thieme, 2011.

(25) Bates, A. D., Maxwell, A. *DNA Topology*; Oxford University Press, 2005.

(26) Bhattacharyya, D.; Majumdar, R. Structural Basis of DNA Flexibility. *Indian Journal of Biochemistry and Biophysics*. **2001**, *38* (1–2), 16–19.

(27) Bhattacharyya, D.; Kundu, S.; Thakur, A. R.; Majumdar, R. Sequence Directed Flexibility of DNA and the Role of Cross-Strand Hydrogen Bonds. *Journal of Biomolecular Structure and Dynamics*. **1999**, *17* (2), 289–300.

(28) Häse, F.; Zacharias, M. Free Energy Analysis and Mechanism of Base Pair Stacking in Nicked DNA. *Nucleic Acids Research*. **2016**, *44* (15), 7100–7108.

(29) Franklin, R. E.; Gosling, R. G. Evidence for 2-Chain Helix in Crystalline Structure of Sodium Deoxyribonucleate. *Nature*. **1953**, *172* (4369), 156–157.

(30) Watson, J. D.; Crick, F. H. C. Molecular Structure of Nucleic Acids: A Structure for Deoxyribose Nucleic Acid. *Nature*. **1953**, *171* (4356), 737–738.

(31) Mitsui, Y.; Langridge, R.; Shortle, B. E.; Cantor, C. R.; Grant, R. C.; Kodama, M.; Wells, R. D. Physical and Enzymatic Studies on Poly d(I–C).Poly d(I–C), an Unusual Double-Helical DNA. *Nature*. **1970**, *228* (5277), 1166–1169..

(32) Nakamoto, K.; Tsuboi, M.; Strahan, G. D. *Drug-DNA Interactions: Structures and Spectra*; John Wiley & Sons, 2008.

(33) Ussery, D.W. (2002) “DNA Structure: A-, B- and Z-DNA Helix Families” Encyclopedia of Life Sciences : 1-7.

(34) Ussery, D. DNA Structure: A-, B- and Z-DNA Helix Families; 2002.

(35) Kimsey, I.; Al-Hashimi, H. M. Increasing Occurrences and Functional Roles for High Energy Purine-Pyrimidine Base-Pairs in Nucleic Acids. *Current Opinion in Structural Biology*. **2014**, *24*, 72–80.

(36) Pohl, F. M.; Jovin, T. M. Salt-Induced Co-Operative Conformational Change of a Synthetic DNA: Equilibrium and Kinetic Studies with Poly(DG-DC). *Journal of Molecular Biology* **1972**, *67* (3), 375–396. (72)90457-3.

(37) Wang, A. H.; Quigley, G. J.; Kolpak, F. J.; Crawford, J. L.; van Boom, J. H.; van der Marel, G.; Rich, A. Molecular Structure of a Left-Handed Double Helical DNA Fragment at Atomic Resolution. *Nature*. **1979**, *282* (5740), 680–686.

(38) Ha, S. C.; Lowenhaupt, K.; Rich, A.; Kim, Y.-G.; Kim, K. K. Crystal Structure of a Junction between B-DNA and Z-DNA Reveals Two Extruded Bases. *Nature*. **2005**, *437* (7062), 1183–1186.

(39) Rich, A.; Zhang, S. Z-DNA: The Long Road to Biological Function. *Nature Reviews Genetics*. **2003**, *4* (7), 566–572.

(40) Kastenholz, M. A.; Schwartz, T. U.; Hünenberger, P. H. The Transition between the B and Z Conformations of DNA Investigated by Targeted Molecular Dynamics Simulations with Explicit Solvation. *Biophysical Journal*. **2006**, *91* (8), 2976–2990.

(41) Behe, M.; Felsenfeld, G. Effects of Methylation on a Synthetic Polynucleotide: The B--Z Transition in Poly(DG-M5dC).Poly(DG-M5dC). *Proceedings of the National Academy of Sciences*. **1981**, *78* (3), 1619–1623.

(42) Peck, L. J.; Nordheim, A.; Rich, A.; Wang, J. C. Flipping of Cloned d(PCpG)n.d(PCpG)n DNA Sequences from Right- to Left-Handed Helical Structure by

Salt, Co(III), or Negative Supercoiling. *Proceedings of the National Academy of Sciences*. **1982**, *79* (15), 4560–4564.

(43) L, N. D.; Lehninger, A. L.; Nelson, D. L.; Cox, M. M.; Cox, M. M.; Nelson, I. for M. G. D. L.; Cox, U. M. M. *Lehninger Principles of Biochemistry*; W. H. Freeman, 2005.

(44) Herbert, A.; Rich, A. The Biology of Left-Handed Z-DNA (∗). *Journal of Biological Chemistry*. **1996**, *271* (20), 11595–11598.

(45) Liu, L. F.; Wang, J. C. Supercoiling of the DNA Template during Transcription. *Proceedings of the National Academy of Sciences*. **1987**, *84* (20), 7024–7027.

(46) Herbert, A.; Rich, A. Left-Handed Z-DNA: Structure and Function. In *Structural Biology and Functional Genomics*; Bradbury, E. M., Pongor, S., Eds.; NATO Science Series; Springer Netherlands: Dordrecht, 1999; pp 53–72.

(47) Lafer, E. M.; Möller, A.; Nordheim, A.; Stollar, B. D.; Rich, A. Antibodies Specific for Left-Handed Z-DNA. *Proceedings of the National Academy of Sciences*. **1981**, *78* (6), 3546–3550.

(48) Möller, A.; Gabriels, J. E.; Lafer, E. M.; Nordheim, A.; Rich, A.; Stollar, B. D. Monoclonal Antibodies Recognize Different Parts of Z-DNA. *Journal of Biological Chemistry*. **1982**, *257* (20), 12081–12085.

(49) Lafer, E. M.; Valle, R. P.; Möller, A.; Nordheim, A.; Schur, P. H.; Rich, A.; Stollar, B. D. Z-DNA-Specific Antibodies in Human Systemic Lupus Erythematosus. *Journal of Clinical Investigation*. **1983**, *71* (2), 314–321.

(50) Suram, A.; Rao, K. S. J.; Latha, K. S.; Viswamitra, M. A. First Evidence to Show the Topological Change of DNA from B-DNA to Z-DNA Conformation in the Hippocampus of Alzheimer's Brain. *Neuromolecular Medicine*. **2002**, *2* (3), 289–297.

(51) Herbert, A.; Lowenhaupt, K.; Spitzner, J.; Rich, A. Chicken Double-Stranded RNA Adenosine Deaminase Has Apparent Specificity for Z-DNA. *Proceedings of the National Academy of Sciences*. **1995**, *92* (16), 7550–7554.

(52) Chiang, D. C.; Li, Y.; Ng, S. K. The Role of the Z-DNA Binding Domain in Innate Immunity and Stress Granules. *Frontiers in Immunology*. **2021**, *11*, 3779.

(53) Dick, A. L. W.; Khermesh, K.; Paul, E.; Stamp, F.; Levanon, E. Y.; Chen, A. Adenosine-to-Inosine RNA Editing Within Corticolimbic Brain Regions Is Regulated in Response to Chronic Social Defeat Stress in Mice. *Frontiers in Psychiatry*. **2019**, *10*, 277.

(54) Ng, S. K.; Weissbach, R.; Ronson, G. E.; Scadden, A. D. J. Proteins That Contain a Functional Z-DNA-Binding Domain Localize to Cytoplasmic Stress Granules. *Nucleic Acids Research*. **2013**, *41* (21), 9786–9799.

(55) Lee, C.-H.; Shih, Y.-P.; Ho, M.-R.; Wang, A. H.-J. The C-Terminal D/E-Rich Domain of MBD3 Is a Putative Z-DNA Mimic That Competes for Zα DNA-Binding Activity. *Nucleic Acids Research*. **2018**, *46* (22), 11806–11821.

(56) Hannoush, R. N.; Damha, M. J. Remarkable Stability of Hairpins Containing 2‘,5‘-Linked RNA Loops. *Journal of the American Chemical Society*. **2001**, *123* (49), 12368–12374.

(57) Kuznetsov, S. V.; Ren, C.-C.; Woodson, S. A.; Ansari, A. Loop Dependence of the Stability and Dynamics of Nucleic Acid Hairpins. *Nucleic Acids Research*. **2008**, *36* (4), 1098–1112.

(58) Scheffler, I. E.; Elson, E. L.; Baldwin, R. L. Helix Formation by DAT Oligomers. I. Hairpin and Straight-Chain Helices. *Journal of Molecular Biology*. **1968**, *36* (3), 291–304.

(59) Lightfoot, D. Thermodynamics of a Stable Yeast 5.8S RRNA Hairpin Helix. *Nucleic Acids Research*. **1978**, *5* (10), 3565–3577.

(60) Lake, J. A. Yeast Transfer RNA: A Small-Angle x-Ray Study. *Science*. **1967**, *156* (3780), 1371–1373.

(61) Cech, T. R.; Hearst, J. E. An Electron Microscopic Study of Mouse Foldback DNA. Cel.l **1975**, *5* (4), 429–446.

(62) Klämbt, D.; Richter, O. Computer Programs for Studying Conformations in Ribonucleic Acids. *Journal of Theoretical Biology*. **1976**, *58* (2), 319–324.

(63) Krebs, J. E.; Lewin, B.; Goldstein, E. S.; Kilpatrick, S. T. *Lewin's Essential Genes*; Jones & Bartlett Publishers, 2013.

(64) Banerjee, S.; Chalissery, J.; Bandey, I.; Sen, R. Rho-Dependent Transcription Termination: More Questions than Answers. *Journal of Microbiology*. **2006**, *44* (1), 11–22.

(65) Turnbough, C. L. Regulation of Bacterial Gene Expression by Transcription Attenuation. *Microbiology Molecular Biology Reviews*. **2019**, *83* (3), e00019-19.

(66) Clark, D. P.; Pazdernik, N. J. *Molecular Biology*; Elsevier, 2012.

(67) Sharp, S. J.; Schaack, J.; Cooley, L.; Burke, D. J.; Soil, D. Structure and Transcription of Eukaryotic TRNA Gene. *Critical Reviews in Biochemistry*. **1985**, *19* (2), 107–144.

(68) Sioud, M. *RNA Therapeutics: Function, Design, and Delivery*; Humana Press, 2010.

(69) Pelley, J. W. *Elsevier's Integrated Review Biochemistry E-Book: With STUDENT CONSULT Online Access*; Elsevier Health Sciences, 2011.

(70) Herskovits, T. T. Nonaqueous Solutions of DNA; Denaturation by Urea and Its Methyl Derivatives*. *Biochemistry*. **1963**, *2* (2), 335–340.

(71) Wang, X.; Lim, H. J.; Son, A. Characterization of Denaturation and Renaturation of DNA for DNA Hybridization. *Environmental Health Toxicology* **2014**, *29*.

(72) Huang, P. C. Effect of Guanidinium Ion on DNA Denaturation and Renaturation. *Biochemical and Biophysical Research Communications*. **1968**, *33* (3), 384–390.

(73) Crothers, D. M. The Kinetics of DNA Denaturation. *Journal of Molecular Biology*. **1964**, *9* (3), 712–733.

(74) Davidson, V. L.; Sittman, D. B. *Biochemistry*; Lippincott Williams & Wilkins, 1999.

(75) Timmis, J. N.; Ingle, J. The Nature of the Variable DNA Associated with Environmental Induction in Flax. *Heredity*. **1974**, *33* (3), 339–346.

(76) R. L. Letsinger, S. K. Chaturvedi, F. Farooqui, AndM. Salunkhe. "Use of Hydrophobic Substituents in Controlling Self-Assembly of Oligonucleotides" J. Am. Chem. Soc. (1993), 115, 7535-7536

(77) Freifelder, D.; Davison, P. F. Hyperchromicity and Strand Separation in Bacterial DNA. *Biophysical Journal*. **1962**, *2* (3), 249–256.

(78) Shih, T. Y.; Bonner, J. Thermal Denaturation and Template Properties of DNA Complexes with Purified Histone Fractions. *Journal of Molecular Biology* **1970**, *48* (3), 469–487.

(79) Mouzakis, K. D.; Lang, A. L.; Vander Meulen, K. A.; Easterday, P. D.; Butcher, S. E. HIV-1 Frameshift Efficiency Is Primarily Determined by the Stability of Base Pairs Positioned at the MRNA Entrance Channel of the Ribosome. *Nucleic Acids Research*. **2013**, *41* (3), 1901–1913.

(80) Gabriela, C.-C., Eugenia; Antonio, R.-A., José; Cecilia, A.-S., Karina; Manuel, C.-B., José. *Design of Experiments for Chemical, Pharmaceutical, Food, and Industrial Applications*; IGI Global, 2019.

(81) Dumitras, D. C. *Nd YAG Laser*; BoD – Books on Demand, 2012.

(82) Solomons, T. W. G.; Fryhle, C. B.; Snyder, S. A. *Organic Chemistry*; Wiley, 2013.

(83) Tang, Y.; Zeng, X.; Liang, J. Surface Plasmon Resonance: An Introduction to a Surface Spectroscopy Technique. *Journalof Chemical Education*. **2010**, *87* (7), 742–746.

(84) Long, Y.-T.; Jing, C. *Localized Surface Plasmon Resonance Based Nanobiosensors*; Springer Science & Business Media, 2014.

(85) *Annalen der Physik und Chemie*; J.A. Barth, 1852.

(86) Lambert, J. H. *I. H. Lambert ... Photometria sive de mensura et gradibus luminis, colorum et umbrae*; Augustae Vindelicorum : sumptibus viduae Eberhardi Klett typis Chistophori Petri Detleffsen, 1760.

(87) Maeder, M.; Neuhold, Y.-M. *Practical Data Analysis in Chemistry*; Elsevier, 2007.

(88) Woody, R. W. [4] Circular Dichroism. In *Methods in Enzymology*; Biochemical Spectroscopy; Academic Press, 1995; Vol. 246, pp 34–71.

(89) Kuroda, R.; Harada, T.; Shindo, Y. A Solid-State Dedicated Circular Dichroism Spectrophotometer: Development and Application. *Review of Scientific Instruments*. **2001**, *72* (10), 3802–3810.

(90) Uratani, Y.; Asakura, S.; Imahori, K. A Circular Dichroism Study of Salmonella Flagellin: Evidence for Conformational Change on Polymerization. *Journal of Molecular Biology*. **1972**, *67* (1), 85–98.

(91) Avitabile, C.; D'Andrea, L. D.; Romanelli, A. Circular Dichroism Studies on the Interactions of Antimicrobial Peptides with Bacterial Cells. *Scientific Reports*. **2014**, *4* (1), 4293.

(92) Suzuki, M.; Kawamura, N.; Miyagawa, H.; Garitaonandia, J. S.; Yamamoto, Y.; Hori, H. Measurement of a Pauli and Orbital Paramagnetic State in Bulk Gold Using X-Ray Magnetic Circular Dichroism Spectroscopy. *Physical Review Letters*. **2012**, *108* (4), 047201.

(93) Tomasz, M.; Barton, J. K.; Magliozzo, C. C.; Tucker, D.; Lafer, E. M.; Stollar, B. D. Lack of Z-DNA Conformation in Mitomycin-Modified Polynucleotides Having Inverted Circular Dichroism. *Proceedings of the National Academy of Sciences of the United States of America*. **1983**, *80* (10), 2874–2878.

(94) Knight, R. D.; Jones, B.; Field, S. *College Physics: A Strategic Approach Technology Update, Books a La Carte Edition*; Pearson Education Canada, 2012.

(95) Benenson, W.; Harris, J. W.; Stöcker, H.; Lutz, H. *Handbook of Physics*; Springer Science & Business Media, 2006.

(96) Miles, A. J.; Wallace, B. A. Chapter 6 - Biopharmaceutical Applications of Protein Characterisation by Circular Dichroism Spectroscopy. In *Biophysical Characterization of Proteins in Developing Biopharmaceuticals (Second Edition)*; Houde, D. J., Berkowitz, S. A., Eds.; Elsevier, 2020; pp 123–152.

(97) Dods, R. *Concepts in Bioscience Engineering*; Springer Nature, 2020.

(98) Greenfield, N. J. Using Circular Dichroism Spectra to Estimate Protein Secondary Structure. *Nauret Protocols*. **2006**, *1* (6), 2876–2890.

(99) Uversky, V. N.; Permi̇akov, E. A. *Methods in Protein Structure and Stability Analysis: Luminescence Spectroscopy and Circular Dichroism*; Nova Publishers, 2007.

(100) Hamamatsu Photonics.2007. Photomultiplier Tubes Basics and Applications. 3rd Ed. Hamamatsu Photonics K.K. Electron Tube .

(101) Rodger, A, Nordén, B. *Circular Dichroism and Linear Dichroism*; Oxford University Press, 1997.

(102) Pelletier, M. J.; Pelletier, C. C. RAMAN SPECTROSCOPY | Instrumentation. In *Encyclopedia of Analytical Science (Second Edition)*; Worsfold, P., Townshend, A., Poole, C., Eds.; Elsevier: Oxford, 2005; pp 94–104.

(103) Rodger, A.; Marshall, D. Beginners Guide to Circular Dichroism. *The Biochemist*. **2021**, *43* (2), 58–64.

(104) Crews, P.; Rodríguez, J.; Jaspars, M. *Organic Structure Analysis*; Oxford University Press, 2010.

(105) Akitt, J. W.; Mann, B. E. *NMR and Chemistry: An Introduction to Modern NMR Spectroscopy, Fourth Edition*; CRC Press, 2000.

(106) Yan, L.; Hu, Y.; Zhang, X.; Yue, B. Chapter Three - Applications of NMR Techniques in the Development and Operation of Proton Exchange Membrane Fuel Cells. In *Annual Reports on NMR Spectroscopy*; Webb, G. A., Ed.; Academic Press, 2016; Vol. 88, pp 149–213.

(107) Rule, G. S.; Hitchens, T. K. *Fundamentals of Protein NMR Spectroscopy*; Springer Science & Business Media, 2005.

(108) Mirau, P. *Solid-State Nmr of Polymers*; iSmithers Rapra Publishing, 2001.

(109) Cavanagh, J.; Fairbrother, W. J.; III, A. G. P.; Skelton, N. J.; Rance, M. *Protein NMR Spectroscopy: Principles and Practice*; Elsevier, 2010.

(110) Bruch, M. *NMR Spectroscopy Techniques, Second Edition,*; CRC Press, 1996.

(111) Edison, A. S.; Schroeder, F. C. 9.06 - NMR – Small Molecules and Analysis of Complex Mixtures. In *Comprehensive Natural Products II*; Liu, H.-W. (Ben), Mander, L., Eds.; Elsevier: Oxford, 2010; pp 169–196.

(112) Aue, W. P.; Bartholdi, E.; Ernst, R. R. Two-dimensional Spectroscopy. Application to Nuclear Magnetic Resonance. *Journal of Chemical Physics*. **1976**, *64* (5), 2229–2246.

(113) Rahman, A.-. *One and Two Dimensional NMR Spectroscopy*; Elsevier, 2013.

(114) Rule, G. S.; Hitchens, T. K. *Fundamentals of Protein NMR Spectroscopy*; Springer Science & Business Media, 2006.

(115) Lambert, J. B.; Mazzola, E. P.; Ridge, C. D. *Nuclear Magnetic Resonance Spectroscopy: An Introduction to Principles, Applications, and Experimental Methods*; John Wiley & Sons, 2018.

(116) Rahman, A.; Choudhary, M. I.; Wahab, A.-. *Solving Problems with NMR Spectroscopy*; Academic Press, 2015.

(117) Claridge, T. *High-Resolution NMR Techniques in Organic Chemistry*; Elsevier, 1999.

(118) Lindon, J.C.. (2016). Multidimensional NMR Spectroscopy. Reference Module in Chemistry, Molecular Sciences and Chemical .

(119) Finley, J. W.; Schmidt, S. J.; Serianni, A. S. *NMR Applications in Biopolymers*; Springer Science & Business Media, 2012.

(120) Gibbons, A. Stabilization of Z-DNA Through Chemical Modification Of Guanosine.BS.Thesis, Brock University, April 2017.

(121) Mazo, R. M. *Brownian Motion: Fluctuations, Dynamics, and Applications*; Clarendon Press, 2002.

(122) Pregosin, P. S. *NMR in Organometallic Chemistry*; John Wiley & Sons, 2013.

(123) Schalley, C. A. *Analytical Methods in Supramolecular Chemistry*; John Wiley & Sons, 2012.

(124) Rahman, A.; Choudhary, M. I. *Applications of NMR Spectroscopy: Volume 3*; Elsevier, 2015.

(125) *Encyclopedia of Spectroscopy and Spectrometry*; Academic Press, 2016.

(126) Scott, R. A.; Lukehart, C. M. *Applications of Physical Methods to Inorganic and Bioinorganic Chemistry*; John Wiley & Sons, 2013.

(127) Harwood, J. S.; Mo, H. *Practical NMR Spectroscopy Laboratory Guide: Using Bruker Spectrometers*; Elsevier Science, 2015.

(128) Harris, D. C. *Quantitative Chemical Analysis*; W. H. Freeman, 2010.

(129) U.S. Patent 3,263,484.

(130) Watson, E.S., O'Neil, M.J., Justin, J., Brenner, N. (1944) "A Differential Scanning Calorimeter for Quantitative Differe.

(131) Privalov, P. L., Monaselidze, (1975) D. R. Mol. Biol. 6, 7-33.

(132) Cimpoeşu, I., Stanciu, S., Enache, A., Răţoi, M., and Cimpoeşu, R. (2012)"Differential Scanning Calorimetry of Different.

(133) Penn, L.; Larsen, F. Physicochemical Properties of Kevlar 49 Fiber. *Journal of Applied Polymer Science*. **1979**, *23* (1), 59–73.

(134) Duguid, J. G.; Bloomfield, V. A.; Benevides, J. M.; Thomas, G. J. DNA Melting Investigated by Differential Scanning Calorimetry and Raman Spectroscopy. *Biophysical Journal*. **1996**, *71* (6), 3350–3360.

(135) Zhang, H.; Takenaka, M.; Isobe, S. DSC and Electrophoretic Studies on Soymilk Protein Denaturation. *Journal of Thermal Analysis and Calorimetry*. **2004**, *75* (3), 719–726.

(136) Hamrick, P. E. Thermal Denaturation of DNA Exposed to 2450 MHz CW Microwave Radiation. *Radiation Research* **1973**, *56* (2), 400–404.

(137) Hung, M.-S.; Kurosawa, O.; Washizu, M. Single DNA Molecule Denaturation Using Laser-Induced Heating. *Molecular and Cellular Probes* **2012**, *26* (3), 107–112.

(138) Müller, A. J.; Michell, R. M. Differential Scanning Calorimetry of Polymers. In *Polymer Morphology*; John Wiley & Sons, Ltd, 2016; pp 72–99.

(139) Demarest, S. J.; Frasca, V. Chapter 11 - Differential Scanning Calorimetry in the Biopharmaceutical Sciences. In *Biophysical Characterization of Proteins in Developing Biopharmaceuticals (Second Edition)*; Houde, D. J., Berkowitz, S. A., Eds.; Elsevier, 2020; pp 311–332.

(140) L. C. Thomas, "Practical Benefits of Using Heat Capacity Versus Heat FlowSignals", (2001) Proceedings of the 29th Conference.

(141) Riga, A. T.; Judovits, L. *Materials Characterization by Dynamic and Modulated Thermal Analytical Techniques*; ASTM International, 2001.

(142) Gill, P.; Moghadam, T. T.; Ranjbar, B. Differential Scanning Calorimetry Techniques: Applications in Biology and Nanoscience. *Journal of Biomolecular Techiques*. **2010**, *21* (4), 167–193.

(143) Brittain, H. G.; Bruce, R. D. Chapter 4 Thermal Analysis. In *Comprehensive Analytical Chemistry*; Ahuja, S., Jespersen, N., Eds.; Modern Instrumental Analysis; Elsevier, 2006; Vol. 47, pp 63–109.

(144) Schön, A.; Clarkson, B. R.; Jaime, M.; Freire, E. Temperature Stability of Proteins: Analysis of Irreversible Denaturation Using Isothermal Calorimetry. *Proteins*. **2017**, *85* (11), 2009–2016.

(145) Gromiha, M. M. *Protein Bioinformatics: From Sequence to Function*; Academic Press, 2011.

(146) Chang, R. *Chemistry*; McGraw-Hill, 2010.

(147) *Hyperthermophilic Enzymes, Part C*; Elsevier, 2001.

(148) Cranwell, P. B.; Page, E. M. *Foundations of Chemistry: An Introductory Course for Science Students*; John Wiley & Sons, 2021.

(149) Muñoz, V. *Protein Folding, Misfolding and Aggregation: Classical Themes and Novel Approaches*; Royal Society of Chemistry, 2008.

(150) Whitelegge, J. *Protein Mass Spectrometry*; Elsevier, 2008.

(151) Jones, C.; Mulloy, B.; Thomas, A. H. *Microscopy, Optical Spectroscopy, and Macroscopic Techniques*; Springer Science & Business Media, 1994.

(152) Grasby, J.; Stephen, N. *Nucleic Acids in Chemistry and Biology*; Blackburn, G. M., Gait, M. J., Loakes, D., Williams, D. M., Eds.; Royal Society of Chemistry, 2015.

(153) *Advances in Protein Chemistry*; Academic Press, 1992.

(154) González, M.; Bagatolli, L. A.; Echabe, I.; Arrondo, J. L. R.; Argaraña, C. E.; Cantor, C. R.; Fidelio, G. D. Interaction of Biotin with Streptavidin: THERMOSTABILITY AND

CONFORMATIONAL CHANGES UPON BINDING *. *Journal of Biological Chemistry*. **1997**, *272* (17), 11288–11294.

(155) Tello-Solís, S. R.; Romero-García, B. Thermal Denaturation of Porcine Pepsin: A Study by Circular Dichroism. *International Journal of Biological Macromolecules*. **2001**, *28* (2), 129–133.

(156) Goldsby, K.; Chang, R. *Chemistry*; McGraw-Hill Education, 2012.

(157) Rogers, D. W. *Concise Physical Chemistry*; John Wiley & Sons, 2011.

(158) Sprague, B. L.; Müller, F.; Pego, R. L.; Bungay, P. M.; Stavreva, D. A.; McNally, J. G. Analysis of Binding at a Single Spatially Localized Cluster of Binding Sites by Fluorescence Recovery after Photobleaching. *Biophysical Journal*. **2006**, *91* (4), 1169–1191.

(159) Ramesh, V. *Biomolecular and Bioanalytical Techniques: Theory, Methodology and Applications*; John Wiley & Sons, 2019.

(160) Chen, G. C.; Yang, J. T. Two-Point Calibration of Circular Dichrometer with d-10-Camphorsulfonic Acid. *Analytical Letters*. **1977**, *10* (14), 1195–1207.

(161) Mason, W. R. *Magnetic Circular Dichroism Spectroscopy*; John Wiley & Sons, 2007.

(162) Shugar, D.; Fox, J. J. Spectrophotometric Studies of Nucleic Acid Derivatives and Related Compounds as a Function of PH. I. Pyrimidines. *Biochimca Et Biophysica Acta*. **1952**, *9* (2), 199–218.

(163) Chakraborty, K.; Mantha, S.; Bandyopadhyay, S. Molecular Dynamics Simulation of a Single-Stranded DNA with Heterogeneous Distribution of Nucleobases in Aqueous Medium. *Journal of Chemical Physics*. **2013**, *139* (7), 075103.

(164) Marky, L. A.; Blumenfeld, K. S.; Kozlowski, S.; Breslauer, K. J. Salt-Dependent Conformational Transitions in the Self-Complementary Deoxydodecanucleotide d(CGCAATTCGCG): Evidence for Hairpin Formation. *Biopolymers.***1983**, *22* (4), 1247–1257.

(165) Tan, Z.-J.; Chen, S.-J. Nucleic Acid Helix Stability: Effects of Salt Concentration, Cation Valence and Size, and Chain Length. *Biophysical Journal* **2006**, *90* (4), 1175–1190.

(166) Tan, Z.-J.; Chen, S.-J. Salt Dependence of Nucleic Acid Hairpin Stability. *Biophysical Journal*. **2008**, *95* (2), 738–752.

(167) Kibbe, W. A. OligoCalc: An Online Oligonucleotide Properties Calculator. *Nucleic Acids Research*. **2007**, *35* (Web Server issue), W43-46.

(168) Marmur, J.; Doty, P. Determination of the Base Composition of Deoxyribonucleic Acid from Its Thermal Denaturation Temperature. *Journal of Molecular Biology*. **1962**, *5*, 109–118.

(169) Owczarzy, R.; You, Y.; Moreira, B. G.; Manthey, J. A.; Huang, L.; Behlke, M. A.; Walder, J. A. Effects of Sodium Ions on DNA Duplex Oligomers: Improved Predictions of Melting Temperatures. *Biochemistry*. **2004**, *43* (12), 3537–3554.

(170) Haasnoot, C. A. G.; de Leeuw, F. A. A. M.; Altona, C. The Relationship between Proton-Proton NMR Coupling Constants and Substituent Electronegativities—I: An Empirical Generalization of the Karplus Equation. *Tetrahedron*. **1980**, *36* (19), 2783–2792.

(171) Sato, T. Structure of 2'-Deoxyadenosine, C10H13N5O3. *Acta Crystallographica Section C: Crystal Structure Communications*. **1984**, *40* (5), 880–882.

(172) Wu, Z. *Lecture Notes on Computational Structural Biology*; World Scientific, 2008.

(173) Goto, M.; Kanno, H.; Sugaya, E.; Osa, Y.; Takayanagi, H. Crystal Structure of Adenosinium Picrate. *Analytical Sciences: X-ray Structure Analysis Online*. **2004**, *20*, 39–40.

(174) Smith, G.; Wermuth, U. D.; Healy, P. C. Adenosinium 3,5-Di-nitro-salicyl-ate. *Acta Crystallographica Section E: Crystal Structure Reports Online*. **2004**, *60* (9), o1573–o1576.

(175) Caminiti, R.; Ortaggi, G.; Mazzei, R. A.; Ballirano, P.; Rizzi, R. Powder X-Ray Data for Adenosine C10H13N5O4. *Powder Diffraction*. **2000**, *15* (2), 112–115.

(176) X.P. Fu, H.A. Aisa, M. Abdurahim, A. Yili, S.F. Aripova, B. Tashkhodzhaev, *Chemistry of Natural Compounds* . 43, 181 (2007).

(177) Klooster, W. T.; Ruble, J. R.; Craven, B. M.; McMullan, R. K. Structure and Thermal Vibrations of Adenosine from Neutron Diffraction Data at 123 K. *Acta Crystallographica Section B: Structural Science*. **1991**, *47* (3), 376–383.

(178) Lai, T. F.; Marsh, R. E. The Crystal Structure of Adenosine. *Acta Crystallographica Section B: Structural Crystallography and Crystal Chemistry*. **1972**, *28* (7), 1982–1989.

(179) Levitt, M.; Warshel, A. Extreme Conformational Flexibility of the Furanose Ring in DNA and RNA. *Journal of the American Chemical Society*. **1978**, *100* (9), 2607–2613.

(180) Williams, D. A.; Foye, W. O.; Lemke, T. L. *Foye's Principles of Medicinal Chemistry*; Lippincott Williams & Wilkins, 2002.

(181) Yadav, M. *Computational Biochemistry*; Discovery Publishing House, 2009.

(182) Brooks, B. R.; Bruccoleri, R. E.; Olafson, B. D.; States, D. J.; Swaminathan, S.; Karplus, M. CHARMM: A Program for Macromolecular Energy, Minimization, and Dynamics Calculations. *Journal of Computational Chemistry*. **1983**, *4* (2), 187–217.

(183) Foloppe, N.; Hartmann, B.; Nilsson, L.; MacKerell, A. D. Intrinsic Conformational Energetics Associated with the Glycosyl Torsion in DNA: A Quantum Mechanical Study. *Biophysical Journal*. **2002**, *82* (3), 1554–1569.

(184) Suyama, T. L.; Gerwick, W. H.; McPhail, K. L. Survey of Marine Natural Product Structure Revisions: A Synergy of Spectroscopy and Chemical Synthesis. *Bioorganic & Medicinal Chemistry*. **2011**, *19* (22), 6675–6701.

(185) Patrick, G. *Instant Notes in Organic Chemistry*; Taylor & Francis, 2004.

(186) Ahuja, S.; Jespersen, N. *Modern Instrumental Analysis*; Elsevier, 2006.

(187) Claridge, T. D. W. *High-Resolution NMR Techniques in Organic Chemistry*; Elsevier, 2009.

(188) Burns, D. C.; Reynolds, W. F. *Optimizing NMR Methods for Structure Elucidation: Characterizing Natural Products and Other Organic Compounds*; Royal Society of Chemistry, 2018.

(189) Vranken, D. V.; Weiss, G. A. *Introduction to Bioorganic Chemistry and Chemical Biology*; Garland Science, 2018.

(190) Williams, A.; Martin, G.; Rovnyak, D. *Modern NMR Approaches to the Structure Elucidation of Natural Products: Volume 2: Data Acquisition and Applications to Compound Classes*; Royal Society of Chemistry, 2016.

(191) Rao, V. *Phytochemicals: A Global Perspective of Their Role in Nutrition and Health*; BoD – Books on Demand, 2012.

(192) Deene, Y. D. *NMR and MRI of Gels*; Royal Society of Chemistry, 2020.

(193) Kemple, M. D.; Rao, B. D. N. *NMR as a Structural Tool for Macromolecules: Current Status and Future Directions*; Springer Science & Business Media, 2012.

(194) Butts, C. P.; Jones, C. R.; Towers, E. C.; Flynn, J. L.; Appleby, L.; Barron, N. J. Interproton Distance Determinations by NOE – Surprising Accuracy and Precision in a Rigid Organic Molecule. *Beilstein Journal of Organic Chemistry*. **2010**, *9* (1), 177–184.

(195) Jones, C. R.; Butts, C. P.; Harvey, J. N. Accuracy in Determining Interproton Distances Using Nuclear Overhauser Effect Data from a Flexible Molecule. *Beilstein Journal of Organic Chemistry*. **2011**, *7*, 145–150.

(196) Lederberg, J.; Sutherland, G. L.; Buchanan, B. G.; Feigenbaum, E. A.; Robertson, A. V.; Duffield, A. M.; Djerassi, C. Applications of Artificial Intelligence for Chemical Inference. I. Number of Possible Organic Compounds. Acyclic Structures Containing Carbon, Hydrogen, Oxygen, and Nitrogen. *Journal of the American Chemical Society*. **1969**, *91* (11), 2973–2976.

(197) Elyashberg ME, Gribov LA: Formal Logic Method of Infrared Spectrum Interpretation. Zh Prikl Spectrosk. 1968, 8: 296-300.

(198) Sasaki, Shinichi.; Abe, Hidetsugu.; Ouki, Tatsumi.; Sakamoto, Masayoshi.; Ochiai, Shukichi. Automated Structure Elucidation of Several Kinds of Aliphatic and Alicyclic Compounds. *Analalytical Chemistry*. **1968**, *40* (14), 2220–2223.

(199) Nelson, D. B.; Munk, M. E.; Gash, K. B.; Herald, D. L. Alanylactinobicyclone. Application of Computer Techniques to Structure Elucidation. *Journal of Orgganic Chemistry*. **1969**, *34* (12), 3800–3805.

(200) Elyashberg, M.; Blinov, K.; Molodtsov, S.; Smurnyy, Y.; Williams, A. J.; Churanova, T. Computer-Assisted Methods for Molecular Structure Elucidation: Realizing a Spectroscopist's Dream. *Journal of Cheminformatics*. **2009**, *1* (1), 3.

(201) Sun, J.; Vanloon, J.; Yan, H. Influence of Microwave Irradiation on DNA Hybridization and Polymerase Reactions. *Tetrahedron Letters*. **2019**. 60 (39): 1-4.

(202) Sun, J.; Joshi, D.; Betancourt, F.; Solodinin, A.; Woodland, B.; Yan, H. Anion Exchange Chromatography of Oligonucleotides under Denaturing Conditions. *Nucleosides Nucleotides Nucleic Acids*. **2020**, *39* (6), 818–828.

(203) Summer, H.; Grämer, R.; Dröge, P. Denaturing Urea Polyacrylamide Gel Electrophoresis (Urea PAGE). *Journal of Visualized Experiments*. **2009**, No. 32, 1485.

(204) Zhang, W.; Liu, M.; Lee, C.; Salena, B. J.; Li, Y. Serendipitous Discovery of a Guanine-Rich DNA Molecule with a Highly Stable Structure in Urea. *Scientific Reports*. **2018**, *8* (1), 1935.

(205) Balcı, M. *Reaction Mechanisms in Organic Chemistry*; John Wiley & Sons, 2022.

(206) Shimokawa, K.; Ishihara, K.; Tezuka, Y. *Topology of Polymers*; Springer Nature, 2019.

(207) George S. Hammond, Wilfred G. Borduin, and Gerald A. Guter.

(208) Wang, X.; Son, A. Effects of Pretreatment on the Denaturation and Fragmentation of Genomic DNA for DNA Hybridization. *Environmental Science: Processes & Impacts*. **2013**, *15* (12), 2204–2212.

(209) Herskovits, T. T. Nonaqueous Solutions of DNA; Denaturation by Urea and Its Methyl Derivatives. *Biochemistry*. **1963**, *2*, 335–340.